A MECHANICALLY-GUIDED APPROACH TO THREE-DIMENSIONAL FUNCTIONAL MESOSTRUCTURES TOWARDS UNCONVENTIONAL APPLICATIONS

BY

KEWANG NAN

DISSERTATION

Submitted in partial fulfillment of the requirements
for the degree of Doctor of Philosophy in Mechanical Engineering
in the Graduate College of the
University of Illinois at Urbana-Champaign, 2018

Urbana, Illinois

Doctoral Committee:

Associate Professor Seok Kim, Chair
Professor John A. Rogers, Director of Research
Professor Paul V. Braun, Co-director of Research
Professor Xiuling Li

ABSTRACT

Controlled formation of three-dimensional functional mesostructures (3DFMs) has broad engineering implications in biomedical devices, microelectromechanical systems (MEMS), optics, and energy storage. Most existing 3D techniques, however, not only lack compatibility with essential electronic materials (silicon, metals, ceramics) that exist in solid-state or crystalline forms, but also produce in a slow and inefficient manner. This is in stark contrast to the planar technologies widely adopted by the modern semiconductor industry.

I propose to solve these challenges by a novel 3D assembly strategy based on the planar technologies, which involves precisely controlled 2D-to-3D transformations via the substrate-induced mechanical buckling. This lithography-based, mechanically-guided 3D approach is compatible with virtually any engineering thin films including semiconductors, metals, and polymers, applies to a wide range of length scales and geometries and produces in a high throughput.

In this dissertation, I present strategies that combine fabrications and mechanics to achieve a set of complex 3D geometries. I also study the potentials of the 3DFMs in micro-robotics. I further demonstrate the unique applications in energy harvesting, bio-integrated systems, and nanoscale sensing. The results may enlighten the development of advanced, multi-functional 3D electronic micro-systems inaccessible to other 3D techniques.

ACKNOWLEDGEMENTS

For starters, I would like to thank my advisor, Prof. John A. Rogers, who granted me the opportunity to study in this prestigious group and has continued to offer support, guidance, and motivation. I am extremely fortunate to have learned and benefited from his scientific insights, dedications to work and to his students, and great leadership.

I could not have succeeded without the consistent guidance and support from the senior mentors in the group. My special gratitude goes to Dr. Zheng Yan, currently an assistant professor at the University of Missouri, who not only guided me on research when I first started in the group but also cared for my personal life and offered tremendous help. Other senior members, such as Dr. Yuhao Liu, Dr. Lan Yin, and Dr. Xu Xie, warmly welcomed me to the group and helped me quickly adjust to the life as a doctoral student.

I would also like to thank the key collaborators, Prof. Yonggang Huang (on mechanics, Northwestern University, USA), Prof. Yihui Zhang (on mechanics, Tsinghua University, China), Prof. Xiuling Li (on electronics, University of Illinois at Urbana-Champaign, USA), and Prof. G. Jeffrey Snyder (on thermoelectrics, Northwestern University, USA), without whom the work cannot complete.

I have been able to conduct all experiments smoothly without worrying too much about technical issues, thanks to all the technical staff and the state-of-the-art lab equipment at the University of Illinois at Urbana-Champaign. These labs are the Materials Research Lab (MRL), the Micro and Nanotechnology Lab (MNTL), the Micro-Nano Mechanical Systems (MNMS) Cleanroom, and the Visualization Lab (ITG) at the Beckman Institute.

My parents have been the greatest supporters of my journey in the academia all this time. They paid a tremendous amount of money to support my undergraduate educations at one of the best institutions in the U.S. and were always by my side in the darkest moments. I am forever in their debts.

I feel extremely proud and fortunate to have grown up, learned from, and completed my doctoral studies alongside this many fabulous people.

TABLE OF CONTENTS

CHAPTER 1: MOTIVATION AND INTRODUCTION..1

1.1 Existing Techniques for 3D Mesostructures..1

1.2 Desire to Use Thin Films..3

1.3 Introduction to the Mechanically-Guided 3D Assembly..4

1.4 Dissertation Overview..7

1.5 Tables and Figures..9

1.6 References..18

CHAPTER 2: STRATEGIES TO COMPLEX 3D GEOMETRIES..21

2.1 Introduction..21

2.2 Kirigami/Origami-Inspired Membranes..22

2.2.1 Assembly Concepts and Design Principles..22

2.2.2 Diverse Geometries Enabled by Kirigami/Origami..25

2.3 Multi-Layered 3D Mesostructures..26

2.3.1 Assembly Concepts and Representative Results..26

2.3.2 NFC Devices with Enhanced Performances..27

2.4 Locally-Tunable 3D Mesostructures..28

2.4.1 Assembly Concepts and Design Principles..28

2.4.2 Functional Devices Enabled by Local Tuning..31

2.5 Conclusions..33

2.6 Methods..33

2.7 Figures..39

2.8 References 52
CHAPTER 3: TOWARDS MICRO-ROBOTICS 54
3.1 Introduction 54
3.2 Reversible Shape Transformations 54
3.2.1 Route to Morphable 3D Mesostructures and Electronics 56
3.2.2 Underlying Mechanics and General Design Approach 58
3.2.3 Representative Experimental Results 60
3.2.4 Morphable 3D RF Devices 60
3.3 Freestanding 3D Mesostructures 62
3.3.1 Interfacial Photopolymerizations 63
3.3.2 Plastic Mechanics 64
3.4 3D Micro Swimmers 65
3.5 Conclusions 66
3.6 Methods 66
3.7 Figures 74
3.8 References 84
CHAPTER 4: UNCONVENTIONAL APPLICATIONS 87
4.1 Introduction 87
4.2 3D Bio-integrated Electronic Scaffolds 87
4.2.1 High-resolution, in situ Imaging of Biological Tissues 88
4.2.2 Monitoring Electrophysiological Behaviors of Biological Tissues 89
4.2.3 Methods 90
4.3 Compliant and Stretchable Thermoelectric Coils for Energy Harvesting 94

4.3.1 Fabrication and Design Approaches 95
4.3.2 Thermal Design Principles: Heat Exchange and Impedance Matching.............97
4.3.3 Mechanical Compliance..100
4.3.4 Power Output and Projections 101
4.3.5 Methods...103
4.4 Soft 3D Vibratory Platforms for Nanomechanical Sensing.................................106
4.4.1 3D Multimodal Vibratory Systems Actuated by Lorentz-Force..........................106
4.4.2 Characterization of Modulus and Density Using Multimodal Resonances......108
4.4.3 Robustness and Reusability of 3D Vibrators..110
4.4.4 Integration with Thermal Actuators for Temperature-Dependent Measurements 111
4.4.5 Potential for Characterization of Anisotropic Elastic Moduli Using Multimodal Resonances...112
4.4.6 Methods..113
4.5 Conclusions...117
4.6 Figures..118
4.7 References...131
CHAPTER 5: CONCLUSIONS AND OUTLOOK 134
APPENDIX A: DESIGN AND MECHANICS OF MORPHABLE 3D MESOSTRUCTURES..136
A. 1 Scaling Law for the Strain Energy Barrier..136
A. 2 Design Process for 2D Precursors with Multiple Buckling Modes 137
A. 3 Appendix Figures..139

APPENDIX B: POWER OPTIMIZATION IN THERMOELECTRIC HARVESTERS 142

B. 1 Power Output from a Thermoelectric Harvester 142

B. 2 Thermal Impedance Matching Condition 143

B. 3 Thermal Impedance Matching in Coil Harvesters 143

APPENDIX C: 3D VIBRATORS FOR MECHANICAL CHARACTERIZATION OF NANO-THIN FILMS 144

C. 1 Scaling Law in Eq. (1), Section 4.4.2 144

C. 2 Effective Modulus and Average Density of an n-Layer Composite 145

C. 3 Polymer Patterns for Determining Polymer Modulus and Density of Isotropic Materials 145

C. 4 Determination of Polymer Modulus and Density from Multimodal Resonance 146

C. 5 Polymer Patterns for Determining Longitudinal Modulus and Transverse Modulus of Transversely Isotropic Materials 147

CHAPTER 1

MOTIVATION AND INTRODUCTION

There is a drive for electronic sensors and devices to become increasingly compact and conformal to the operating environment, especially for wearable and bio-integrated applications. Compared to the early-generation wearable electronics consisting of bulky hardware and substrates that integrate with human bodies only at the surface level (Figure 1.1a)[1-2], the state-of-the-art flexible electronics, with significantly reduced overall size and stiffness, can conform at the tissue level (Figure 1.1b) to realize more accurate sensing and direct stimulations, and less weight bearing of the tissues[3-6]. The next-generation sensing requires further reductions in device size and stiffness, and dramatic changes in device geometries from two-dimensional (2D) to three-dimensional (3D) for seamless integrations at the micro/cellular level (Figure 1.1c). However, it remains challenging to fabricate 3D functional mesostructures (3DFMs) in a reliable and high-throughput fashion, with full-scale sensing and electronic capabilities as their 2D counterparts.

The past decade has witnessed numerous approaches to 3DFMs, ranging from printing-based 3D techniques to those that involve physical deformations such as folding, rolling and assembling[7-17]. This chapter will begin with a brief review of the existing 3D approaches, which motivates the development of our lithography-based, mechanically-guided 3D assembly strategy. The rest of the chapter introduces our assembly strategy in terms of fabrications, mechanics, and applicability, and concludes with an overview of the dissertation.

1.1 Existing Techniques for 3D Mesostructures

Most existing techniques for 3DFMs fall into one of the four categories based on the dominating mechanisms for 3D formations, which are printing, folding, rolling, and assembling[17].

Printing-Based Techniques. Also known as 3D printing or additive manufacturing, the printing-based techniques represent one of the most recognized developments in the field, where highly complex and customized 3D geometries are directly printed/written using computer-controlled nozzles/lasers on a variety of substrates. Depending on whether nuzzles or lasers are used, they further divide into ink-based or light-based printing. The former can produce spanning and electrically conductive 3D features (Figure 1.2a)[18] using viscoelastic inks mixed with conductive metal nanoparticles, while the latter is particularly good at fabricating sub-micron features (Figure 1.2b)[19-20] with stunning resolutions. Nonetheless, printing-based techniques suffer from several major limitations, the most notable of which is their incompatibility with high-performance electronic materials (semiconductors, metals, and ceramics) that only exist in solid-state or crystalline forms. As a result, they cannot produce sensors and devices that offer on-par performances with conventional solid-state electronics. In addition, the printed 3D structures often have high stiffness and limited flexibility as they need to support their own weight during the bottom-up fabrications, making them unbefitting for wearable and bio-integrated applications. Furthermore, the serial nature of printing significantly limits its production efficiency and speed, as opposed to the conventional planar technologies, namely techniques based on photolithography, which can manufacture tens of thousands of devices in a parallel manner.

Folding, Rolling, and Assembling. Another class of 3D strategy draws inspirations from macroscopic deformations such as folding, rolling, and assembling. It typically starts with the fabrications of 2D precursors via the conventional planar technologies, followed by the physical transformations into 3D configurations by the microscopic actuations including surface tension[21], thin-film residual stress[11], and stimuli responses from composite materials[15] (Figure 1.2c).

Although these methods are compatible with certain solid-state materials, the accessible 3D geometries are highly dependent on and thus limited by the types of actuations. In addition, these actuations can be difficult to implement, some of which require harsh conditions (i.e. corrosive chemicals, elevated temperature), while some demand sophisticated external control (i.e. electrical and/or magnetic field). As a result, many of these strategies are confined to a specific set of materials and are impossible to scale up or down.

1.2 Desire to Use Thin films

As can be seen from the above discussion, most existing 3D techniques are unsuitable for producing flexible, customizable 3DFMs for wearable and bio-integrated applications. On the contrary, the state-of-the-art flexible electronics that adopt thin-film geometries, as shown in Figure 1.1b, can realize seamless integrations with even the softest biological tissues. I believe that the solution to 3D lies within 2D thin films, for reasons in both fabrications and mechanics.

Fabrications. The existing 3D techniques are summarized and compared with the conventional planar technologies (i.e. photolithography-based techniques) in Table 1.1. It is evident that the planar technologies outperform various 3D techniques in almost all aspects including material and geometric diversity, feature size, and manufacturing efficiency. They are also widely considered as the most studied and optimized manufacturing technique in modern industry[22]. It is therefore desirable to use the planar technologies as the core technique, and correspondingly the thin-film materials as the building blocks for 3DFMs.

Mechanics. The advantages of using thin films as the build blocks for 3DFMs can also be understood from a mechanics perspective. Virtually any material, if sufficiently thin, can become flexible as the flexural rigidity depends cubically on the thickness (Figure 1.3a)[27]:

$$Flexural\ rigidity = \frac{Et^3}{12(1 - v^2)}$$

where *E*, *t*, and *v* are elastic modulus, thickness and Poisson's ratio of the material, respectively. As an example, silicon exists as rigid wafers in its bulk forms (Figure 1.3b) but behaves like papers when the thickness is significantly reduced (Figure 1.3c). This concept has broad implications in thin-film devices for wearable and bio-integrated applications. Among them, the most prominent is perhaps the use of mono-crystalline silicon, one of the most important yet brittle semiconductors, to realize inorganic active electronic circuits that are flexible enough for conformal attachment onto the soft and corrugated tissue surfaces such as skin, heart, and brain, and provide various functions of sensing, stimulation, and diagnosis (Figure 1.1b)[3-6].

1.3 Introduction to the Mechanically-Guided 3D Assembly

These and other groundworks motivate us to propose a seminal method that assembles the thin-film materials with strategic 2D layouts into 3DFMs using the substrate-induced mechanical buckling[28]. This mechanically-guided 3D technique not only enables a wide range of highly customizable 3D geometries across different length scales, but also gains full access to the various advantages of the planar technologies, including the compatibility with state-of-the-art electronic materials (semiconductors, metals, and ceramics), the high resolution of patterning, and the ability to batch productions.

General Procedures. The general procedures of the mechanically-guided 3D assembly involve I) fabricating 2D precursors using the planar technologies and releasing them from the fabrication substrates (Figure 1.4a), II) transferring the 2D precursors to a previously stretched elastomer substrate and bonding at the selective locations called bonding sites (red, Figure 1.4b), and III) relaxing the elastomer substrate to provide sufficient compressive forces at the bonding sites to drive the 2D-to-3D transformations (Figure 1.4c). A quantitative example of such transformations is given in Figure 1.4b-c, where the 2D serpentine precursors transform into the 3D helical coils through relaxation of the elastomer substrate.

Fabrications of 2D Precursors. The 2D precursors made of mono-crystalline silicon are as an example to illustrate the fabrication process. It starts by defining 2D precursors in the device silicon layer of a silicon-on-insulator (SOI) wafer through photolithography (i.e. photoresist patterning and dry etching), followed by partial undercut in buffered oxide etchant to remove the exposed buried oxide layer. Another photolithography step defines a layer of positive photoresist that covers all the 2D precursors except the bonding sites. The photoresist also flows underneath the 2D precursors, forming an anchor to secure them during subsequent full undercut in concentrated hydrofluoric acid (HF), which completely release the precursors from the fabrication substrate. After rinsing the remaining HF and drying, a thin layer of silicon oxide is deposited on the 2D precursors by electron beam evaporation. The 2D precursors are then transfer printed[29] onto a flat slab of polydimethylsiloxane (PDMS), which are subsequently transferred onto a piece of soft, water-soluble tape to prepare for the 3D assembly. A flow diagram can be found in Figure 1.5.

Assembly into 3D. While still on the water-soluble tape, the samples and the pre-stretched elastomer substrate, made of silicone, are exposed to ultra-violet induced ozone, then laminated firmly and cured in the oven. The bonding sites deposited with silicon oxide will chemically react with silicone through a condensation reaction to form strong Si-O-Si linkage (Figure 1.6), whereas the non-bonding sites are protected by the photoresist to have only weak Van der Waals interactions with silicone. The bonding strength is ~ 8 J/m^2 for the bonding sites and only ~ 0.2 J/m^2 for the non-bonding sites, which ensures good selectivity. Finally, the water-soluble tape and the photoresist are dissolved by warm water and organic solvent, respectively, and the elastomer substrate is slowly relaxed to complete the 3D assembly.

Diversities in 3D Geometries, Materials, and Length Scales. A diverse set of complex 3D geometries are accessible through strategic designs of the 2D precursors and the layouts of the bonding sites. Figure 1.7 presents examples made of mono-crystalline silicon with ribbons and meshes as the primary geometric units[28]. Techniques and strategies discussed in Chapter 2 of this dissertation further extend the accessible geometries to kirigami/origami membranes, multi-layers, and locally-tunable structures.

The compatibility with the planar technologies also implies large degrees of freedom in the choices of starting materials and length scales (Figure 1.8)[30]. Planar technologies across the entire mesoscales, such as electron beam lithography (< 10 μm), photolithography (10 μm – 1 cm), and laser cutting (>1 cm) can all be used to fabricate the 2D precursors. Material-wise, the 3DFMs can be built from virtually any thin-film materials, including the grown semiconductors, the physically or electrochemically deposited metals, and the spin coated or drop casted polymers.

1.4 Dissertation Overview

The mechanically-guided 3D assembly provides a reliable route to tunable, flexible and stretchable 3DFMs that are otherwise inaccessible with existing 3D techniques, leading to exciting device opportunities in tunable electronics, micro robotics, energy harvesting, wearable electronics and biomedical applications. In this dissertation, I present the results of various strategies towards complex 3D geometries, study the potentials of the 3DFMs in micro-robotics, and demonstrate the unique applications in energy harvesting, bio-integrated systems, and nanoscale sensing.

Chapter 1 provides the **motivation and introduction** of the mechanically-guided 3D assembly, with an emphasis on the fabrications and the mechanics. The advantages of this 3D approach, including the diversities in materials and length scales, and the compatibility with batch productions are discussed.

Chapter 2 presents various strategies to achieve the **complex 3D geometries**, such as kirigami/origami membranes, multi-layers, and locally-tunable structures, with an emphasis on the importance of finite element analysis (FEA) as a quantitative design tool.

Chapter 3 presents studies on the potentials of the 3DFMs towards micro-robotics. Specifically, I investigate a set of 3DFMs capable of reversible shape transformations by manipulating the sequences of strain release in the elastomer substrate. The results lead to the development of tunable, shape-shifting 3D electronics. I also propose and demonstrate the strategy to build untethered, free-standing 3DFMs. The chapter concludes with a demonstration of 3D micro swimmers that have controllable swimming trajectories.

Chapter 4 provides three examples of the **unique applications** enabled by the mechanically-guided 3D assembly, which are the 3D electronic scaffolds for *in vitro* biological studies, the 3D thermoelectric energy harvesters for wearable applications, and the 3D vibratory

platforms for nanomechanical sensing. The results represent crucial components (energy supplies, structural supports, and sensors) towards miniature, multi-functional, bio-integrated 3D electronic platforms for the next-generation biomedical research.

Chapter 5 provides the **conclusions** of the key findings from previous chapters and the **outlook** on the possible future directions.

This dissertation completes the story of the mechanically-guided 3D assembly from invention, mechanics, fabrications, designs to applications.

1.5 Tables and Figures

Technique	Compatible Materials	Geometries	Finest Feature Size Reported	Number of Samples per Production
Ink-based 3D printing	Polymers, inorganic nanoparticles	Arbitrary 3D shapes	~ 500 nm [23]	In series, slow
Light-based 3D printing	Photosensitive polymers	Arbitrary 3D shapes	~55 nm [24]	In series, slow
Folding, rolling, and assembling	Shape-memory polymers/alloys, thin-film inorganics, hydrogels	Simple curved geometries (tubes, grippers)	~100 nm [25]	In parallel, fast
Planar technology	Almost all thin-film materials	Arbitrary 2D shapes	~6 nm [26]	In parallel, fast

Table 1.1 Summary of existing 3D techniques and comparison with the conventional planar technologies.

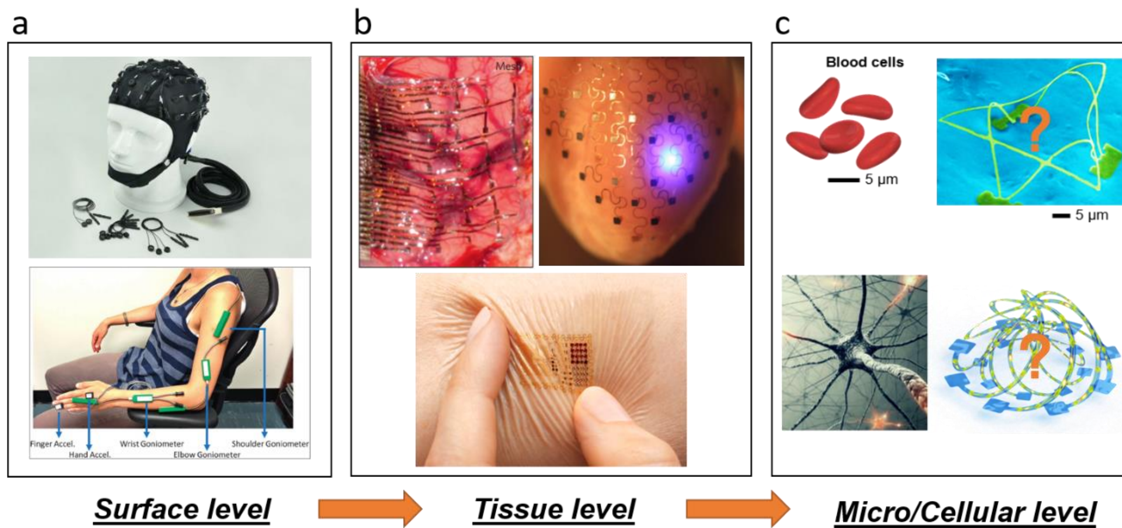

Figure 1.1 Evolution of electronic sensors and devices for wearable and bio-integrated applications. (a) Examples of the early-generation wearable electronics consisting of bulky hardware and substrates that integrate with human bodies only at the surface level. (b) Examples of the state-of-the-art flexible electronics that conform at the tissue level. (c) Schematics of the next-generation devices that are tiny and 3D for seamless integrations at the micro/cellular level. Reproduced from references 1-6.

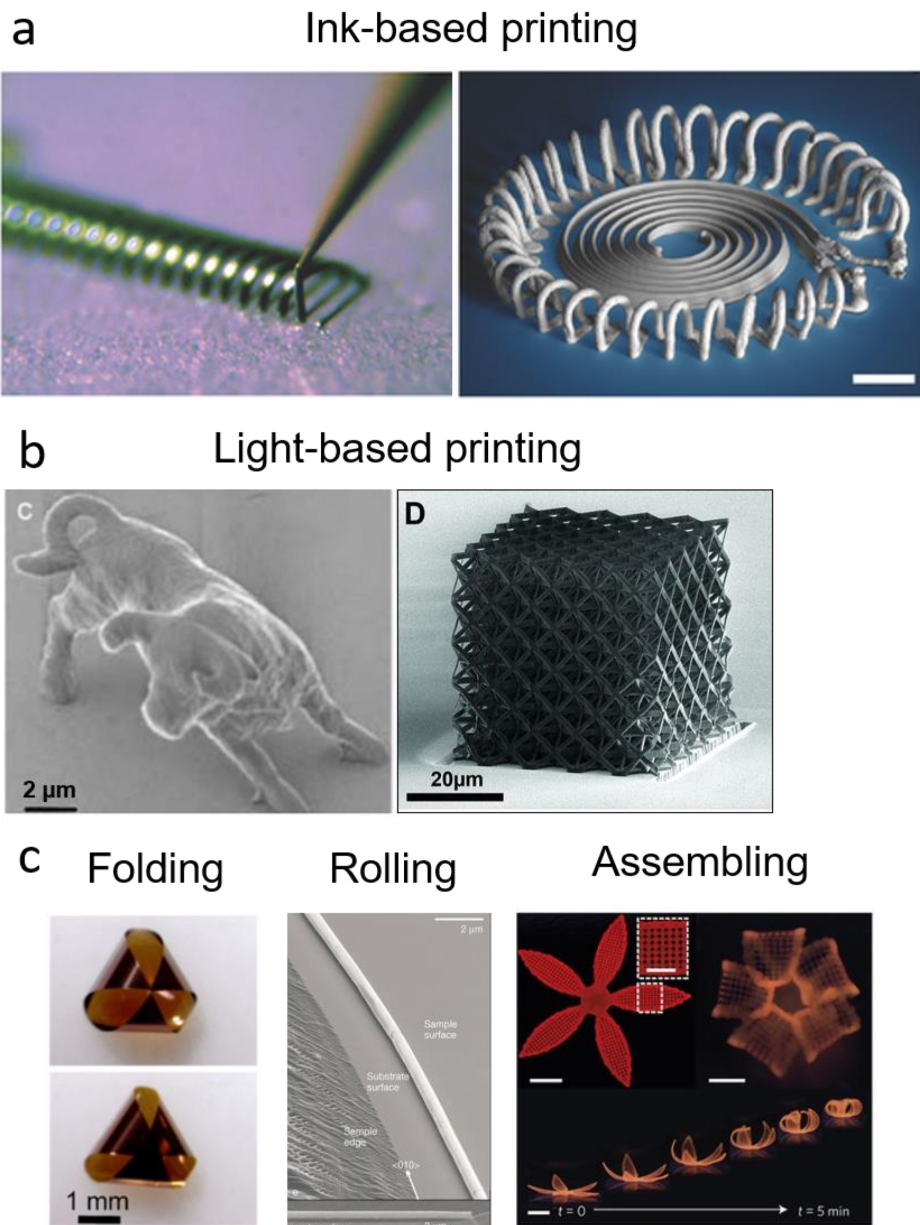

Figure 1.2 Examples of 3D mesostructures produced by existing techniques. (a) Spanning and electrically conductive features by ink-based printing. (b) Structures with highly-customized sub-micron features by light-based printing. (c) 3D inorganic structures produced by folding and rolling, and 3D composite structures capable of self-assembling into 3D. Reproduced from references 11, 15, 18-21.

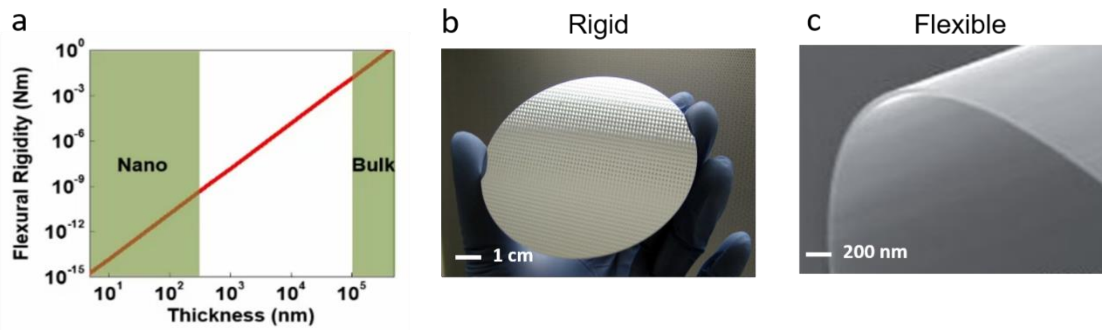

Figure 1.3 Flexibility due to reduced thickness. (a) Log-log plot of flexural rigidity of silicon as a function of its thickness. (b) Rigid silicon wafers in its bulk form. (c) Flexible silicon nanomembranes with significantly reduced thickness. Reproduced from references 27.

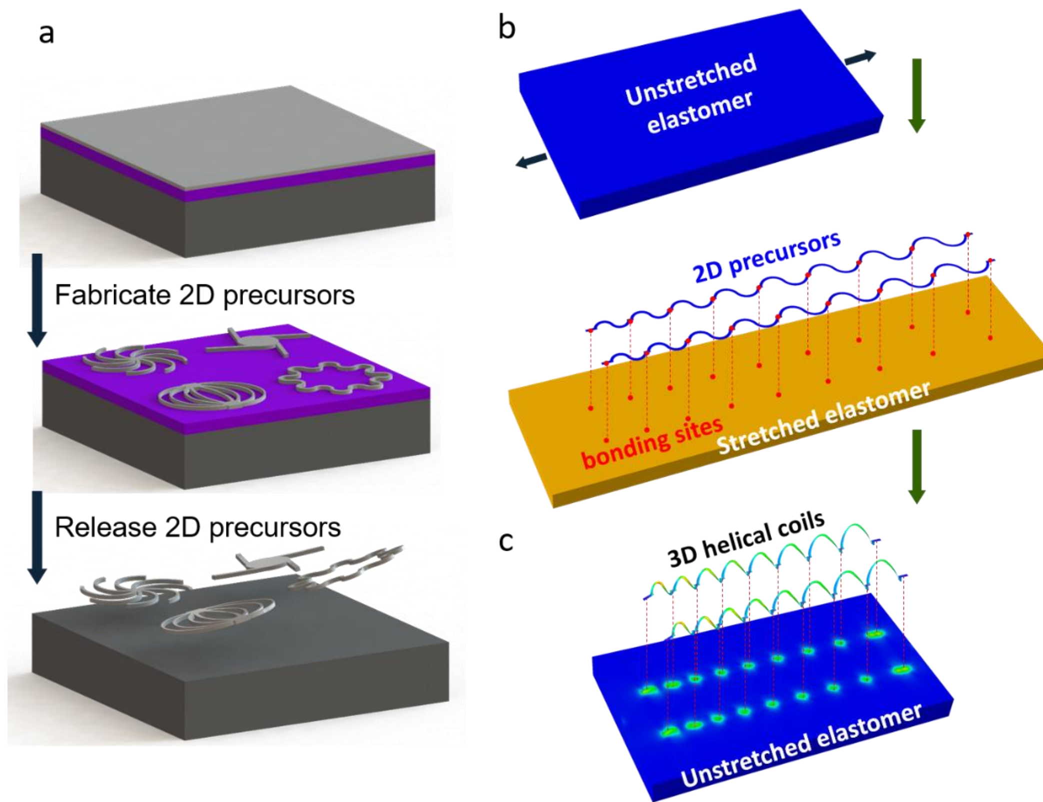

Figure 1.4 General procedures of the mechanically-guided 3D assembly. (a) Fabrications of the 2D precursors. (b) Transfer and attachment of the 2D precursors onto a previously stretched elastomer substrate. (c) Formations of 3D geometries by relaxation of the elastomer substrate. Reproduced from references 28.

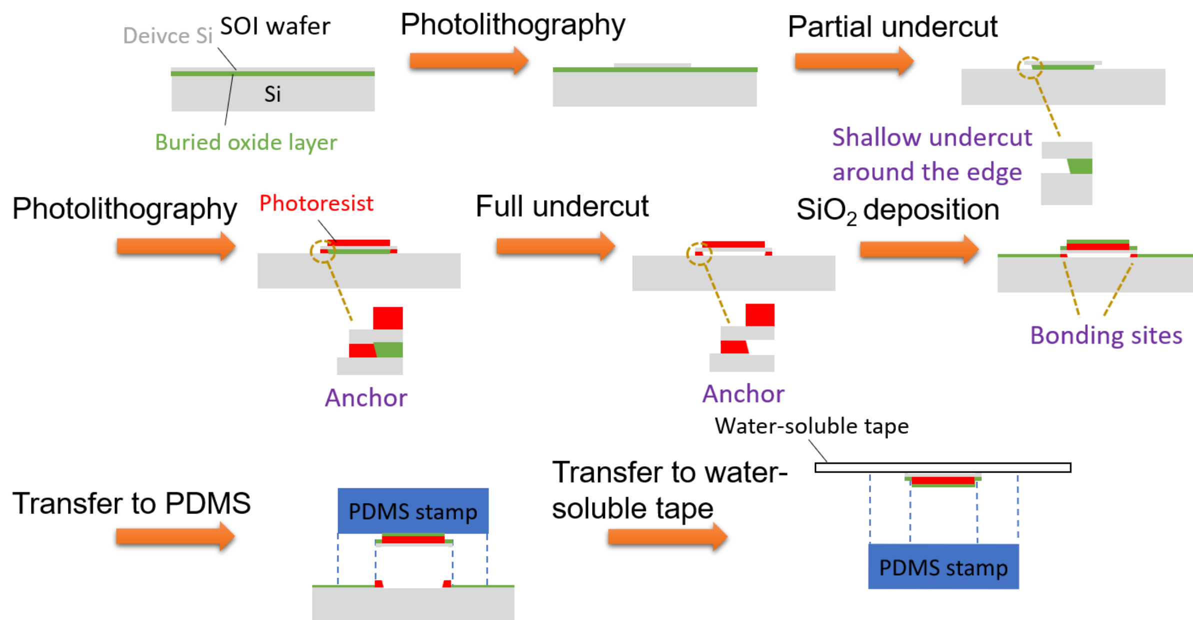

Figure 1.5 Flow diagram of the fabrications of 2D silicon precursors.

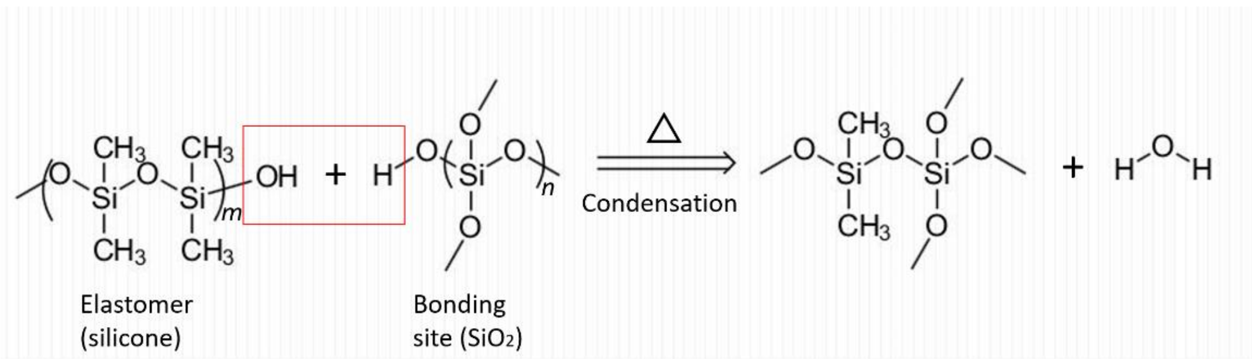

Figure 1.6 Chemical reaction between elastomer and SiO_2 that results in strong bonding sites.

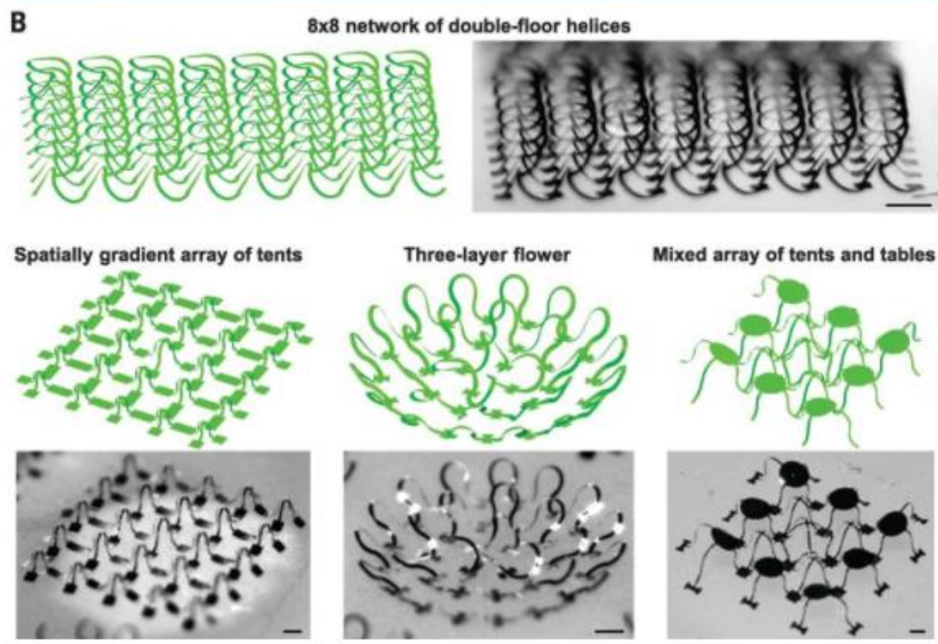

Figure 1.7 Examples of 3D silicon structures with ribbons and meshes as the primary geometric units. Reproduced from reference 28.

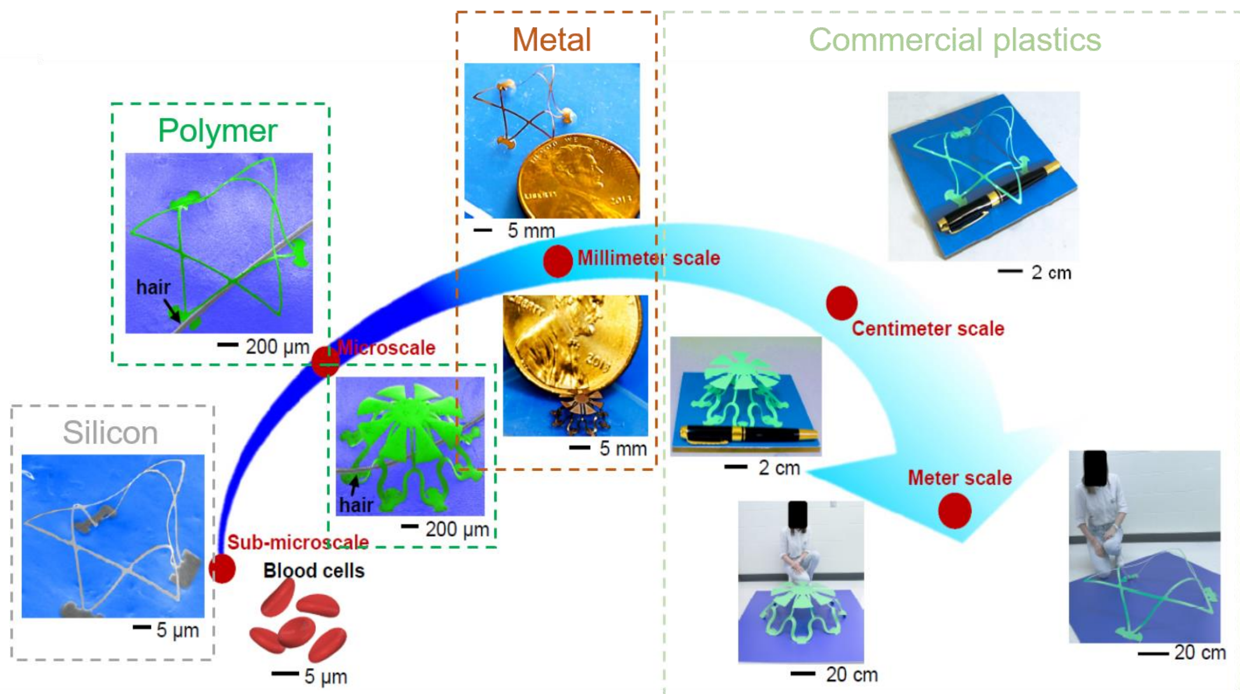

Figure 1.8 The diversity in materials and length scales of the mechanically-guided 3D assembly. Reproduced and modified from reference 30.

1.6 References

1. Rossini, Paolo M., et al. "Non-invasive electrical and magnetic stimulation of the brain, spinal cord and roots: basic principles and procedures for routine clinical application. Report of an IFCN committee." Electroencephalography and clinical neurophysiology 91.2 (1994): 79-92.

2. Rahimi, Fariborz, et al. "Effective management of upper limb parkinsonian tremor by incobotulinumtoxinA injections using sensor-based biomechanical patterns." Tremor and Other Hyperkinetic Movements 5 (2015).

3. Kim, Dae-Hyeong, et al. "Epidermal electronics." science 333.6044 (2011): 838-843.

4. Hammock, Mallory L., et al. "25th anniversary article: the evolution of electronic skin (e - skin): a brief history, design considerations, and recent progress." Advanced materials 25.42 (2013): 5997-6038.

5. Kim, Dae-Hyeong, et al. "Dissolvable films of silk fibroin for ultrathin conformal bio-integrated electronics." Nature materials 9.6 (2010): 511.

6. Xu, Lizhi, et al. "3D multifunctional integumentary membranes for spatiotemporal cardiac measurements and stimulation across the entire epicardium." Nature communications 5 (2014): ncomms4329.

7. Cumpston, Brian H., et al. "Two-photon polymerization initiators for three-dimensional optical data storage and microfabrication." Nature 398.6722 (1999): 51-54.

8. Zheng, Xiaoyu, et al. "Multiscale metallic metamaterials." Nature materials 15.10 (2016): 1100-1106.

9. Leong, Timothy G., et al. "Tetherless thermobiochemically actuated microgrippers." Proceedings of the National Academy of Sciences 106.3 (2009): 703-708.

10. Froeter, Paul, et al. "Toward intelligent synthetic neural circuits: directing and accelerating neuron cell growth by self-rolled-up silicon nitride microtube array." ACS nano 8.11 (2014): 11108-11117.

11. Schmidt, Oliver G., and Karl Eberl. "Nanotechnology: Thin solid films roll up into nanotubes." Nature 410.6825 (2001): 168-168.

12. Ahn, Bok Y., et al. "Omnidirectional printing of flexible, stretchable, and spanning silver microelectrodes." Science323.5921 (2009): 1590-1593.

13. Tumbleston, John R., et al. "Continuous liquid interface production of 3D objects." Science 347.6228 (2015): 1349-1352.

14. Sun, C., et al. "Projection micro-stereolithography using digital micro-mirror dynamic mask." Sensors and Actuators A: Physical 121.1 (2005): 113-120.

15. Gladman, A. Sydney, et al. "Biomimetic 4D printing." Nature materials 15.4 (2016): 413-418.

16. Kim, Jungwook, et al. "Designing responsive buckled surfaces by halftone gel lithography." Science 335.6073 (2012): 1201-1205.

17. Zhang, Yihui, et al. "Printing, folding and assembly methods for forming 3D mesostructures in advanced materials." Nature Reviews Materials 2.4 (2017): natrevmats201719.

18. Zhou, Nanjia, et al. "Gigahertz Electromagnetic Structures via Direct Ink Writing for Radio‐Frequency Oscillator and Transmitter Applications." Advanced Materials 29.15 (2017).

19. LaFratta, Christopher N., et al. "Multiphoton fabrication." Angewandte Chemie International Edition 46.33 (2007): 6238-6258.

20. Meza, Lucas R., Satyajit Das, and Julia R. Greer. "Strong, lightweight, and recoverable three-dimensional ceramic nanolattices." Science 345.6202 (2014): 1322-1326.

21. Guo, Xiaoying, et al. "Two-and three-dimensional folding of thin film single-crystalline silicon for photovoltaic power applications." Proceedings of the National Academy of Sciences 106.48 (2009): 20149-20154.

22. Thompson, Larry F. "An introduction to lithography." 1983. 1-13. APA.

23. Morsali, Seyedreza, et al. "Multi-physics simulation of metal printing at micro/nanoscale using meniscus-confined electrodeposition: Effect of environmental humidity." Journal of Applied Physics 121.2 (2017): 024903.

24. Jacak, Jaroslaw, Richard Wollhofen, and Thomas A. Klar. "Nanoscopic structuring with STED lithography (Conference Presentation)." SPIE Photonics Europe. International Society for Optics and Photonics, 2016.

25. Blees, Melina K., et al. "Graphene kirigami." Nature 524.7564 (2015): 204-207.

26. Buitrago, Elizabeth, et al. "From powerful research platform for industrial EUV photoresist development, to world record resolution by photolithography: EUV interference lithography at the Paul Scherrer Institute." SPIE Nanoscience+ Engineering. International Society for Optics and Photonics, 2016.

27. Rogers, J. A., M. G. Lagally, and R. G. Nuzzo. "Synthesis, assembly and applications of semiconductor nanomembranes." Nature 477.7362 (2011): 45.

28. Xu, S., Yan, Z., Jang, K.I., et al. "Assembly of micro/nanomaterials into complex, three-dimensional architectures by compressive buckling." Science 347.6218 (2015): 154-159.

29. Meitl, Matthew A., et al. "Transfer printing by kinetic control of adhesion to an elastomeric stamp." Nature materials 5.1 (2006): 33.

30. Yan, Zheng, et al. "Deterministic assembly of 3D mesostructures in advanced materials via compressive buckling: a short review of recent progress." Extreme Mechanics Letters 11 (2017): 96-104.

CHAPTER 2

STRATEGIES TO COMPLEX 3D GEOMETRIES

Significant portions of this chapter were published as: "A Mechanically Driven Form of Kirigami as a Route to 3D Mesostructures in Micro/Nanomembranes." by Yihui Zhang, Zheng Yan, Kewang Nan, *et al.*, *Proceedings of the National Academy of Sciences*, 112.38 (2015); "Controlled Mechanical Buckling for Origami-Inspired Construction of 3D Microstructures in Advanced Materials." by Zheng Yan, Fan Zhang, *et al.*, *Advanced Functional Materials*, 26.16 (2016); "Mechanical Assembly of Complex, 3D Mesostructures from Releasable Multilayers of Advanced Materials." by Zheng Yan, Fan Zhang, *et al.*, *Science Advances*, 2.9 (2016); "Engineered Elastomer Substrates for Guided Assembly of Complex 3D Mesostructures by Spatially Nonuniform Compressive Buckling." by Kewang Nan, Haiwen Luan, *et al.*, *Advanced Functional Materials*, 27.1 (2017); and "Mechanically-Guided Deterministic Assembly of 3D Mesostructures Assisted by Residual Stresses," by Haoran Fu, Kewang Nan, *et al.*, *Small*, 13.24 (2017). Reproduced with permission from the journals.

2.1 Introduction

Assembly of three-dimensional functional mesostructures (3DFMs) has important implications across broad areas of technology. The emerging mechanically-guided 3D assembly[1] relies on compressive buckling in narrow ribbons (i.e., structures with lateral aspect ratios of >5:1) or filaments to yield complex 3DFMs, but of primary utility in open-network mesh type layouts such as those in Figure 1.6. In this chapter, we present several strategies to greatly expand the accessible geometries to include (1) kirigami/origami-inspired membranes, (2) multi-layered 3DFMs, (3) locally-tunable 3DFMs, and (4) free-standing 3DFMs. For each strategy, the assembly

concepts and design principles are discussed. The utility of the finite element analysis (FEA) in the quantitative design processes are emphasized. Demonstrations include a diverse set of structures formed using mono-crystalline silicon, metal, polymer and their combinations, and the functional devices uniquely enabled by these strategies.

2.2 Kirigami/Origami-Inspired Membranes

The Attempts to directly apply the mechanically-guided assembly to membrane-type 2D precursors lead to "kink-induced" stress concentrations that can easily cause mechanical fracture (Figure 2.1a). In addition, the buckling of uniform 2D precursors does not allow well-controlled folding deformations and closed surfaces at desired local regions, as is essential to many applications[2-5]. To address these issues, this section presents strategies inspired by *kirigami* (Figure 2.1b) and *origami* (Figure 2.1c) - forms of ancient aesthetic pursuit - to enable broad and interesting 3DFMs consisting of membrane type layouts.

2.2.1 Assembly Concepts and Design Principles

Kirigami. Figure 2.2a presents the FEA and experimental results of the kirigami strategy[6] for assembly of 3DFMs from corresponding 2D nanomembranes of monocrystalline silicon. Here, photolithography and etching define patterns of *cuts* in these structures to yield enhanced flexibility in certain orientations, at specific locations. Compressive forces imparted in-the-plane at the bonding sites deform the systems into engineered 3D configurations via out-of-the-plane buckling. Detailed experimental procedures can be found in Section 2.6. The colors in the FEA results indicate the maximum principal strains during 3D formations, which peak at values well below the fracture thresholds for silicon (~ 1%), owing to the stress-reducing effects of the kirigami

cuts that form the narrow hinges between the sides. The cuts also play critical roles in defining the final 3D geometries. Figure 2.2b shows such examples in which repeated implementation of cross-cut patterns divide larger squares into smaller ones, resulting in fractal-inspired 3DFMs. In all cases examined herein, 2D precursors without carefully placed cuts tend to undergo sharp, localized deformations with associated stress concentrations that lead to fracture.

The experimental results exhibit excellent quantitative agreement with the FEA predictions in general, thereby establishing computation as a means for rapid design iterations. FEA can also reveal the dependence of the maximum principal strains on the prestrain in the elastomer substrate (ε_{pre}), as a function of geometric parameters related to the membrane structure and kirigami cuts, as shown in Figure 2.2c-f. Quantitative analyses of representative kirigami patterns (Figure 2.2c-d) with purely radial and circumferential cuts show that the maximum strains (ε_{max}) are proportional to the normalized thickness for silicon membrane, i.e. t/L, where L measures the overall dimension of the 2D precursor, and the square root of the compressive strain (ε_{compr}) applied to the 2D precursor, where $\varepsilon_{compr} = \varepsilon_{pre}/(1 + \varepsilon_{pre})$. Although the effect of the widths of the cuts (w_{cut}) cannot be captured with a simple scaling law, the qualitative dependence consistently involves a decrease in the maximum strain with an increase in w_{cut} (Figure 2.2e). This trend further highlights the critical, enabling role of kirigami concepts in this approach to 3D assembly. The effect of cut length (l_{cut}) is even more complicated, partly because this parameter significantly affects the nature of deformation modes in a qualitative sense, as shown in the FEA results of Figure 2.2f. These calculations indicate that the cuts must be sufficiently large (i.e. large w_{cut} and l_{cut}) to avoid stress concentrations. These qualitative and quantitative rules, together with the high accuracy in the FEA, provide a strong foundation for systematic engineering designs.

Origami. In the case of the o*rigami*-inspired strategy[7], we use a straight ribbon as a simple example to illustrate the overall design concept (Figure 2.3a). The key difference here is that the 2D precursor includes engineered variations in thickness to guide folding deformations at specific, targeted locations. In this example, the ribbon with length L between the bonding sites consists of five segments, two (in blue color, each with length L_1 and thickness t_1) of which are thicker than the other three (i.e. *creases*, in gray color, each with length L_2 and thickness t_2). When the thickness ratio (t_2/t_1) is relatively small, the thick segments undergo negligible deformation while the thin ones accommodate the compression via folding, simply due to the cubic downscaling of the bending stiffness with thickness. Furthermore, as the length ratio (L_2/L) decreases, the radius of curvature associated with this folded region decreases. Figure 2.3b illustrates these behaviors through FEA and experimental observations for various length and thickness ratios. These results indicate that the co-existence of small thickness ratios ($t_2/t_1 < 1/3$) and small length ratios ($L_2/L < 0.1$) can induce strong folding-type deformations in the creases. The borderlines of the scanning electron microscope (SEM) images are extracted and overlaid with corresponding FEA results (Figure 2.3c), and the folding angles of the creases as a function of the prestrain and the length ratio obtained theoretically and experimentally are plotted and compared (Figure 2.3d). The data provide quantitative evidence of the good agreements between FEA and experiments.

Since the overall compressive deformation is almost entirely accommodated by these creases, the maximum strains must also occur at these regions. Engineering designs that avoid fracture are important. For a straight ribbon with a small thickness ratio ($t_2/t_1 \leq 1/4$), the maximum principal strain (ε_m) in the buckled 3DFMs changes very slowly with further increase of t_2/t_1 (Figure 2.3e, left), indicating that ε_m becomes almost independent on t_2/t_1 for sharp creases. Due to the nature of bending deformation in the creases, ε_m follows a proportional dependence on the

normalized thickness (t_2/L_2) for a given prestrain (ε_{pre}), suggesting a general scaling law: $\varepsilon_m = F(\varepsilon_{pre})t_2/L_2$, where $F(\varepsilon_{pre})$ denotes a function that can be determined from FEA. This relation is well supported by FEA in the right frame of Figure 2.3e for $t_2/t_1 = 1/4$ and a wide range of t_2/L_2. Thus, reductions in the crease thickness (t_2) and increases in the crease width (L_2) act to reduce the maximum strains.

2.2.2 Diverse Geometries Enabled by Kirigami/Origami

Kirigami. The nature of the kirigami cuts in the 2D precursors provides the basis for a classification scheme: (i) membranes without any cuts (Figure 2.4a), (ii) membranes with symmetric cuts (Figure 2.4b), (iii) membranes with antisymmetric cuts (Figure 2.4c), and (iv) membranes with asymmetric cuts (Figure 2.4d). In addition, using the membrane and/or hybrid membrane–ribbon configurations as building blocks, arrays or nested architectures can be formed (Figure 2.4e). These 3DFMs are built from mono-crystalline silicon (grey, Figure 2.4) or photo-patternable epoxy (yellow, Figure 2.4).

Origami. A diverse range of basic origami-inspired geometries, each identified with a descriptive name, can be realized with these approaches as summarized in Figure 2.5a-b. These shapes range from semiellipsoids and starfish, to polyhedral topologies (e.g., cube, inverse pyramid, football, etc.), to those (“closed fan” and “skew tooth”) formed through creases organized circumferentially in an annulus. Concepts inspired by kirigami involve the addition of patterns of cuts to expand the accessible range of 3D structures. Complex integration of crease and cut patterns enable the formation of a “Ziggurat” architecture (Figure 2.5c) and a tri-floor building (Figure 2.5d) using commercially available plastic thin sheets.

2.3 Multi-Layered 3D Mesostructures

So far, the strategies only explore the buckling-driven assembly of 3DFMs from single-layer 2D precursors. This section presents the use of releasable, multilayered 2D precursors to enable the assembly of qualitatively different classes of 3DFMs, characterized by substantially enhanced filling factors[8]. The resulting 3DFMs have a level of geometric complexity unobtainable with single-layer 2D precursors reported previously. Furthermore, an application in antennas for near-field communication (NFC) technologies demonstrates the utility of transformable, 3D geometries from releasable, multilayered 2D precursors for enhanced quality (Q) factor and improved working angle compared to conventional, 2D counterparts.

2.3.1 Assembly Concepts and Representative Results

Figure 2.6a-b presents the fabrication and assembly processes for building multi-layered 3DFMs with a 3D trilayer nested cage. The key technique here is that the 2D precursors with different overall dimensions are stacked together in an aligned manner via layer-by-layer transfer printing[9-10]. Sacrificial layers (AZ 5214) patterned on top of each 2D precursor define positions of bonding sites and allow their subsequent release from one another. Detailed experimental procedures appear in Section 2.6. The initial and intermediate states of assembly obtained through FEA are shown in the left three frames of Figure 2.6b, indicating that each layer assembles independently without any interaction between layers during the buckling process. The color in the FEA illustrates the distribution of maximum principal strains, indicating that peak values remain well below the fracture thresholds for silicon (grey, Figure 2.6b) and for polymer (SU8; yellow, Figure 2.6b). This concept also enables other classes of multilayer designs, such as those

with entangled topologies (Figure 2.6c) and those with coherently coupled multilayers (Figure 2.6d).

2.3.2 NFC Devices with Enhanced Performances

The multi-layered 3D strategy enables a novel NFC device constructed with copper (9 μm)/polyimide (PI, 12 μm) bilayers and SiO_2 encapsulation (1 μm), as shown in Figure 2.7. Schematic illustrations of the multilayer 2D precursors are in Figure 2.7a, along with the final 3D configuration that results from a uniaxial compressive strain of 70%. The lower-layer ribbon and upper-layer spire are electrically connected at the center of the device. Figure 2.7b presents measurements and modeling results for the Q factor and inductance at a frequency of 13.56 MHz as a function of uniaxial strain ($\varepsilon_{x\text{-}appl}$) applied to the elastomeric substrate, for two devices with different widths (w) in the supporting ribbon. Although the inductance decreases slightly during the 2D-3D transformation, the resistance decreases sharply because of a relieved "proximity effect" in the 3D configuration, thereby leading to an enhancement in the Q factor. This result can also be understood from the reduction in energy losses associated with decreased coupling to the supporting metallic ribbon as the separation between the two layers increases. Both experimental measurement and theoretical modeling show these enhancements (~1.5 times for $w_{ribbon} = 1.03$ mm and ~1.8 times for $w_{ribbon} = 2$ mm) of Q factor in 3D devices ($\varepsilon_{x\text{-}appl} = 0\%$) over 2D counterparts ($\varepsilon_{x\text{-}appl} = 70\%$), as shown in Figure 2.7b. To provide further evidence of the underlying mechanism, the Q factors and inductances of NFC devices with a wide range of supporting ribbons widths (w from ~0.24 to 2 mm) appear in Figure 2.7c for both 2D and 3D geometries. These results indeed show a moderate reduction in Q factor with increasing width, and these reductions are smaller in the 3D devices than in the 2D counterparts. In an operational sense, the 3D spiral device provides

an improved output voltage, when wirelessly coupled to a commercial primary coil (Samsung Galaxy Note II), after addition of a capacitor for impedance matching. The left frame of Figure 2.7d summarizes computed voltages for 2D and 3D devices (w_{ribbon} = 2 mm) for a range of working angles (α, from 0° to 50°). The 3D device outperforms the 2D counterpart (for example, >2.2 times) for all angles. Moreover, broad tunability of the induced voltage can be achieved for different working angles, as shown by the middle frame of Figure 2.7d. The right frame of Figure 2.7d provides an experimental demonstration of the 3D device in lighting a commercial red light-emitting diode (LED), using the same NFC chip as in the previous studies with 2D coils[11-12].

2.4 Locally-Tunable 3D Mesostructures

The aforementioned strategies lack the ability to locally tuning the 3D geometries. This section presents two strategies, one of which involves the precise spatial control over the compressive assembly force through engineering the thickness distributions of the elastomer substrates[13]. The other exploits patterned thin films with well-defined residual stresses incorporated at strategic locations in the 2D precursor, as a means for reconfiguration of local regions[14]. These strategies can achieve topologies and/or functions inaccessible to other techniques, which are demonstrated with two functional devices.

2.4.1 Assembly Concepts and Design Principles

Substrate engineering. As opposed to the uniform elastomer substrates used in previous strategies, the elastomer substrate for the 3D assembly includes spatial variations in thickness (Figure 2.8a), created using the casting and curing procedures of soft lithography, in registry with the structures and bonding sites associated with the 2D precursor. The detailed experimental

procedures can be found in Section 2.6. The forces uniformly applied to the edges of the substrate lead to spatial patterns of strain that correlate to the variations in thickness, with smaller strains in thicker regions. This response follows simply from scaling of the tensile stiffness S of the substrate with thickness t, i.e., $S = E(\varepsilon)*t*b$, where E is the tangent modulus and b the width. Upon release of the prestrain, the degree of compressive buckling of the 2D precursor varies spatially in a corresponding manner, thereby leading to the formation of 3D structures with local variations. Figure 2.8b shows a simple example that consists of a buckled silicon ribbon that extends across the interface between thin and thick regions (thickness ratio = 1:4 and thickness of thin region = 0.4 mm) of an elastomer substrate. The periodicity (1.01 and 1.50 mm for the leftmost and the rightmost units, respectively) and amplitude (0.59 and 0.37 mm for the leftmost and the rightmost units, respectively) of the 3D structure are different across the thin and thick regions of the substrate, with an abrupt change at the interface. FEA simulations on strain distribution in the substrate (right frame, Figure 2.8b) indicate that under uniform, biaxial stretching of 70% at edges of the substrate, the strain value at the surface of the thin region ($\approx$76%) is more than four times that of the thick region ($\approx$17%). This effect leads to more compressive buckling in the thin regions than that in the thick regions.

Given a target uniaxial or biaxial strain distribution, the design procedure starts by arranging the overall layout and spacing of unit cells (either thickened or thinned) in the engineered substrate to approach the desired strain profile. The geometries and thickness ratios of the unit cells with respect to the surrounding uniform substrates are then determined carefully to refine details to the designed strain profile. In some cases, special features such as through-holes and trenches[13] can be used for generation of stepwise strain profiles.

Residual stress-assisted local reconfigurations. Figure 2.9a presents an example of residual-stress assisted local reconfigurations of a bi-floor 3D structure made of SU8 (thickness = 2 μm). Here, the key is to incorporate thin films with controlled residual stresses and patterned geometries, such as silicon nitride (SiN_x, 100 nm) onto the 2D precursor. Plasma-enhanced chemical vapor deposition (PECVD) of the SiN_x with control over parameters such as the direct current power, chamber pressure, gas flow rate, and operational frequency allows formation of thin films with well-defined residual stresses ranging from +480 to −581 MPa (+ and − indicates tensile and compressive residual stress, respectively). Detailed experimental procedures can be found in Section 2.6. In this example, the SiN_x resides only on top of the central ribbon (light blue, Figure 2.9a) to leverage the strain mismatch for controlling its bending direction during assembly. When the SiN_x layer has a sufficiently large tensile residual stress (e.g., +480 MPa), the center ribbon bends downward to minimize the strain energy. In contrast, this ribbon bends upward without the SiN_x, or with a layer of SiN_x that has a compressive stress (e.g., −580 MPa) or an insufficient tensile stress.

The bending direction (up or down) can be controlled by the residual stress ($\sigma_{residual}$), the thickness of the SiN_x (t_{SiNx}), and the thickness of the SU8 (t_{SU8}). Figure 2.9b presents a phase diagram in the space of $\sigma_{residual}$ and t_{SU8} for a given t_{SiNx} = 100 nm. Three different domains, denoted by "pop-up," "pop-down," and "unable to fully delaminate," can be identified. Here, to achieve full delamination of the 2D precursor from the substrate, t_{SU8} must be sufficiently large to provide separation forces that can overcome the van der Waals interactions at the weak interface with the substrate. The blue solid line in Figure 2.9b represents the boundary between the two different buckling modes. The minimum tensile residual stress of SiN_x necessary to achieve the pop-down buckling mode increases with the increasing SU8 thickness. For small stresses, the pop-up

buckling mode occurs. Experimental results based on precursors with various $\sigma_{residual}$ and t_{SU8} appear as numbered dots in Figure 2.9b. The resulted 3D configurations shown in Figure 2.9c agree well with the phase diagram. Note that the final 3D configurations for a given buckling mode (pop-down or -up) are mainly governed by the level of prestrain in the elastomer substrate and are insensitive to changes in $\sigma_{residual}$ and t_{SU8}.

In actual experiments, the points in the "pop-down" domain still has a finite probability of popping up because of experimental perturbations such as slight asynchronous release of the biaxial strain and/or parasitic adhesion/stiction at the non-bonding sites. The effect is studied using a statistical analysis based on observations from over 30 identical samples. Figure 2.9d shows that the probability of the pop-down mode decreases sharply as the points in the phase diagram moves from the "pop-down" domain to the "pop-up" domain.

2.4.2 Functional Devices Enabled by Local Tuning

Strain-insensitive 3D electronics. The ability to quantitatively tailor the strain distributions using engineered elastomer substrates gives rise to 3D electronics that are insensitive to in-plane tensile strain. Figure 2.10a demonstrates a 3D toroidal coil made of printed circuit board materials (polyimide film (25 μm) on copper foil (12 μm)) that is fully suspended from the substrate. The substrate in this case embraces a thickened center disc (3 mm in thickness) at which the 2D precursor is attached, and a relatively thin surrounding region (1 mm in thickness) (middle frame of Figure 2.10a). The thickness and area ratios of the two parts can be tuned such that during formation, the 3D coil only experiences ≈86% compression when a ≈300% biaxial compression is applied to the surrounding substrate. Due to this strain scaling effect, only ≈1/3 of the global strain will be sensed by the 3D coil upon biaxial stretching of the substrate, leading to small deformations

of the coil geometry, and thereby, negligible changes in its inductive properties (Figure 2.10b). As a comparison, the same toroidal coil formed on uniform substrate experiences significantly larger deformations upon 30% biaxial stretching, as demonstrated in right frame of Figure 2.10a. These and other features make these 3D electronics valuable for applications such as epidermal electronics[15-16] where parasitic impedance from substrate and motion-induced variance in electrical performances are undesired.

Mechanically tunable microbalance. The ability to local reconfigurations of 3D geometries represents another enabling strategy for novel 3D devices. Figure 2.11 provides an example in the form of a tunable microbalance for mass measurement. The design of the 2D precursor appears in Figure 2.11a. The part in light blue consists of a bilayer of SiN_x (100 nm) and SU8 (5 μm), and the other part (blue and red) consists of a single-layer of SU8 (10 μm). A tensile residual stress of 480 MPa in the SiN_x layer ensures that the central part pops down during assembly to facilitate the placement of microscale object for mass measurements (Figure 2.11b). A small mass (e.g., a few milligrams to tens of milligrams) placed on the plate deforms the structure downward by an amount that can be recorded by a nanoindenter (see Section 2.6 for details). The relationship between mass and displacement can be calibrated by experimental results and numerical simulations. Figure 2.11c illustrates a linear relationship between the displacement and mass. The upper limit of the measurement range corresponds to the maximum mass allowed before inducing physical contact between the microbalance and the substrate. FEA results in Figure 2.11d-e demonstrate that this limit can be adjusted by changing the prestrain, or equivalently, by stretching the underlying substrate after 3D assembly. This type of device might find use in microfluidic systems for

monitoring and separation of colloidal silica microparticles with the radius on the order of hundreds of microns[17-18].

2.5 Conclusions

This chapter present novel micro/nanofabrication strategies to 3DFMs, such as kirigami/origami-inspired processes, layer-by-layer assembly, elastomer substrate engineering, and residual stress-assisted local reconfigurations. Together with quantitative design tools such as FEA, they provide immediate access to diverse 3D geometries with broad-ranging critical dimensions and material compositions. The resulting engineering options in 3DFMs have sweeping implications for construction of advanced micro/nanosystems technologies. Additional opportunities may follow from the use of these concepts with fully formed devices, such as waveguides, light sources, and integrated circuits, and/or with 3D structures formed using complementary techniques in 3D printing.

2.6 Methods

Finite element analysis. The calculations used linear buckling analyses of 2D precursor structures under compression to determine the critical buckling strains and corresponding buckling modes. These results served as initial geometric imperfections for post-buckling simulations. Eight-node 3D solid elements and four-node shell elements were used for the substrate and 2D precursor structure, respectively, with refined meshes adopted to ensure the accuracy. The elastic modulus (E) and Poisson's ratio (v) are $\underline{E}$ = 166 kPa and v = 0.49 for the elastomer substrate; E = 130 GPa and v = 0.27 for silicon; and E = 4.02 GPa and v = 0.22 for SU8.

Fabrications of kirigami/origami-inspired 3DFMs. Preparation of 3D silicon structures began with patterning of 2D precursors with *cuts* for kirigami in the top silicon layer of a silicon-on-insulator (SOI) wafer (device silicon thickness from 300 nm to 1.25 μm) by photolithography and reactive ion etching (RIE). To realize *creases* for origami, photolithography was used to pattern an additional layer of photo-patternable epoxy (SU8, thickness from 300 nm to 3.5 μm) at the non-crease regions to increase their thickness. Immersion in buffered oxide etchant (BOE, 6:1) removed the buried silicon dioxide (SiO_2) layer from the exposed regions and also slightly from under the edges of the patterns at their periphery. Next, spin casting and photolithography formed patterns of a photoresist (AZ5214, thickness = 1.6 μm) to define the bonding sites. Immersion in concentrated hydrofluoric acid (HF, 49%) completed the removal of the buried oxide by complete undercut etching. The photoresist at the edge regions tethered the silicon structures to the underlying wafer. A thin layer of SiO_2 (thickness ~ 50 nm) was deposited on the sample by electron beam evaporation. Retrieving the structures onto a slab of polydimethylsiloxane (PDMS) (Sylgard 184 silicone elastomer, 1:4) and then transferring them to a water-soluble tape [polyvinyl alcohol (PVA)] oriented the 2D precursors with their top sides facing up, supported by the PVA. Exposing these precursors and a thin silicone elastomer (Dragon Skin, Smooth-On, 0.5 mm in thickness) to UV-induced ozone (UVO) yielded hydroxyl termination on their surfaces. A mechanical stage allowed controlled stretching of the silicone to well-defined levels of prestrain (either uniaxial or biaxial). Laminating the PVA tape with the precursors onto the silicone followed by baking in an oven at 70 °C for 7 min yielded strong covalent bonds between the silicone and the exposed regions of the silicon. Washing with hot water and then acetone dissolved the PVA tape and the photoresist sacrificial layers. Slowly releasing the prestrain completed the 3D assembly process.

Preparation of 3D epoxy structures started with thermal oxidation to form a layer of SiO_2 (thickness ~ 500 nm) on a silicon wafer. Next, spin casting and photolithography formed 2D precursors of SU8 (thickness from 300 nm to 3.5 μm) with *cuts* for kirigami on the SiO_2. To realize *creases* for origami, photolithography was used to pattern an additional layer of SU8 (thickness from 300 nm to 3.5 μm) at the non-crease regions to increase their thickness. Immersion in BOE removed the SiO_2 from the exposed regions and also slightly from under the edges of the SU8. Next, spin casting and photolithography formed patterns of photoresist (AZ5214, thickness = 1.6 μm) to define the bonding sites. Immersion in HF eliminated the remaining SiO_2 by complete undercut etching. A thin layer of SiO_2 (thickness ~ 50 nm) was deposited on the sample by electron beam evaporation. Transfer and bonding steps similar to those used for the silicon structures followed by release of the prestrain completed the assembly process.

Preparation of 3D structures in commercially available plastic sheets began with laser cutting of a base layer (≈75 μm in thickness) into desired patterns, followed by cutting of patterns to define the thick regions with additional layers of this same material. Adhering additional layers of plastic films onto the base layer through thin, stick double-coated tape (9080A, 3M, Minnesota, USA) yielded 2D precursors for assembly using a pre-stretched silicone substrate. A highly viscous, organic adhesive, i.e., an RTV silicone rubber (706, NAN DA, Jiangsu, China), dispensed at desired locations on the 2D precursors resulted in strong bonding to the silicone substrate, after curing for ≈2 h at room temperature. Slowly releasing the prestrain in the substrate completed the assembly process.

Fabrications of multi-layered 3DFMs. The fabrication procedures of individual 2D precursors made of mono-crystalline silicon and epoxy (SU8) followed those described in previous section.

A transfer printing tool and soft, elastomeric stamps of polydimethylsiloxane (Sylgard 184, Dow Corning) enabled alignment and stacking of 2D precursors with various configurations, feature sizes, and materials in a layer-by-layer fashion. The resulting multi-layered 2D precursors were delivered to a water-soluble (PVA) tape. The 3D assembly procedures then followed those described in previous section.

Fabrications and characterizations of the 3D NFC device. The 3D NFC devices were formed using 2D precursors defined in copper (9 μm)/PI (12 μm) (AC 091200EV, DuPont) by laser cutting. Plasma-enhanced chemical vapor deposition through a shadow mask formed a layer of SiO_2 (1 μm) on the copper at nonbonding areas, to serve as an encapsulation layer. A transfer printing tool yielded stacked bilayer 2D precursors that were then delivered onto a piece of PVA tape with the copper side facing downward. Deposition of SiO_2 (50 nm) by electron beam evaporation through a shadow mask defined the bonding sites, subsequently activated by exposure to UV-ozone. Removing the shadow mask and laminating the patterns onto a pre-stretched elastomer substrate (Dragon Skin, Smooth-On) followed by elimination of the PVA with hot water prepared the structure for 3D assembly. A fast-drying silver paint (Electrodag 1415M, Ted Pella) connected the top layer coil and bottom layer ribbon. Two electrical contact pads were connected to SubMiniature version A connectors by lead solder. The inductance and resistance of the NFC devices were characterized at 13.56 MHz using a radio-frequency impedance/material analyzer (Hewlett-Packard, 4291A).

Fabrications of engineered elastomer substrates. Fabrication of engineered substrate began with formation of the mold by 3D printing (Stratasys Objet350 Connex3 printer). A thin layer of

silicone mold release (Stoner S206) was applied to the mold surface before each use. Precursors to a low modulus, high elongation silicone material (Dragon Skin 10) were mixed and slowly poured onto the mold to fill all the surface cavities. After curing at room temperature for ≈10 h, extra silicone on the edges was carefully trimmed by a razor blade to render a flat surface. This defined isolated, thick portions of the engineered substrate. Spin casting of a second layer of silicone precursors and room - temperature curing for another 10 h defined thin portions of the engineered substrate that also connected the previously formed thick portions. Peeling the piece of cured elastomer away from the mold completed the fabrication of the engineered substrate.

Fabrications of 3DFMs with SiN_x layer. Electron beam evaporation formed a bilayer of 5 nm of chromium and 100 nm of gold on a clean silicon wafer at pressures between 0.7 and 3.4 μTorr, and at rates of 0.5–0.7 and 0.9–1.2 Å/s, respectively. Following deposition, loading the wafer into a dual-frequency PECVD tool enabled deposition of 100 nm of SiN_x, either at high or low frequencies to generate films with tensile or compressive stresses, respectively. Specific details of how the growth parameters affect the residual stresses in SiN_x appear in Figure 2.12. Specifically, tensile stress follows from low density Si-N bonds that stretch to interact with each other, which occurs primarily under high frequency deposition condition; compressive stress follows from low-frequency and high-power conditions which result in excess amine and other fragments. Photolithographically patterning AZ5214 photoresist and then etching away the exposed regions of the SiN_x using CF_4 reactive ion etching, backstopped by the gold sacrificial layer, yielded desired geometries in the stressed layer. A barrel plasma etcher with O_2 gas at 500 W for 3 min removed the photoresist.

Next, spin casting and photolithography aligned and formed 2D precursors of SU8 on SiN_x layers. A thin layer of adhesion promoter (Omnicoat, MicroChem) was applied between SiN_x and SU8 to promote strong adhesions. Immersion in gold etchant removed the gold from the exposed regions and also slightly from under the edges of the SU8. Next, spin casting and photolithography formed patterns of photoresist (AZ5214, thickness = 1.6 μm) to define the bonding sites. Immersion in gold etchant overnight eliminated the remaining gold by complete undercut etching. A thin layer of SiO_2 (thickness ~ 50 nm) was deposited on the sample by electron beam evaporation. The transfer and 3D assembly procedures then followed those described in previous section.

2.7 Figures

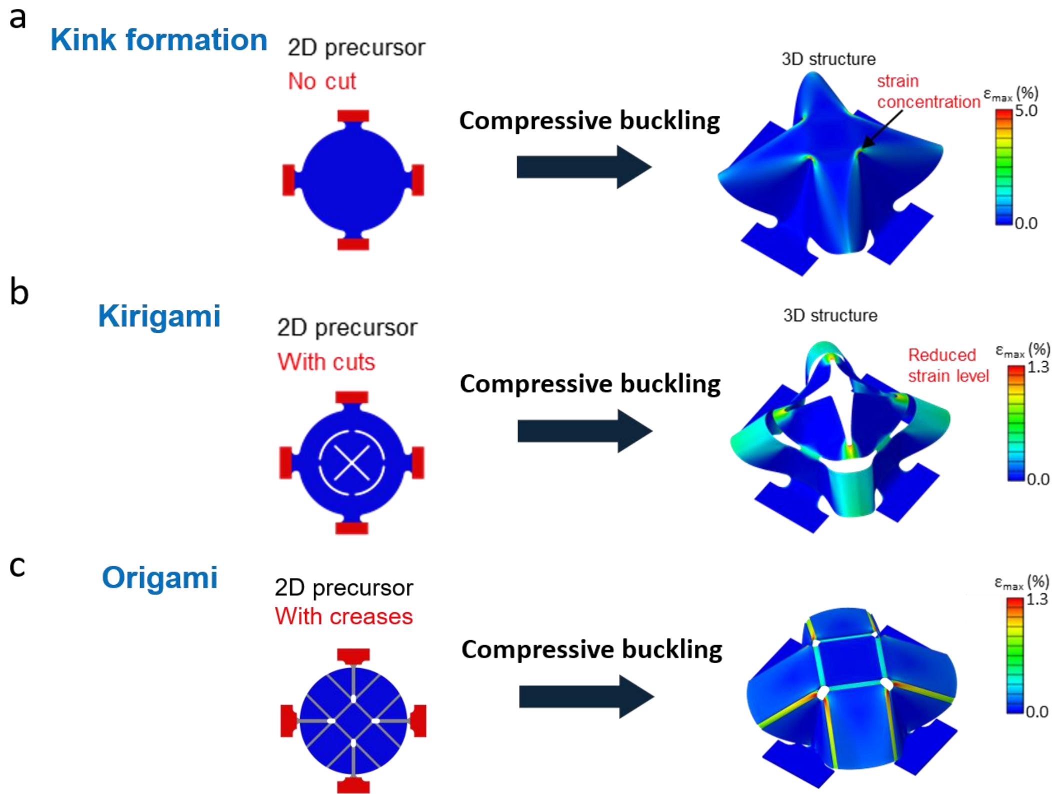

Figure 2.1 General concepts of kirigami- and origami-inspired 3DFMs. (a) Modeling results of direct 3D assembly of a solid 2D membrane that leads to kink-induced strain concentrations. (b) Modeling results of 3D assembly of a 2D precursor similar to (a), but now with strategic, kirigami-inspired *cuts* to avoid strain concentrations. (c) Modeling results of 3D assembly of a 2D precursor similar to (a), but now with strategic, origami-inspired *creases* to avoid strain concentrations and create folding patterns.

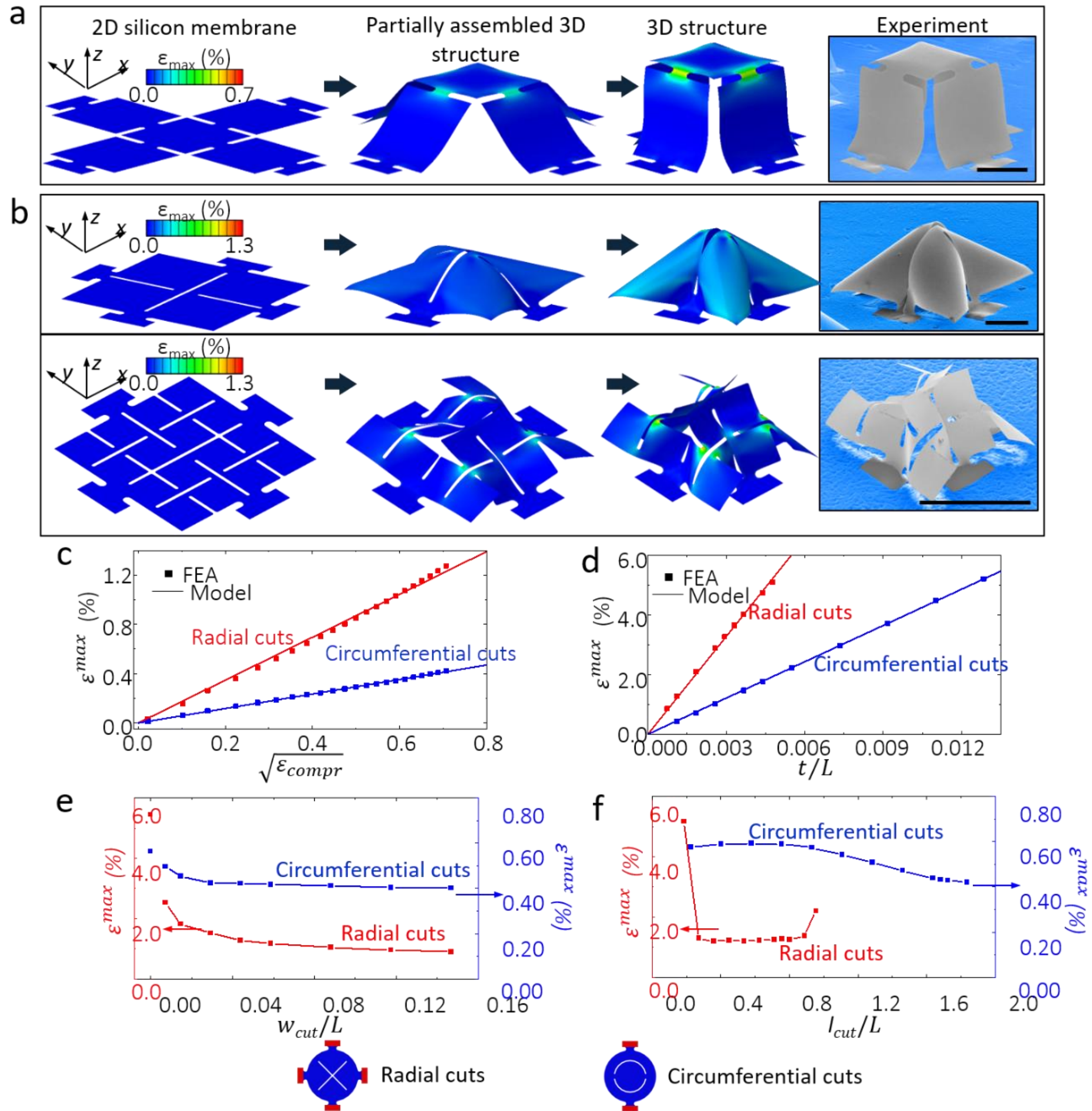

Figure 2.2 Concepts and design principles of kirigami-inspired 3DFMs. (a) FEA and experimental results of a kirigami-inspired 3D membrane structure made of silicon. (b) FEA and experimental results of 3D membrane structures made of silicon due to different 2D fractal cut patterns. (c)-(f) Computed maximum strains (ε_{max}) in the 3DFMs as a function of the square root of the compressive strain (ε_{compr}), the normalized thickness for silicon membrane, the normalized width of the cuts, and the normalized length of the cuts, respectively. Scale bars = 200 µm. Reproduced from reference 6.

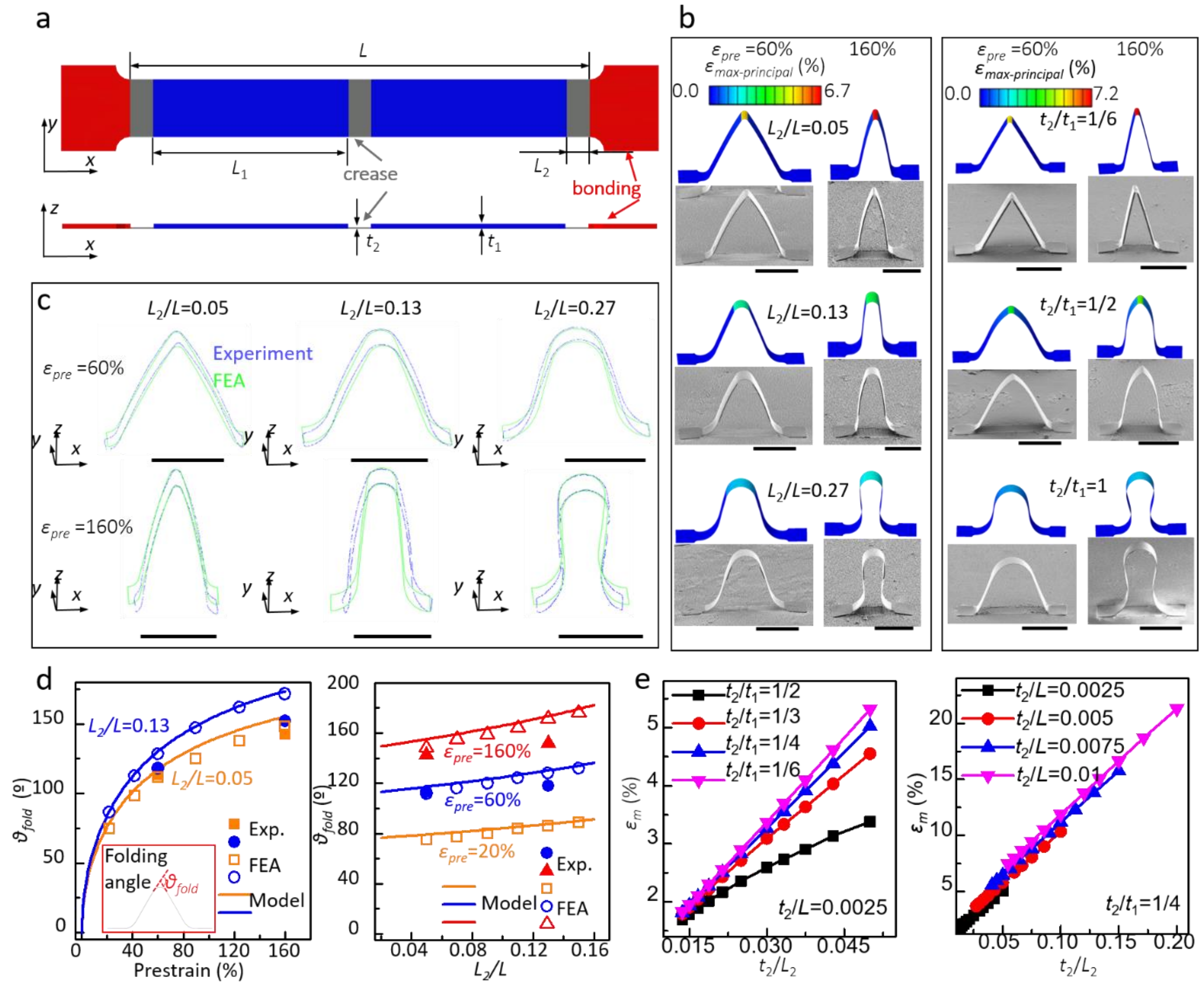

Figure 2.3 Concepts and design principles of origami-inspired 3D structures. (a) Design of the simple ribbon structure to demonstrate the origami concept. (b) FEA and experimental results of 3D ribbons in (a) with different *crease* length and thickness ratios. (c) Overlaid boundaries from experiments and FEA to show good agreement between the two. (d) Folding angles as a function of prestrain (left) and crease length ratios (right) from experiments and FEA to show good agreement between the two. (e) Computed maximum strains (ε_m) in the 3D structures as a function of the normalized thickness of the creases, at different crease thickness ratios (left) and crease normalized thickness (right). Scale bars = 200 μm. Reproduced from reference 7.

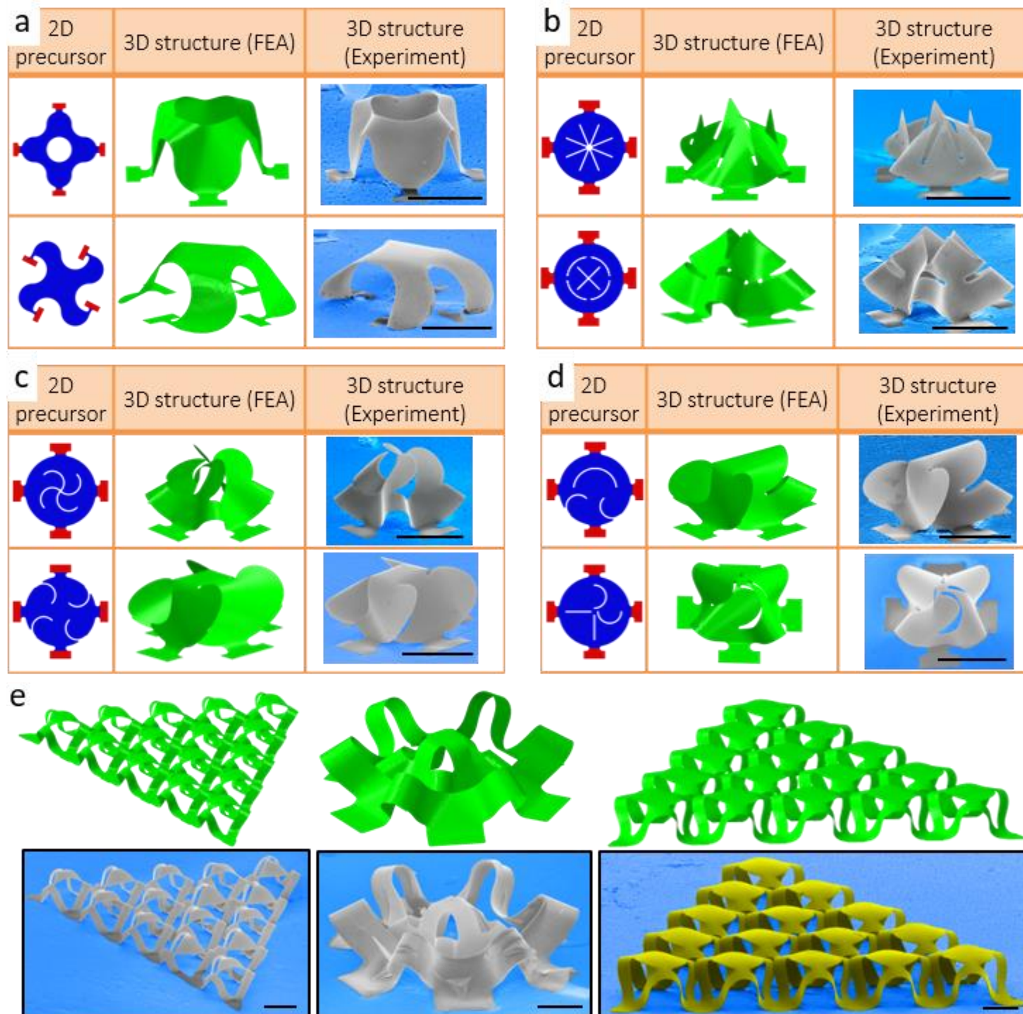

Figure 2.4 Representative experimental results of kirigami-inspired 3DFMs. (a) Membranes without any cuts. (b) Membranes with symmetric cuts. (c) Membranes with antisymmetric cuts. (d) Membranes with asymmetric cuts. (e) Arrays and nested architectures using membrane and/or hybrid membrane–ribbon configurations as building blocks. Scale bars = 200 µm. Materials color code: grey = mono-crystalline silicon, yellow = SU8. Reproduced from reference 6.

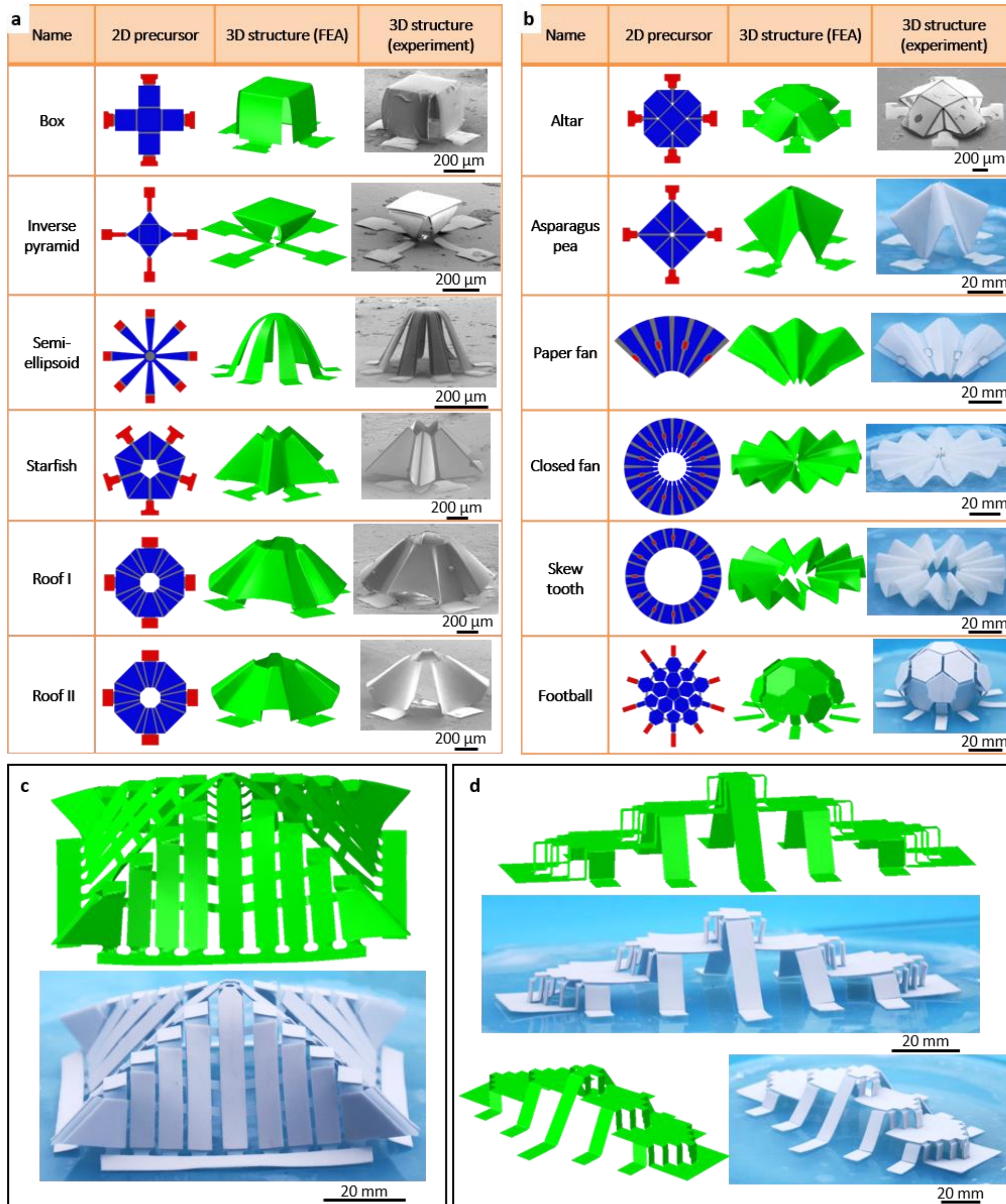

Figure 2.5 Representative experimental results of origami-inspired 3DFMs. (a) (b) A diverse range of basic origami-inspired geometries, each identified with a descriptive name. (c) (d) Examples of complex integration of crease and cut patterns: a "Ziggurat" architecture (c) and a tri-floor building. Structures 1, 5 and 6 in (a) are made of silicon/SU8; structures 2-4 in (a) and structure 1 in (b) are made of SU8; the remaining structures are made of commercially available plastic sheets. Reproduced from reference 7.

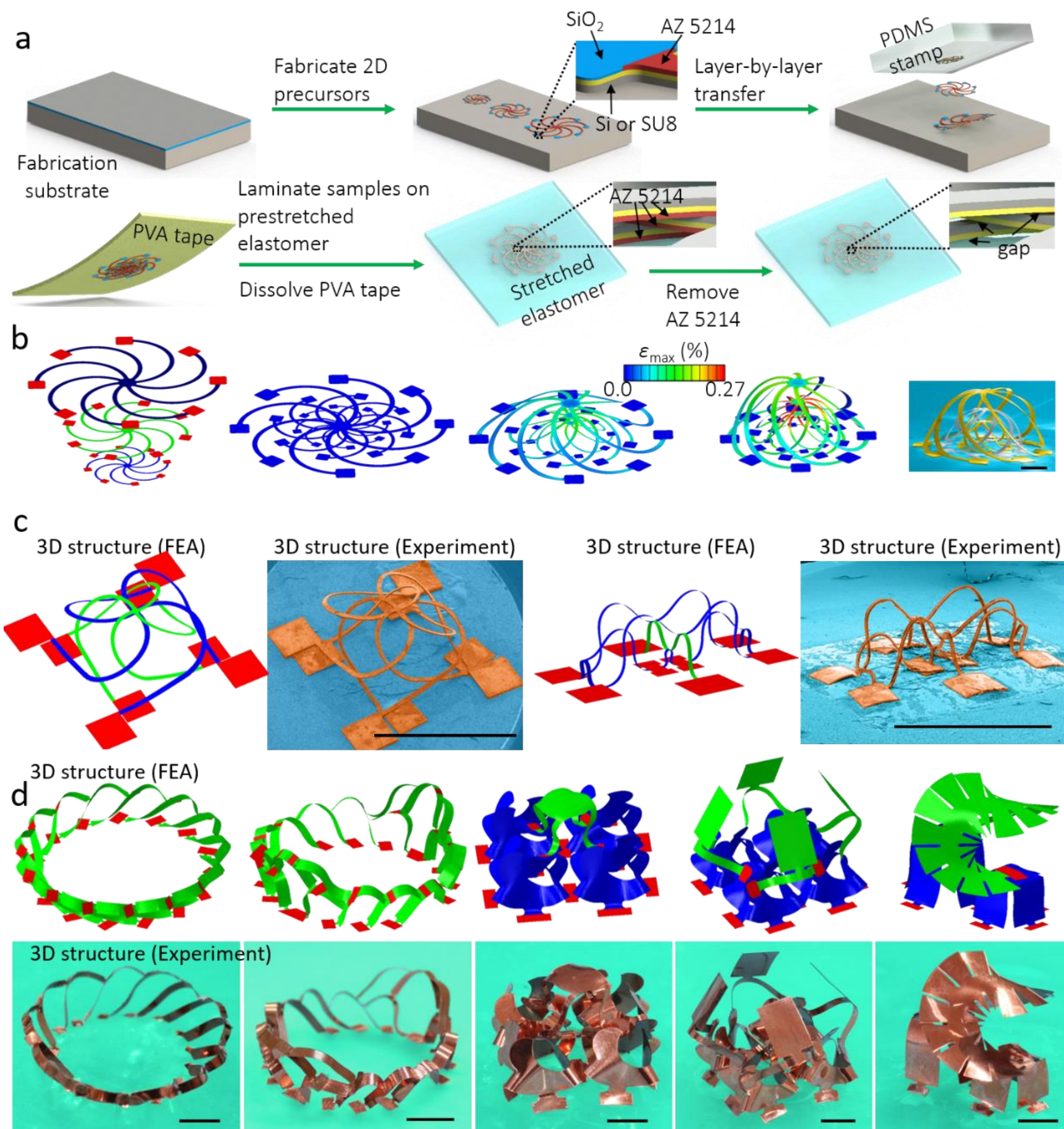

Figure 2.6 Multi-layered 3DFMs. (a) Schematic illustration of the fabrication procedures. (b) FEA (left) and experimental (right) results of a 3D trilayer nested cage. (c) 3DFMs with entangled topologies. (d) 3DFMs with coherently coupled multilayers. Scale bars = 400 μm for (b), = 3 mm for (c), and = 5 mm for (d). Materials color code: yellow = SU8, grey = mono-crystalline silicon, orange = copper, brown = commercially available PET film. Reproduced from reference 8.

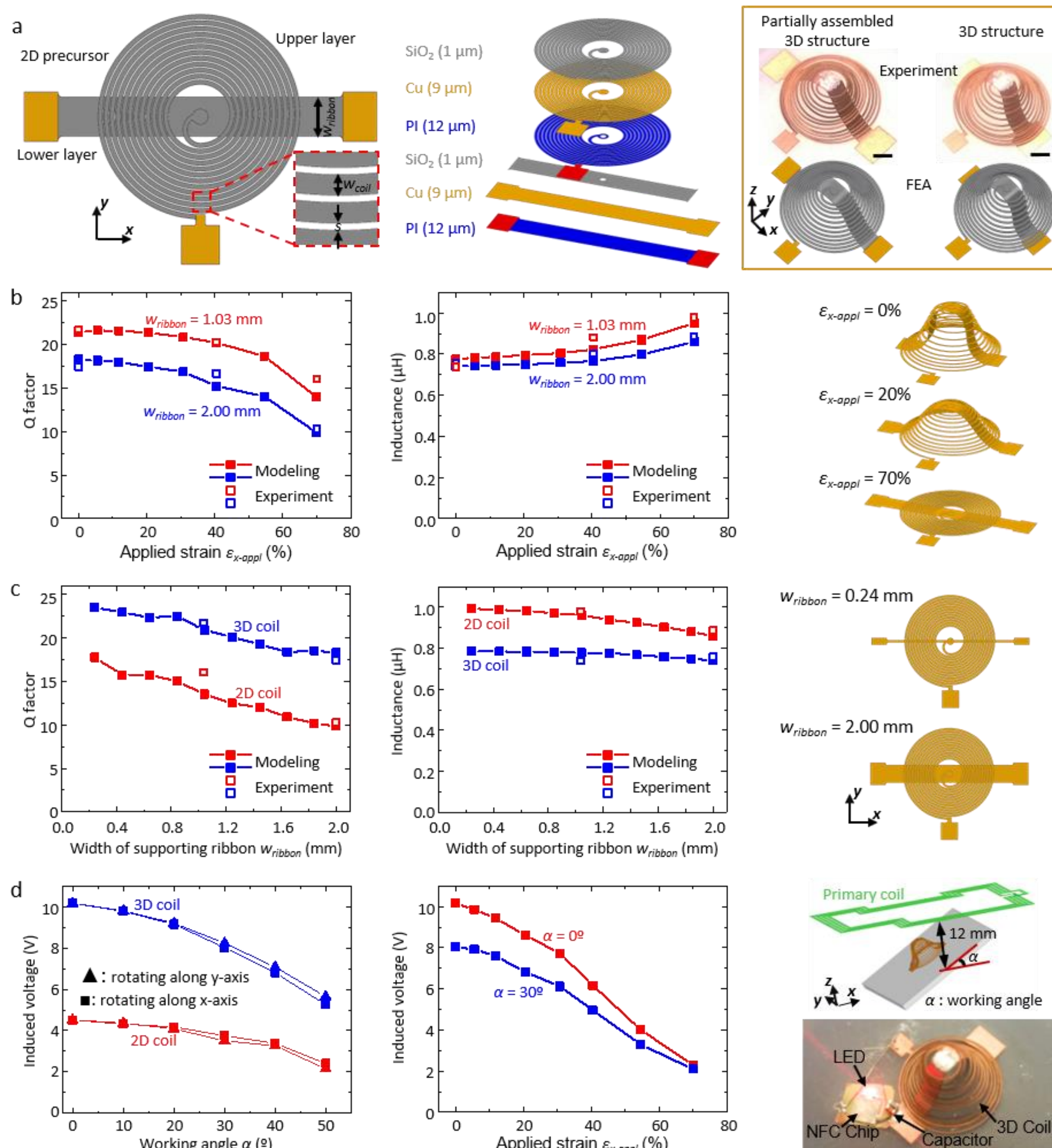

Figure 2.7 The NFC device enabled by the multi-layered 3D strategy. (a) Schematic illustration of the multilayer 2D precursors, an exploded view to show the layer construction, and the corresponding 3D configurations. Scale bars = 2 mm. (b) Measured and computed dependence of the Q factor and inductance on the applied strain for devices with two different widths (1.03 and 2.00 mm) in the supporting ribbon. The right frame corresponds to the FEA results of 3D configurations for the NFC device under different levels of applied strain (0, 20, and 70%). The

Figure 2.7 (cont.) other geometric parameters are fixed as coil width = 222 μm, coil turn = 82 μm, and turn number = 12. (c) Measured and computed results for the Q factor and inductance versus the width of supporting ribbon for both the 2D and 3D devices with the same coil width, coil turn, and turn number as in (b). (d) Computed results of the induced voltage as a function of the working angle and the applied strain, when the devices are coupled with a commercial primary coil, as schematically shown in the right top frame. The right bottom frame corresponds to an optical image demonstrating the use of the 3D NFC device for lighting a commercial red LED. The coil width, coil turn, and turn number are the same as in (b). Reproduced from reference 8.

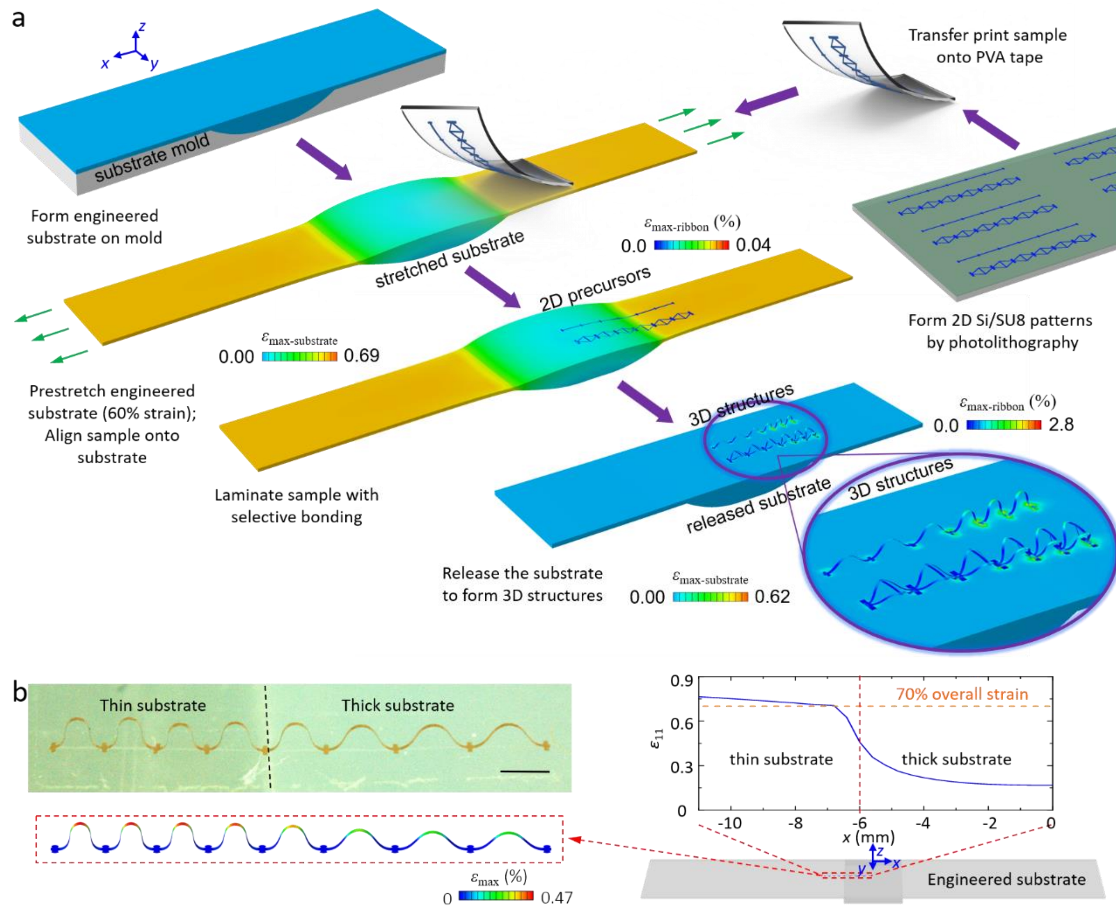

Figure 2.8 Local tuning of the 3D geometries by substrate engineering. (a) Schematic illustration of the general procedures. (b). An example 3D silicon ribbon that extends across the interface between thin and thick regions of an elastomer substrate (left), and the FEA results of strain distribution in the substrate (right) indicating the strain value at the surface of the thin region (≈76%) is more than four times that of the thick region (≈17%). Scale bar = 1 mm. Reproduced from reference 13.

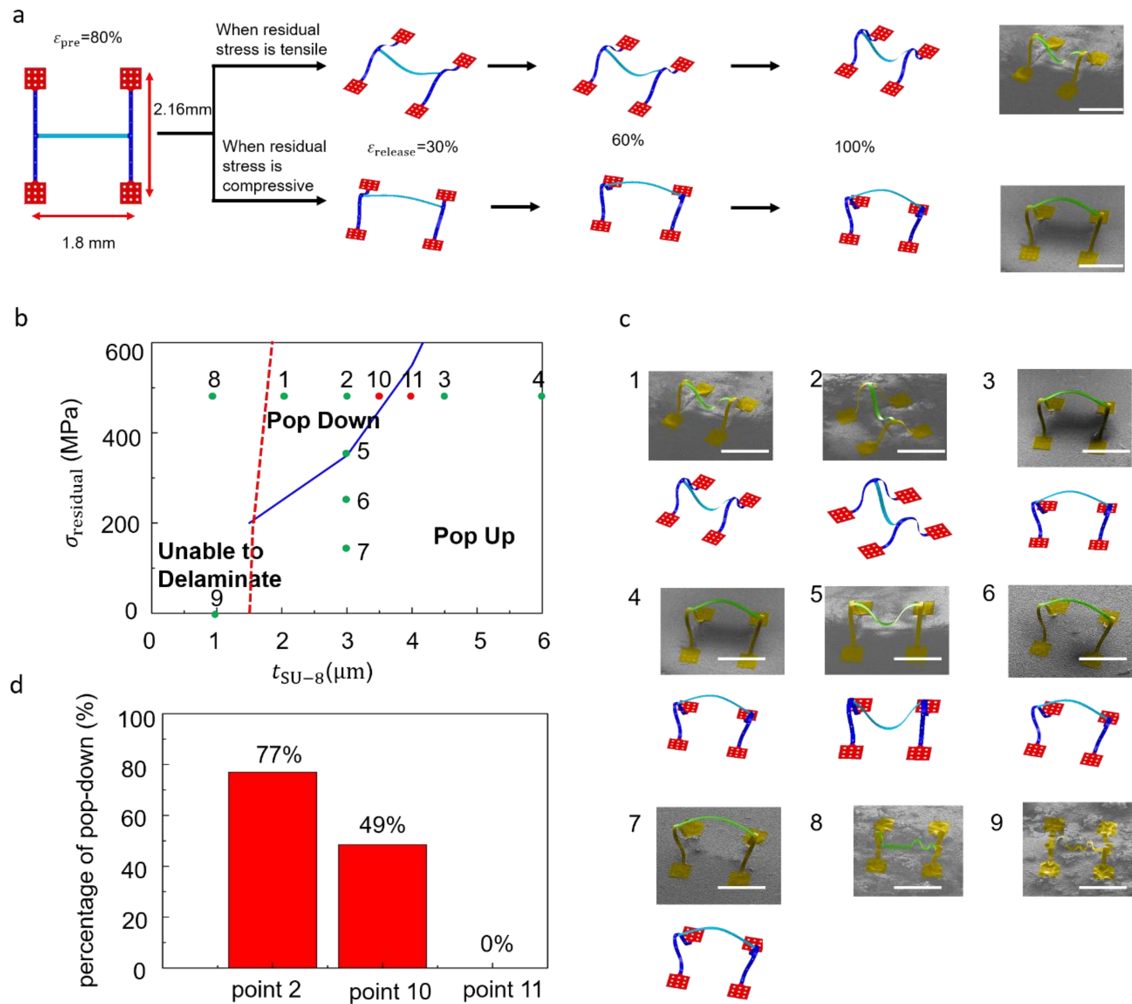

Figure 2.9 Local tuning of the 3D geometries by residual stresses. (a) Example of the SiN_x layer with residual stresses capable of local reconfigurations into a new 3D geometry. (b). A phase diagram showing the "pop down", "pop up" and "unable to delaminate" domains for the 3DFMs in (a). (c) Experimental results that validate the phase diagram in (b). (d) The actual probability for reconfigurations to occur at different points in the phase diagram in (b). Scale bar = 1 mm. Reproduced from reference 14.

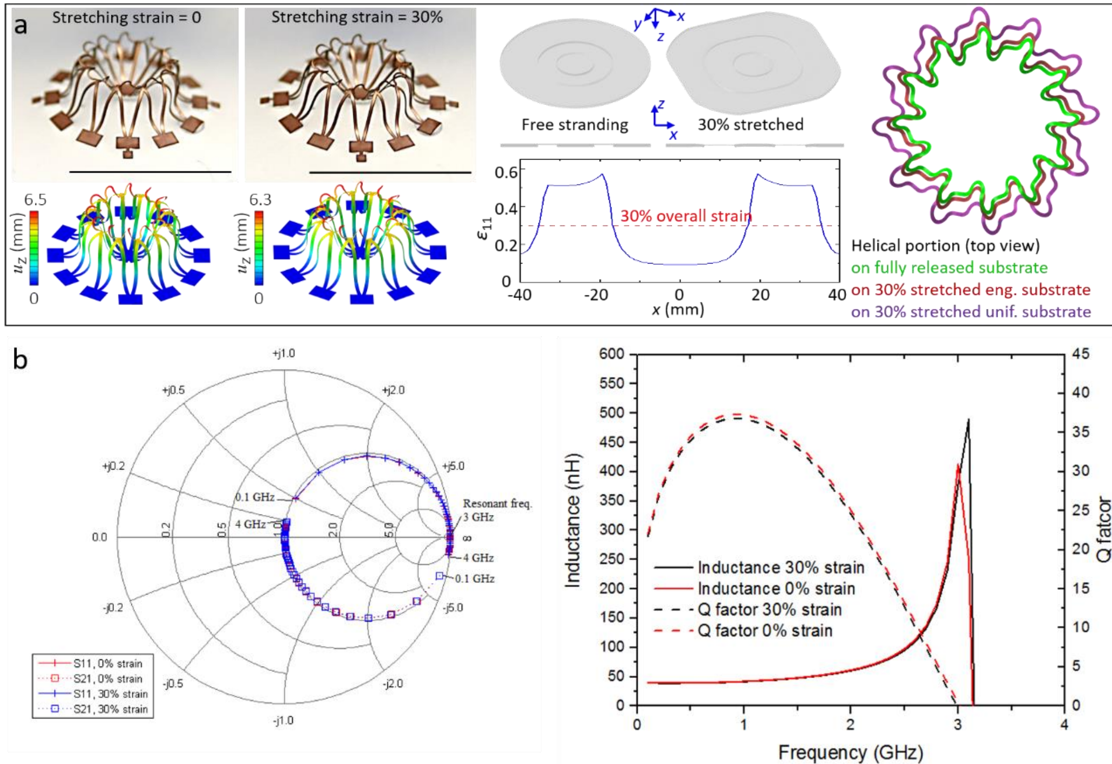

Figure 2.10 Strain-insensitive 3D electronics enabled by substrate engineering. (a) A 3D helical coil elevated from the substrate. The left two frames show the experimental and FEA results of the structure at 0% and 30% tensile strains. The middle frames show 3D and cross-sectional views of the substrate, as well as the magnitude of the x-direction normal strain for 30% applied biaxial strain. The right frame shows a top view of the helical coil upon 30% biaxial stretching, with and without the use of an engineered substrate. (b) Left frame: scattering coefficients (S11, S12) of the 3D helical coil formed on engineered substrate before and after 30% biaxial stretching to show that inductive properties are insensitive to tensile strain. Right frame: the resulted inductance and Q factor before and after stretching are close to each other. Scale bars = 1 cm. Reproduced from reference 13.

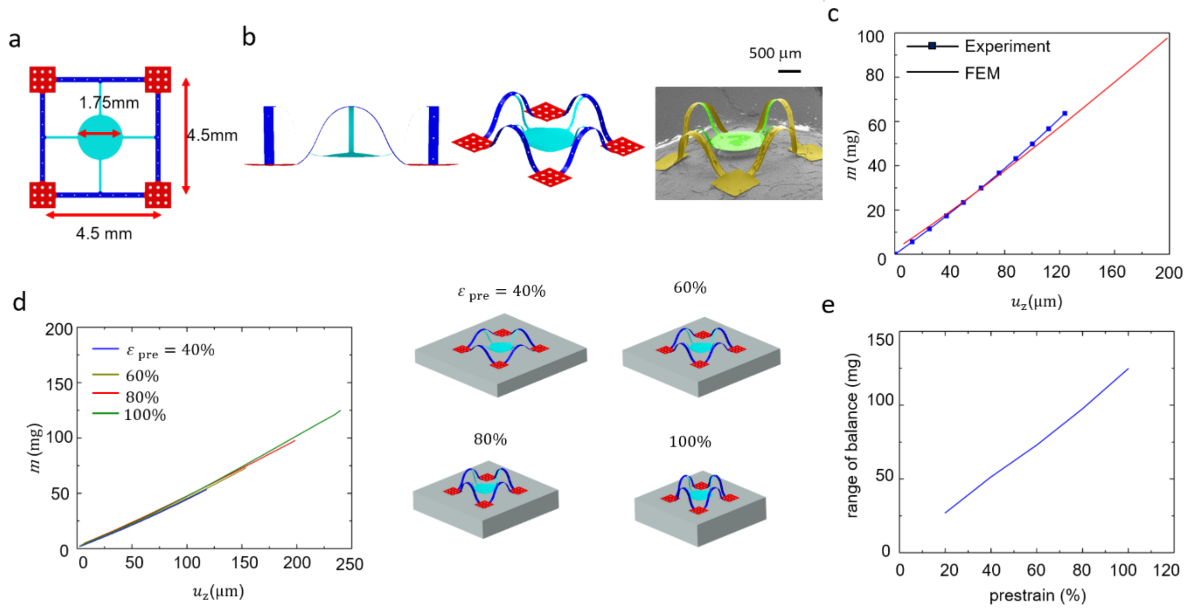

Figure 2.11 Mechanically-tunable microbalance enabled by local reconfigurations. (a) 2D precursor for the device. (b) FEA prediction and SEM images from two different viewing angles. (c) Measured and computed dependence of the mass on the vertical displacement. (d) Mass versus vertical displacement for devices assembled with four different levels of prestrain, along with their corresponding 3D configurations. (e) The range of the microbalance as a function of the prestrain. Reproduced from reference 14.

SiNx Film	A	B	C	D	E
Power (W)	20	20	60	60	20
Pressure (mTorr)	900	900	900	550	750
SiH4 flow (sccm)	40	60	60	60	30
NH3 flow (sccm)	60	60	60	60	20
Frequency	13.56 MHz	13.56 MHz	13.56 MHz	13.56 MHz	380 kHz
Stress* (MPa)	(+)480±10	(+)368±32	(+)263±23	(+)180±46	(-)581±51

*Stress is measured using a FSM film measurement tool, thickness is measured prior to this using an ellipsometer. Sample set of n=3.

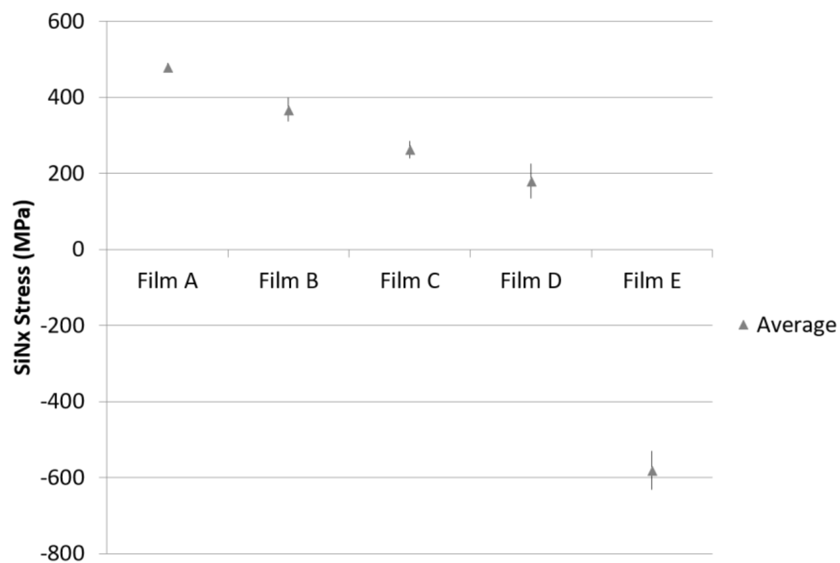

Figure 2.12 Effects of the growth parameters on the residual stresses in SiN_x. Reproduced from reference 14.

2.8 References

1. Xu, S., Yan, Z., Jang, K.I., et al. "Assembly of micro/nanomaterials into complex, three-dimensional architectures by compressive buckling." Science 347.6218 (2015): 154-159.

2. Bishop, David, et al. "Silicon micro-machines for fun and profit." Journal of Low Temperature Physics 169.5-6 (2012): 386-399.

3. Ware, Taylor H., et al. "Voxelated liquid crystal elastomers." Science 347.6225 (2015): 982-984.

4. Liu, Yuhang, et al. "Aggregation and morphology control enables multiple cases of high-efficiency polymer solar cells." Nature communications 5 (2014): 5293.

5. Filipov, Evgueni T., Tomohiro Tachi, and Glaucio H. Paulino. "Origami tubes assembled into stiff, yet reconfigurable structures and metamaterials." Proceedings of the National Academy of Sciences 112.40 (2015): 12321-12326.

6. Zhang, Yihui, et al. "A mechanically driven form of Kirigami as a route to 3D mesostructures in micro/nanomembranes." Proceedings of the National Academy of Sciences 112.38 (2015): 11757-11764.

7. Yan, Zheng, et al. "Controlled mechanical buckling for origami - inspired construction of 3D microstructures in advanced materials." Advanced functional materials 26.16 (2016): 2629-2639.

8. Yan, Zheng, et al. "Mechanical assembly of complex, 3D mesostructures from releasable multilayers of advanced materials." Science advances 2.9 (2016): e1601014.

9. Carlson, Andrew, et al. "Transfer printing techniques for materials assembly and micro/nanodevice fabrication." Advanced Materials 24.39 (2012): 5284-5318.

10. Meitl, Matthew A., et al. "Transfer printing by kinetic control of adhesion to an elastomeric stamp." Nature materials 5.1 (2006): 33.

11. Kim, Jeonghyun, et al. "Epidermal electronics with advanced capabilities in near - field communication." small 11.8 (2015): 906-912.

12. Kim, Jeonghyun, et al. "Miniaturized Flexible Electronic Systems with Wireless Power and Near - Field Communication Capabilities." Advanced Functional Materials 25.30 (2015): 4761-4767.

13. Nan, Kewang, et al. "Engineered elastomer substrates for guided assembly of complex 3D mesostructures by spatially nonuniform compressive buckling." Advanced functional materials 27.1 (2017).

14. Fu, Haoran, et al. "Mechanically - Guided Deterministic Assembly of 3D Mesostructures Assisted by Residual Stresses." small 13.24 (2017).

15. Kim, Dae-Hyeong, et al. "Epidermal electronics." science 333.6044 (2011): 838-843.

16. Yeo, Woon - Hong, et al. "Multifunctional epidermal electronics printed directly onto the skin." Advanced Materials 25.20 (2013): 2773-2778.

17. Mark, Daniel, et al. "Microfluidic lab-on-a-chip platforms: requirements, characteristics and applications." Microfluidics Based Microsystems. Springer, Dordrecht, 2010. 305-376.

18. Chin, Curtis D., Vincent Linder, and Samuel K. Sia. "Commercialization of microfluidic point-of-care diagnostic devices." Lab on a Chip 12.12 (2012): 2118-2134.

CHAPTER 3

TOWARDS MICRO-ROBOTICS

Significant portions of this chapter were published as: "Morphable 3D Mesostructures and Microelectronic Devices by Multistable Buckling Mechanics." by Haoran Fu, Kewang Nan, *et al.*, *Nature Materials*, 17.3 (2018); and "Three-Dimensional Mesostructures as High-Temperature Growth Templates, Electronic Cellular Scaffolds, and Self-Propelled Microrobots." by Zheng Yan, Mengdi Han, *et al.*, *Proceedings of the National Academy of Sciences*, 114.45 (2017). Reproduced with permission from the journals.

3.1 Introduction

The great diversity in geometries and the compatibility with high-performance electronic materials suggest potentials of the 3DFMs in micro-robotics. In this chapter, we present several studies towards this goal, including (1) the reversible shape transformations between different 3D geometries[1], and (2) freeing the 3DFMs from the assembling elastomer substrates[2]. The chapter concludes with a demonstration of 3D micro swimmers capable of controlled trajectories, which is the first working prototype of micro robots enabled by the mechanically-guided 3D assembly.

3.2 Reversible Shape Transformations

3DFMs with shapes that can be dramatically and reversibly altered between different configurations are important in a wide range of engineering applications, such as deployable space structures[3], biomedical devices[4], microelectromechanical systems (MEMS)[5], robots[6] and metamaterials[7]. Many such morphable 3D systems use designs inspired by the ancient arts of origami and kirigami, in part due to a myriad of shapes that can be achieved by actively folding

and unfolding thin sheets with pre-defined creases and cuts[7-9]. A different strategy exploits the foldability of prismatic geometries[10-11], where space-filling tessellations of polyhedra create reconfigurable 3D structures comprising a periodic assembly of rigid plates and elastic hinges. Although these design principles offer remarkable levels of freedom in reconfiguration and shape-defined mechanical responses, they in general apply to macroscopic structures and simple, non-functional materials. Methods that rely on residual stresses[12-13] or responsive materials (for example, shape memory polymers or hydrogels)[14-16] provide alternatives. Such approaches are not, however, readily applicable to high-performance, planar thin film materials or to micro- or nanoscale architectures. Significant opportunities remain in the development of schemes for realizing reconfigurable 3DFMs in classes of materials and with component device designs found in existing forms of electronics, optoelectronics and microelectromechanical systems.

We present a set of strategies and design concepts that first begin with assembly of 3DFMs using schemes that rely on biaxially prestrained elastomer substrates and 2D precursors similar to the previous work[17-22]. Here, we show that strategically selected release sequences and specially engineered precursor designs can trigger the stabilization of multiple, distinct 3D buckling modes, thereby providing capabilities for reversible reconfiguration in which the time sequence of strains applied to the elastomer platform serves as the control strategy. These options in morphable 3DFMs lie qualitatively beyond the scope of previously reported strategies. Fundamental studies of the bistability, and in general the multistability, behaviors inherent in the 2D-to-3D transformations of the systems reported here establish general rationales for designing 3DFMs with distinct, reconfigurable topologies. Experimental demonstrations of more than 20 examples, including complex objects with recognizable forms (for example, octopus, spider, bird, maple leaf, house and basket) illustrate the versatility of the approaches. An array of silicon n-channel metal-

oxide–semiconductor field-effect transistors (n-MOSFET) integrated onto a shape-shifting 3DFMs framework serves as an example in high-performance electronics. Passive radiofrequency (RF) circuits and concealable RF antennas highlight applications in reconfigurable 3D systems of potential relevance in wireless communications.

3.2.1 Route to Morphable 3D Mesostructures and Electronics

Figure 3.1a presents the key concepts in the context of a simple example that consists of a 3D vertical column with square cross-section that can be reconfigured into a socket-type shape, segmented into four strips. The initial formation of the column made of epoxy (SU8), referred to as shape I, relies on the mechanical assembly strategy described elsewhere[15-20] (see Section 3.6 for details). The narrow green regions that span the widths of the ribbons, oriented orthogonal to their lengths, correspond to segments with reduced thickness, i.e. the creases that help to determine the overall shape and the multistable buckling mechanics, as essential to capabilities in shape reconfiguration. This reconfiguration begins with application of an equal biaxial stretch ($\varepsilon_x = \varepsilon_y$) to the substrate to return the 3D column to the planar geometry, at $\varepsilon_x = \varepsilon_y = 100\%$ for this particular example. Next, release of the biaxial strain in a sequential manner, starting with ε_x and then followed by ε_y, reshapes the column into the socket shown in the right top frame of Figure 3.1a (shape II). Since the maximum principal strain in the polymer remains well below the yield strain of SU8, the entire process is reversible, meaning the two configurations can be reshaped into each other repetitively. Furthermore, any intermediate state during the reconfiguration process can be also maintained by holding the stretch at any level, thereby allowing control over the amplitudes of the displacements of either of the two modes. FEA predictions and experimental results on

mesostructures created using this loading-path control strategy show remarkably good agreement, for all scenarios examined.

Such classes of reconfigurable 3D mesostructures can be realized in a broad set of materials that lead to integrated devices. Figure 3.1b-d summarize an example that consists of an array of four silicon n-MOSFETs with electrodes and contact pads for electrical probing. The device is first fabricated in its planar form using conventional photolithography to define the various functional layers, such as transistors, electrodes, encapsulations, and oxides for bonding to the elastomer substrate (see Figure 3.1b and Section 3.6 for details). The initial assembly leads to a 3D tower-shaped structure with four supporting struts, capable of changing shape into a recessed well with similar struts (Figure 3.1c). As in the other examples, this shape change is reversible. Transistor measurements in Figure 3.1d show that the transistor characteristics remain unchanged by switching between these two different shapes.

Figure 3.1e-f provide another example that integrates multiple microscale light-emitting diodes (μ-LEDs) into a conducting framework that consists of a lithographically patterned multilayer of copper and polyimide (see Figure 3.1e and Section 3.6 for details). Here, a key aspect of the design is that the pattern of light emission can be reversibly modified not only through 3D geometric reconfiguration, but also through modification of the connectivity of the associated electrical circuits. Specifically, the circuit remains unchanged from the 2D configuration during simultaneous release, such that all four μ-LEDs light up in the resulted 3D device (shape I, Figure 3.1f). By contrast, the copper layers in the six suspended ribbons contact one another in the case of sequential release (shape II), thereby resulting in a different circuit connectivity. In this condition, only three outer μ-LEDs light up, while the central one is off. Such a system could

potentially find use in optoelectronic[23] and optogenetic[24] research, where on-demand spatial variations of light emission in small volumes can be valuable.

3.2.2 Underlying Mechanics and General Design Approach

Results of experiments and computational modelling suggest that only certain classes of 2D precursors lead to reconfigurable 3DFMs by this type of loading-path strategy. Energetic analyses of some specialized cases provide context for general, rule-based procedures for designing systems with multiple stable 3D modes, as an essential requirement for reconfigurability.

Figure 3.2a-f presents analysis of the type of geometry appeared in Figure 3.1a. Here, u_z is the out-of-plane displacement at the central, intersection point. E_I and E_{II} are the strain energies associated with shape I and shape II, respectively. Quantitative calculations (Figure 3.2b) show that although shape I has a much smaller strain energy (E_I) than shape II (E_{II}), both representing local minima in the overall energy landscape. The existence of an energy barrier ($E_{barrier} = E_{peak} - E_{initial}$) and a threshold energy difference ($E_{diff} = E_{II} - E_I$) determine the 3D buckling modes that form during assembly, where E_{peak} and $E_{initial}$ are the peak strain energy and the initial strain energy during the loading process, respectively. Specifically, E_{diff} determines the configuration to emerge upon release (that is, shape II for $E_{diff} < 0$ and shape I for $E_{diff} > 0$), and the mode transition can occur only when the energy barrier vanishes (that is, $E_{barrier} = 0$). For simultaneous release, both E_{diff} and $E_{barrier}$ are positive during the entire process, as shown in Figure 3.2c. In the absence of an external excitation sufficiently large to overcome the energy barrier, the 3D geometry remains in shape I. During the first stage of sequential release (strain in x direction from 100% to 0, while strain in y direction is 100%), only one configuration can occur, due to the constraint imposed by

the flat ribbon along the perpendicular (y) direction. During the second stage (strain in y direction from 100% to 0, while strain in x direction is 0), E_{diff} is initially negative (Figure 3.2c), thereby causing the 3D geometry to enter shape II that cannot switch back to shape I due to the presence of a positive energy barrier.

These observations suggest that the magnitude of the energy barrier (zero or positive) governs reconfigurability by sequential release. According to the scaling law for this energy barrier (see Appendix A. 1 and Appendix Figure A1 for details), a phase diagram (Figure 3.2d) can be obtained for the 2D precursor. Here, the regime above the pink curve gives the same configuration for simultaneous and sequential release, due to the vanishing energy barrier. Below this curve gives rise to reconfigurable 3D geometries.

Slight experimental variabilities, such as parasitic adhesion/stiction at regions adjacent to the bonding sites, can alter the energy landscape in ways that can be significant compared to the energy barrier for the unperturbed case. In such scenarios, even design parameters that suggest the existence of two modes can yield the same configuration for different release strategies. Statistical analysis of experiments on collections of three groups of 2D precursors (marked design points 1, 2 and 3 in Figure 3.2d) yield probabilities for realizing shape I during sequential release (Figure 3.2e). This probability (p) increases as the design point approaches the boundary between the two regimes in Figure 3.2d, consistent with a decrease in the magnitude of the energy barrier. The data can be fitted with an exponential law (Figure 3.2f), $p = exp\ (-E_{barrier} / E_{critical})$, where $E_{critical}$ = 52.6 nJ. Natural thermal fluctuations could affect the reconfiguration process in extremely small structures, as $E_{critical}$ scales by a factor of m^3 and can approach kT for room conditions, where k is the Boltzmann constant and T is the room temperature.

This understanding of the underlying mechanics principles enables a general design rationale for complex reconfigurable 3D mesostructures (Appendix Figure A2). Consider, as an example, classes of geometries that consist of straight ribbons with creases at the middle and end sections, as shown in Appendix Figure A3. Theoretical modelling serves as the basis for layout selection, where the focus is on the distribution of creases for a prescribed 2D shape, using an algorithm of exhaustive search for bistable designs (see Appendix A. 2 for details).

3.2.3 Representative Experimental Results

These design concepts allow the assembly of complex 3DFMs, some of which can transform between different recognizable geometries. Figure 3.3a illustrate three examples that reshape between a 'house' and a 'shopping bag', between a 'maple leaf' and a 'bird', or between an 'octopus' and a 'spider'.

In advanced versions of these design algorithms, tri-stable modes can be realized through complex release sequences. Figure 3.3b presents an example with three stable shapes, corresponding to three release sequences: simultaneous release (shape I), $[\varepsilon_{x\text{-}pre}, \varepsilon_{y\text{-}pre}] \rightarrow [\varepsilon_{x\text{-}pre}, 0] \rightarrow [0, 0]$ (shape II), and $[\varepsilon_{x\text{-}pre}, \varepsilon_{y\text{-}pre}] \rightarrow [0, \varepsilon_{y\text{-}pre}] \rightarrow [0, 0]$ (shape III). In principle, this same strategy can be extended to accommodate an even greater number (>3) of stable shapes by careful design and complex release sequences.

3.2.4 Morphable 3D RF Devices

Compatibility of these reconfigurable 3D structures with modern planar device technologies suggests potential for unusual classes of 3D microelectronic systems. Figure 3.4a–e presents a 3D radiofrequency (RF) circuit that can reconfigure reversibly between geometries that

function as a low-pass filter and an inductor. The simultaneous release of biaxial prestrain (60%) forms a resonant circuit that features an inductor (helical coils in Figure 3.4b) and a parallel-plate capacitor (shape I in Figure 3.4b). The sequential release yields a 3D shape that involves a large distance between the parallel plates (shape II in Figure 3.4b), resulting in an open circuit at this region. Here, the inductive-capacitive (LC) circuit functions only as a single inductor. Electromagnetic measurements summarized in Figure 3.4c show that the low-pass filter has a cutoff frequency at 1.9 GHz with passband ripple as high as 2.8 dB, possibly due to the mechanical instability of the soft testing fixture. In contrast, the inductor performs as a choke, providing different values of impedance to block signal at a desired frequency (Figure 3.4d). This reconfigurable function might have utility as a radio switch. Specifically, shape I turns the radio on across frequencies from 1.13 GHz to 1.36 GHz, as the return loss (S11) is less than -20 dB for this range, as shown in Figure 3.4c. Meanwhile, shape II turns the radio off by increasing the return loss beyond -1 dB for frequencies from 1.24 GHz to 3 GHz, as shown in Figure 3.4d. As such, the radio can be switched reversibly between on (shape I) and off (shape II) through mechanical tuning, for frequencies from 1.24 GHz to 1.36 GHz. The prestrain used in the 3D assembly can be used to tune the operating frequency (Figure 3.4e), for example, from radiolocation service (433.05 MHz to 434.79 MHz) at a prestrain level of 21–23%, to the 33-centimeter band amateur radio (902 MHz to 928 MHz) at a prestrain level of 39–43%.

A concealable electromagnetic device represents another application in reconfigurable 3D RF electronics (Figure 3.4f-k). The 2D precursor in this case consists of three parts, the first of which serves as an electromagnetically shielding structure; the second as three antennas for communication and a shielding structure; and the third as a support structure. The simultaneous release yields a working mode (shape I, Figure 3.4g), where the antennas are elevated and exposed.

The sequential release leads to a reconfigured system where the metallic support structure electromagnetically shields the coils. Figure 3.4h present measurements and modelling results for the return loss (S11) associated with these three antennas. Figure 3.4i show that the device can span a wide range of frequencies (from ~6 GHz to ~30 GHz). The radiant efficiencies obtained by simulation (Figure 3.4j) show that shape II has a much smaller radiant efficiency than shape I for all three antennas. Figure 3.4k illustrates the calculated radiant efficiency ratio of shape II to shape I as a function of prestrain. The ratio decreases slowly at the initial stage (prestrain $< 25\%$), and drops quickly for prestrain $>75\%$, as the shielding membranes in shape II begin to close. The compatibility of these approaches with planar microfabrication techniques suggests broad scalability and diversity in the choice of circuit designs.

3.3 Freestanding 3D Mesostructures

Recent work demonstrates that processes of stress release in prestrained elastomeric substrates can guide the assembly of sophisticated 3DFMs in advanced materials. A significant disadvantage of these systems is that the elastomeric substrates, while essential to the assembly process, can impose significant engineering constraints for applications such as micro robotics that demand the 3DFMs in freestanding forms. Here, we introduce concepts in interfacial photopolymerization and plastic mechanics to bypass these limitations[25]. The results enable 3DFMs in fully or partially freestanding forms via mechanisms quantitatively described by theoretical modeling. Taken together, these methodologies establish a set of enabling options in 3D micro/nanomanufacturing that lie outside of the scope of existing alternatives.

3.3.1 Interfacial Photopolymerizations

The first strategy to freestanding 3DFMs appear in Figure 3.6a. It starts with drop casting a liquid, photo-definable epoxy (SU8) onto the 3DFMs already assembled on the elastomer substrate that is deposited with a sacrificial layer of Al_2O_3 (~50 nm in thickness). Passing UV light through a photomask mounted on the back side of the substrate photopolymerizes a thin layer of the epoxy at the interface, with size and geometry matched to those of the 3DFMs. Developing the unexposed epoxy and removing the sacrificial layer in hydrochloric acid yield freestanding 3DFMs, whose 3D geometries are secured by the thin epoxy bases. Additional details appear in Section 3.6. Demonstrations of this strategy include a bilayer flower-like structure of SU8 (thickness: 7 µm, ribbon width: 50 µm) confined with hollow bases (thickness: 30 µm, inner radius: 300 µm, outer radius: 1 mm, Figure 3.6b), a peacock-like structure of silicon/SU8 (thickness: 200 nm/7 µm, ribbon width: 50 µm, Figure 3.6c) on a rectangular base (thickness: 30 µm, length: 1.3 mm, width: 1 mm), and a jellyfish-like structure of gold/SU8 (thickness: 50 nm/7 µm) on a circular base (thickness: 30 µm, radius: 1 mm, Figure 3.6d). In all cases, the 3DFMs are mechanically robust and can be suspended by other objects such as human hairs and needle tips as shown in Figure 3.6f-g. Bases with other geometries, such as thin rings (thickness: 50 µm, inner radius: 700 µm, outer radius: 1.1 mm), are also possible (Figure 3.6h). The yield of forming 3DFMs with this approach is ~90% (i.e., of ~50 samples, 5 failed). Fracture of the bases, typically near the bonding sites of the 3DFMs, represents the dominant failure mode. Increasing the thicknesses of the bases can reduce their probability for fracture, thereby improving the yield of this process.

In bases that adopt thin and/or narrow designs, mechanical restoring forces associated with the buckled 3DFMs can cause additional changes in shape upon release, as shown in Figure 3.6g. The average out-of-plane deformation of the base, in the form of a flatness factor (F), defines the

extent. Considering the square root dependence of the curvature on the compressive strain, the dimensionless form of this flatness factor (F/R, with R being the radius of the epoxy base) exhibits a simple scaling as determined by FEA. For the jellyfish-like and ring-like cases in Figure 3.6d and h, this scaling law captures the effect of bending stiffness for different parameter combinations, including cases of circular (Figure 3.6e) and hollow (Figure 3.6i) bases.

3.3.2 Plastic Mechanics

The second route to freestanding 3DFMs relies on controlled plasticity induced during assembly. As illustrated in Figure 3.6j, the 2D precursor designs in this scheme incorporate thin metal (copper) films, most importantly at locations that undergo strong bending due to the compressive buckling process. Plastic deformations in copper can hold the buckled 3DFMs in their 3D geometries even after release from the assembly substrate. Demonstrations in Figures 3.6k include 3DFMs made of copper (Left, thickness: 5 μm, crease width: 230 μm, ribbon width: 410 μm), copper/polyimide (Middle, thickness: 5 μm/7 μm, crease width: 130 μm, ribbon width: 320 μm), and copper/silicon (Right, thickness: 5 μm/1.5 μm, crease width: 250 μm, membrane width: 820 μm).

Spring-back effects associated with the elastic-plastic response, which depend on both the geometry and the prestrain level are important to consider. Quantitative mechanics analyses yield a simple scaling law for the spring-back ratio (ρ_s) that characterizes the copper/silicon composite design. For prestrains sufficiently large to induce plastic deformations, ρ_s decreases rapidly with increasing copper thickness (Figure 3.6l). Fracture at the creases is the major form of failure, arising from material defects introduced during the fabrication process that can induce nonuniform, localized plastic deformations, with success rates at around 70% (i.e., of ~20 samples, 6 failed).

Decreasing the thickness of the copper layer will reduce the strain concentrations at the crease regions, with the potential to reduce the failure rate. On the other hand, reducing the strain results in a decrease in plastic deformations at the creases, which also leads to more pronounced spring-back. Therefore, a balance between the two different considerations (failure rate and spring-back effect) should be considered.

3.4 3D Micro Swimmers

The studies in this chapter on shape transformations and freestanding 3DFMs suggest potentials in micro/nanoscale robots. A proof-of-concept described in the following exploits kirigami 3DFMs as self-propelled 3D micro swimmers with geometrically controlled dynamics and motion trajectories (Figure 3.7). The structures include strategically patterned films of platinum (Pt, 100 nm in thickness) to catalyze the production of water and oxygen (O_2) at room temperature upon immersion into hydrogen peroxide (H_2O_2, 30% by weight). Bubbles of O_2 drive movements of the 3D swimmers in a controlled manner that depends on the placement of the Pt films and the 3D geometries. With Pt on one side of the 3D swimmer depicted in Figure 3.7a, it executes linear motions. By contrast, with Pt on four petals and one side of the 3D swimmer as shown in Figure 3.7b, it realizes curvilinear motions. FEA simulations that model the forces induced by the O_2 bubbles as uniform pressures applied at the regions covered with Pt successfully capture the details, including the time-evolving gesture changes (Figure 3.7c-d). The predicted trajectories (Figure 3.7c-d) agree reasonably well with the experiments (Figure 3.7a-b), thereby establishing the models as predictive tools for design. These design possibilities extend the range of engineered motions that are possible in previous versions of related micro swimmers but built with comparatively simple designs.

3.5 Conclusions

In this chapter, we present strategies to realize morphable and freestanding 3DFMs. The results establish the basis for the 3DFMs towards micro/nano robotics applications. FEA simulations can capture quantitative mechanical details to facilitate the design process. Demonstrations include a variety of 3DFMs built using semiconductors, polymers, metals and their combinations, and 3D functional devices such as morphable RF devices and micro swimmers. Potential future directions include exploring other actuation mechanisms that can realize fast, reversible and dramatic 3D shape transformations, such as shape memory materials[26-27], skeletal muscles[28-29] and stimuli responsive materials (ionic polymers[30], magnetic composites[31] etc.). Furthermore, we can integrate wirelessly controlled and powered sensors[32-34] into the freestanding 3DFMs for remote and self-regulated motion controls.

3.6 Methods

Finite element analysis (FEA). Computational models of post-buckling analyses were developed using FEA software (ABAQUS) to simulate the processes of compressive buckling. 8-node solid elements (C3D8R) and 4-node shell elements (S4R) were used for the silicone substrate and 2D precursors, respectively. Convergence of mesh sizes was tested to ensure computational accuracy. Frictionless contact was implemented to model the interface between 2D precursors and substrate. The elastic modulus (E) and Poisson's ratio (v) are $E_{\mathrm{substrate}}$= 166 kPa and $\upsilon_{\mathrm{substrate}}$ =0.49 for substrate; E_{SU8}= 4.02 GPa and υ_{SU8} =0.22 for SU8; E_{PI}= 2.5 GPa and υ_{PI}=0.34 for PI; E_{Cu}= 119 GPa and υ_{Cu} =0.34 for copper (Cu). E_{Si}= 130 GPa and υ_{Si}=0.27 for silicon. E_{PET} = 2.7 GPa and υ_{PET} = 0.38 for PET.

Fabrications of 3DFMs in epoxy. Preparation began with formation of a sacrificial layer of thermally grown SiO_2 (600 nm, dry oxidation at 1150ºC) on a silicon wafer and uniform coating of an adhesion promoter (Omnicoat, MicroChem). The 2D precursors consisted of two layers of photodefinable epoxy (SU8 2 or SU8 5, MicroChem) sequentially patterned by spin coating and photolithography with precise alignment, in which the first and second layers of SU8 defined the matrix and the crease regions of the 2D precursors, respectively. A brief exposure to oxygen plasma removed the exposed adhesion promoter. Immersion in buffered oxide etchant (BOE, VWR International, 6:1) eliminated the exposed SiO_2 and created a thin partial undercut around the edges of the patterns of SU8. Next, photolithography defined a layer of photoresist (AZ 5214E, MicroChem, thickness ~ 1.6 µm) at all regions of the SU8 except those associated with the pads designed for bonding to the underlying elastomer platform. The photoresist also formed an anchor around the partially undercut edges of the patterns of SU8 to prevent them from lifting from the substrate during undercut by immersion in concentrated hydrofluoric acid (HF) for several hours to completely eliminate the underlying SiO_2. Then, a thin layer of silicon oxide (thickness ~ 50 nm) deposited on the sample surface by electron beam evaporation at the bonding pads created a surface chemistry necessary for strong adhesion to the platform. Transfer printing with a slab of polydimethylsiloxane (PDMS, Sylgard 184, 1:10) retrieved the 2D precursor from the silicon wafer and placed it on a piece of water-soluble tape (AQUASOL). A silicone elastomer substrate (Dragon Skin® 10) was stretched to a desired prestrain using a customized stage. After exposing the elastomer and the 2D precursors (on the water-soluble tape) to ultraviolet (UV) induced ozone (Jelight UVO-Cleaner, Model 144AX) to create surfaces with hydroxyl termination on the silicone and the SiO2 on the bonding pads, the two were laminated together and then baked in a convection oven at 70 °C to yield strong adhesion via condensation reactions at the interface. Finally,

dissolving the tape in warm water, removing the photoresist by immersion in an acetone bath, and slowly releasing the prestrain along prescribed release paths completed the assembly process.

Fabrications of 3DFMs in silicon. Preparation began with patterning the device layer of a silicon-on-insulator (SOI) wafer (top silicon thickness ~ 1.5 μm, SOITEC) using standard methods in photolithography and reactive ion etching (RIE). Partial undercut with BOE, photoresist patterning and full undercut with HF, as well as transfer printing, UV ozone exposure, bonding, dissolution of the water-soluble tape, removal of the photoresist and release of the prestrain all followed procedures similar to those for the SU8 samples described above.

Fabrications of 3D n-MOSFET transistors. Preparation began with thermal growth of SiO_2 (200 nm) on a p-type SOI wafer (top Si thickness ~200 nm, SOITEC). Patterning the SiO_2 by photolithography and etching in BOE defined openings for solid-state diffusion doping with phosphorus (1000 ^oC for 7 min) to define the source and drain contacts. Immersion in concentrated HF for 30 min completely removed the buried oxide layer of the SOI, allowing retrieval of the device silicon layer onto the surface of a PDMS stamp for transfer printing onto a spin-cast bilayer of poly(methylmethacrylate) (PMMA, MicroChem, thickness ~200 nm) and polyimide (PI, HD MicroSystems, thickness ~2 μm) on a Si wafer. Photolithography and RIE etching isolated the device silicon into regions for individual transistors. A layer of SiO_2 (thickness ~ 400 nm) deposited by plasma-enhanced chemical vapor deposition at 200 ^oC served as the gate dielectric. Photolithography and BOE etching formed openings through the SiO_2 to expose the source and drain contact regions. Deposition of Cr (thickness ~ 5 nm) and Au (thickness ~ 150 nm) by electron beam evaporation followed by photolithography and wet etching defined the gate electrodes and

metal interconnects. Spin coating another layer of PI (thickness ~ 2 µm) and oxygen plasma etching through a thick photoresist mask (AZ 4620, MicroChem, thickness ~ 10 µm) completed the top encapsulation. After removing the photoresist (AZ 400T stripper, AZ Electronic Materials), the underlying PMMA layer was then dissolved by immersion in acetone overnight to allow retrieval onto a piece of water-soluble tape. A thin layer of SiO_2 (thickness ~ 50 nm) was deposited selectively onto the bonding sites through a shadow mask. The 3D assembly process then followed the same procedures for the SU8 and silicon samples as described above.

Fabrications of 3D frameworks that incorporate µ-LEDs. Preparation began by spin coating and curing PI (thickness ~5 µm) on a 3-µm-thick copper foil, followed by lamination of the film with the copper layer facing up onto a PDMS-coated glass slide. Photolithography and wet etching patterned the copper layer into designed geometries. Transfer printing using a mask aligner (Karl Suss MJB3) delivered the µ-LEDs (Cree TR2227 LEDs) onto the copper electrodes with a small amount (1–2 beads per electrode) of In/Ag solder paste (Indalloy 290, Indium Corporation). Placing the device on a hot plate at 150 °C for 1 min electrically bonded the µ-LEDs to the electrodes. A photolithographically defined layer of SU8 (thickness ~4 µm) encapsulated the entire systems, leaving only the external electrodes exposed for connections to an external power supply. A thick layer of photoresist (AZ4620, MicroChem, thickness ~10 µm) was then patterned to mask the device during removal of the exposed PI by exposure to oxygen plasma. The remaining processes of device retrieval by a piece of water-soluble tape, selective SiO2 deposition and 3D assembly then followed the same steps as for the 3D n-MOSFET described above.

Fabrications of 3D RF electronic structures. Preparation of the 3D device in Figure 3.4a-e began with spin casting and curing a layer of PI (thickness ~ 2 μm) on a copper foil (thickness 3 μm, Olin Brass), followed by lamination onto a PDMS-coated glass slide, with copper side facing up. The 3D RF circuit consisted of two different 2D precursors fabricated separately and then joined together prior to 3D assembly. Patterning of each 2D precursor involved two sequential lithographic processes: 1), patterning the copper by photolithography and wet etching; 2), patterning the PI by photolithography and oxygen plasma etching through a thick photoresist mask (AZ 4620, MicroChem, thickness ~ 10 μm). Removing the photoresist (AZ 400T stripper, AZ Electronic Materials) allowed retrieval onto a piece of water-soluble tape. Retrieval of the second layer onto the same piece of tape occurred in an aligned manner under an optical microscope. A thin layer of SiO_2 (thickness ~ 50 nm) was deposited selectively onto the bonding sites through a shadow mask. The 3D assembly process then followed the same procedures for the SU8 and silicon samples as described above.

Preparation of the 3D concealable electromagnetic device (Figure 3.4f-k) began by laminating a commercially available polyimide film on copper foil (Pyralux AC091200EV, DuPont) onto a PDMS-coated glass slide, with copper facing up. Laser cutting defined the overall geometries. Standard photolithography and wet etching patterned the copper. Spin coating a thin layer of PI (thickess ~ 1.5 um) followed by deposition of Cr (thickness ~ 5 nm) and Au (thickness ~ 100 nm) defined the electromagnetic shielding layer on the four legs. The metals and PI were patterned by wet and oxygen plasma etching using layers of photoresist as masks, respectively. Removing the photoresist (AZ 400T stripper, AZ Electronic Materials) allowed the samples to be retrieved onto a piece of water-soluble tape. A thin layer of SiO_2 (thickness ~ 50 nm) was deposited

selectively onto the bonding sites through a shadow mask. The 3D assembly process then followed the procedures described above.

Electromagnetic measurements. Two port S-parameters were measured using the Agilent PNA8363C purpose network analyzer with Cascade Microtech air coplanar ground-signal-ground probes in the frequency range from 10 MHz to 40 GHz. Measurements of the 3D RF circuit used a test fixture shown in Figure 3.5. A thin glass slide placed underneath the contact pads allowed leveling of the probes on the soft substrate. Parasitic effects introduced by feedlines were removed using an open-through de-embedding technique to obtain the real performance of the device under test (DUT). A lumped equivalent circuit model captured the physics of the parasitic effects. Open-through de-embedding patterns are in Figure 3.5. As in Figure 3.5, an admittance Π-network modeled the capacitive effects between the contact pads and the surrounding environment including the substrate and RF ground. An impedance network connected in series modeled the resistance and inductance of the feedlines. Figure 3.5a-c shows schematic views of patterns with the DUT, without the DUT (open case) and with connection thru directly. Corresponding lumped equivalent circuits captured the RF performance of each pattern. The narrow branches of the feedlines were bent 90° to avoid using additional lines to connect the two feedlines.

Electromagnetic simulations. The finite element method was adopted in electromagnetic simulations to calculate the S parameters, central frequency and bandwidth of reconfigurable RF circuit, as well as the return loss parameter (S11) and the radiation efficiency of the antennas. The simulations used the commercial software ANSYS HFSS, in which tetrahedron elements were used in the solution with adaptive meshing convergence. The different 3D configurations of the

devices enabled by the loading-path strategy were all exported from the mechanics simulation performed using the software ABAQUS, and then imported to the software ANSYS HFSS. All the metal layers in the devices, including the antennas themselves, metallic supporting structures and the metal plane underneath the substrate, are modeled by Finite Conductivity Boundary for the sake of efficiency, with use of the prescribed thicknesses. The relative permittivity (ε_r), relative permeability (μ_r) and conductivity (σ) are $\varepsilon_{r_Cu} = 1$, $\mu_{r_Cu} = 0.999991$ and $\sigma_{Cu} = 5.8 \times 10^7 \mathrm{S/m}$; $\varepsilon_{r_PI} = 3.5$, $\mu_{r_PI} = 1$ and $\sigma_{PI} = 0 \mathrm{S/m}$; and $\varepsilon_{r_substrate} = 2.55$, $\mu_{r_substrate} = 1$ and $\sigma_{substrate} = 2.5 \times 10^{-14} \mathrm{S/m}$.

Fabrications of freestanding 3DFMs with epoxy bases. The process began with the fabrications and assembly of 3DFMs with Al_2O_3 (50 nm in thickness) sacrificial layers deposited between the bonding sites and the elastomer substrates, in a similar manner described in previous sections. Drop casting photo-definable epoxy (SU8) with pipettes onto the 3DFMs, followed by baking at 65 °C for 10 min and at 95 °C for 19 h created a solid encapsulation around the 3D geometry. Passing UV light through a photomask mounted on the back side of the substrates, followed by baking at 65 °C for 2 min and 95 °C for 2 min and immersion in SU8 developer, yielded a thin polymer base. The photomask defined the lateral geometries of this base; the UV exposure dose defined its thickness. Immersing the samples in hydrochloric acid (37% by weight) for 19 h dissolved the Al_2O_3 sacrificial layers to release the 3DFMs from the elastomer substrates.

Fabrications of freestanding 3DFMs using plastic mechanics. Preparation of freestanding 3D copper structures began with spin coating a thin layer of PI (400 nm in thickness) onto the front side of a copper film (5 μm in thickness). The film was then laminated onto a PDMS-coated (10

μm in thickness) glass substrate, with PI side in contact with the PDMS. Photolithography, wet etching, and reactive ion etching (RIE) patterned the copper and PI layers in a matching geometry. Retrieving the structure onto water-soluble tape allowed deposition of Ti/SiO_2 (5 nm/50 nm in thickness) via electron beam evaporation through a shadow mask to define the bonding sites. The remaining steps followed the procedures described in previous sections.

Preparation of freestanding 3D copper/PI structures involved spin coating a thick layer of PI (7 μm in thickness) on the back side of a copper film to yield copper–polymer bilayers and then following the procedures described above, with extra photolithography and RIE steps to pattern the thick PI layer to cover the non-crease regions of copper.

Preparation of freestanding 3D copper/silicon structures began with transfer printing 2D silicon patterns (1.5 μm in thickness) onto a partially cured layer of PI (adhesive layer, 1.5 μm in thickness, baked at 110 °C for 1 min) spin casted on the back side of copper film. The subsequent procedures followed those described above, with the additional steps of fully curing the PI adhesive layer, and photolithography and RIE to define silicon structures to match the non-crease regions of the copper patterns.

Fabrications of 3D micro swimmers. Preparation of 3D micro swimmers started with thermal oxidation to form a layer of SiO_2 (800 nm in thickness) on a silicon wafer. Spin coating, photolithography, electron beam evaporation, and lift-off then formed strategically designed patterns of Ti/Pt/Cr (5 nm/50 nm/5 nm in thickness) as the catalysts. Next, spin coating and photolithography defined patterns of SU8 (7 μm in thickness). The remaining steps followed the procedures for fabrications of freestanding 3DFMs with polymer bases described above.

3.7 Figures

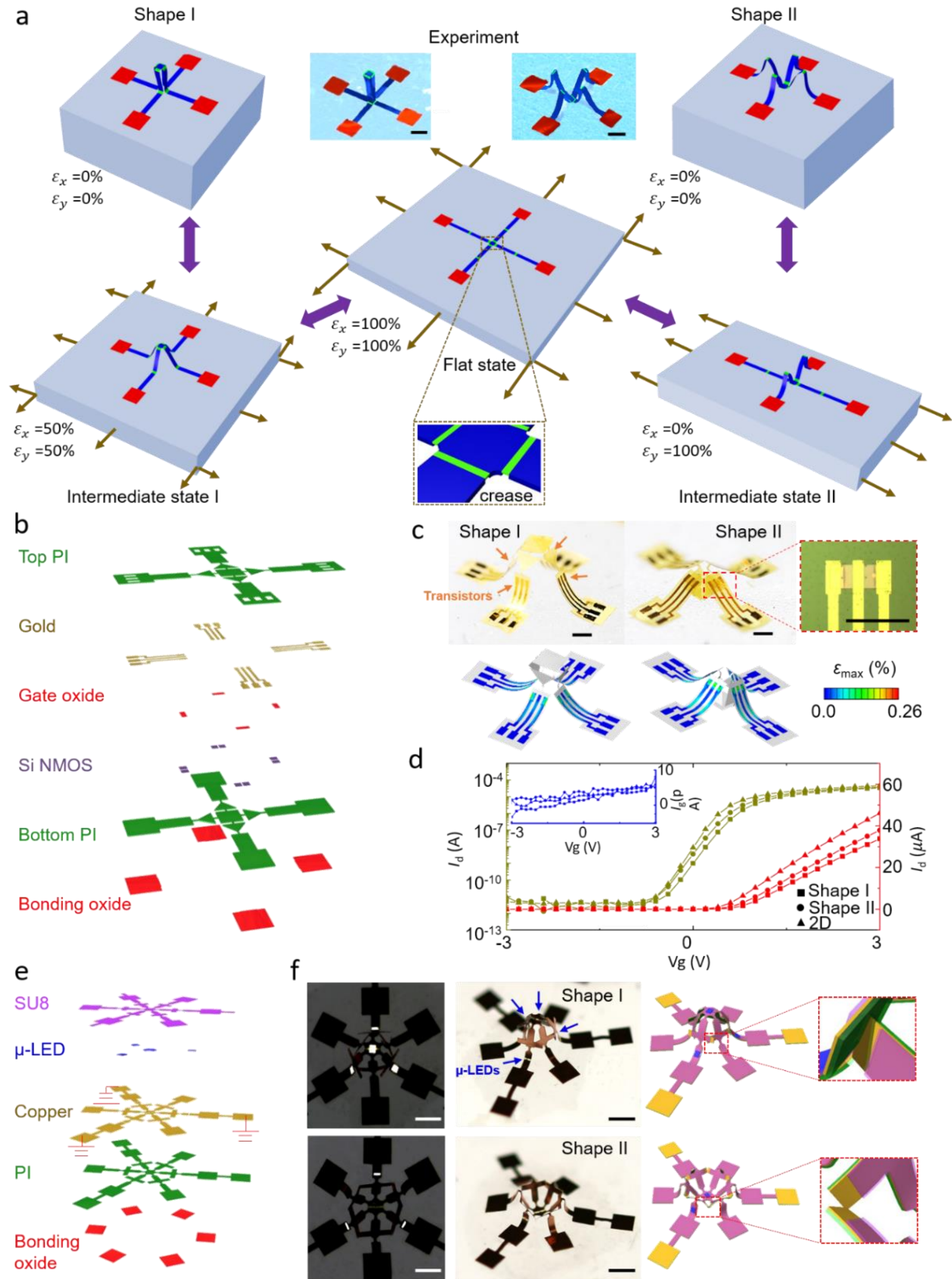

Figure 3.1 Reconfigurable 3DFMs by loading-path controlled mechanical assembly. (a) Conceptual illustration of the strategy through a sequence of FEA results and a pair of colorized

Figure 3.1 (cont.) SEM images of two 3DFMs. Scale bars = 200 μm. (b) Exploded view of the 2D precursor of the 3D shape-shifting n-MOSFET transistor array. (c) Optical images of two configurations of the device after 3D assembly. Shape I and shape II correspond to simultaneous and sequential release, respectively. The color in the FEA results of d corresponds to the magnitude of maximum principal strain in the metal. Scale bars = 200 μm. (d) Current-voltage (I-V) characteristics of a transistor measured with the structure in Mode I, Mode II and the planar state. (e) Exploded view of the 2D precursor of the 3D shape-shifting LED circuits. (f) Top and side views of the 3D LED circuits in shape I (central LED ON) and shape II (central LED OFF), and the FEA results indicating the circuit switch between the two shapes. Scale bars = 1 mm. Reproduced from reference 1.

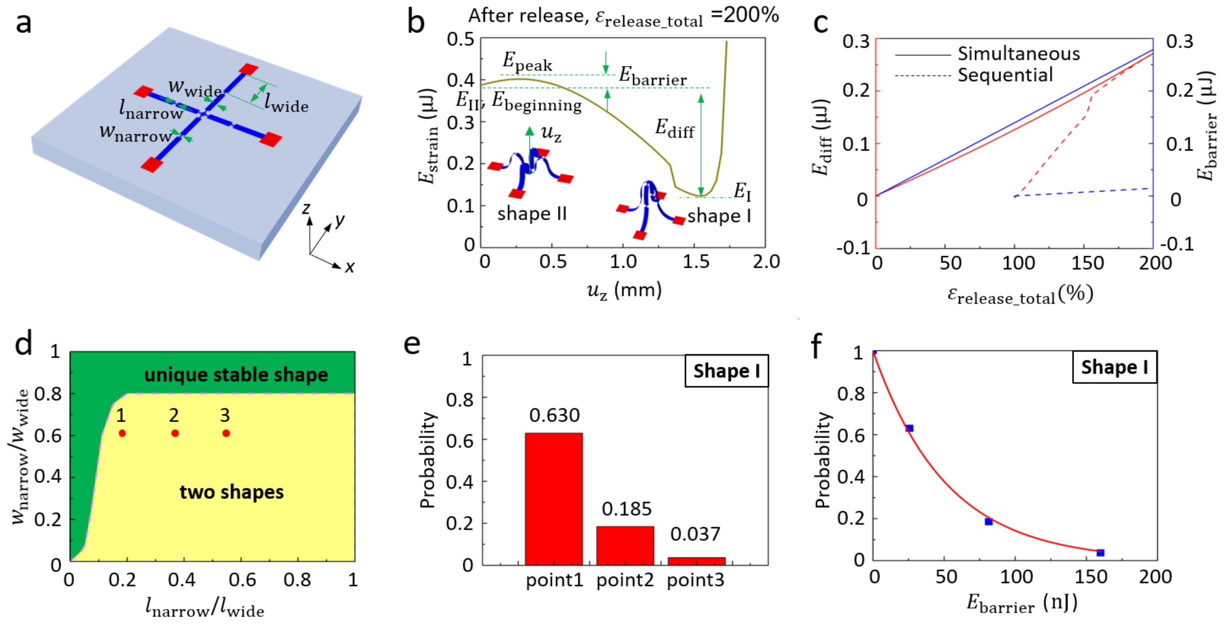

Figure 3.2 Mechanics and general design approach. (a) FEA illustration of the 2D precursor used in this study. (b) Computed strain energy as a function of central displacement, revealing two distinct modes that are both local energy minima. (c) Computed energy difference as a function of the total release strain for the simultaneous and sequential releases, respectively. (d) Phase diagram of one of two shapes governed by width and length of the creases shown in (a). (e) Experimentally collected probability of assembling into shape I with three different crease geometries shown as points 1-3 in (d). (f) Fitted probability of shape I as a function of the energy barrier. Reproduced from reference 1.

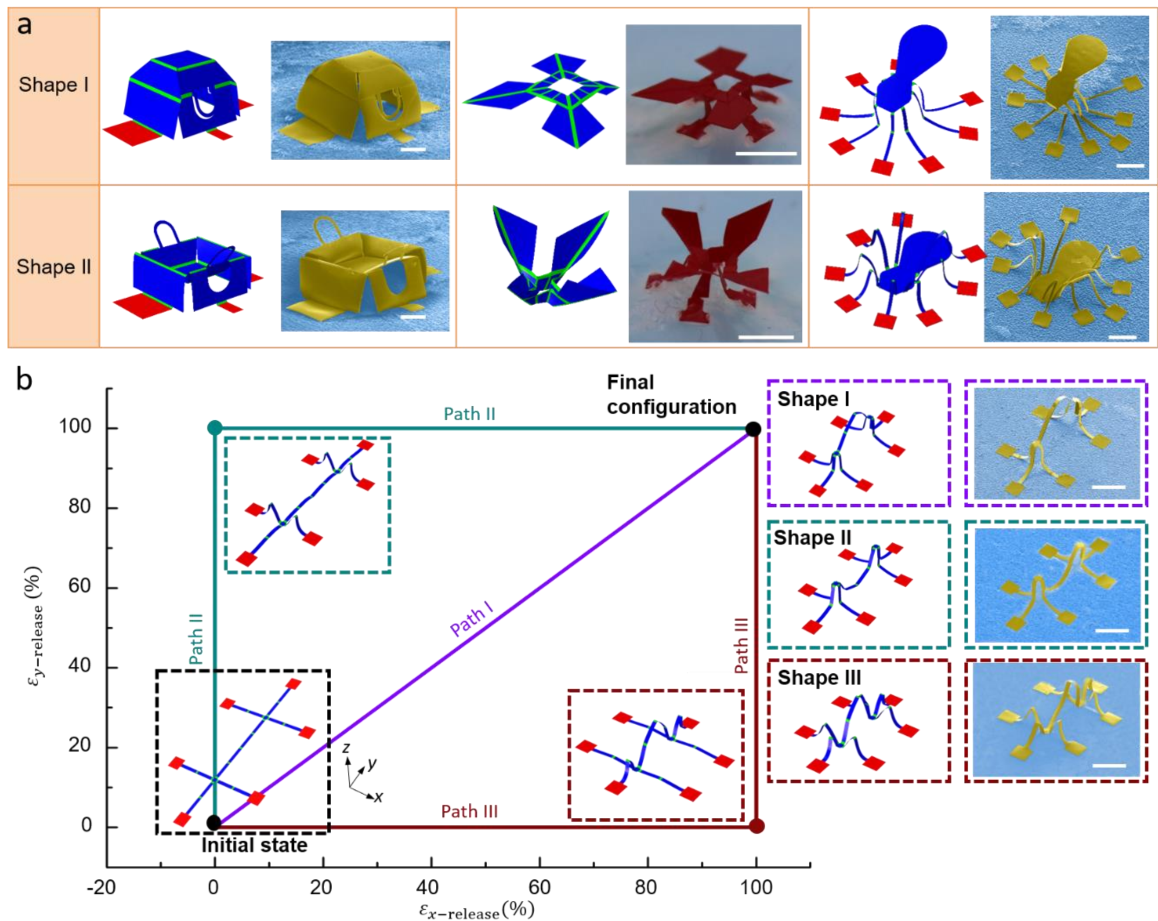

Figure 3.3 Experimental results of reconfigurable 3DFMs. (a) 3DFMs that transform between recognizable geometries. (b) Example of a 3DFM capable of transforming between three distinct geometries(right) and their corresponding release paths (left). Scale bars = 500 µm. Reproduced from reference 1.

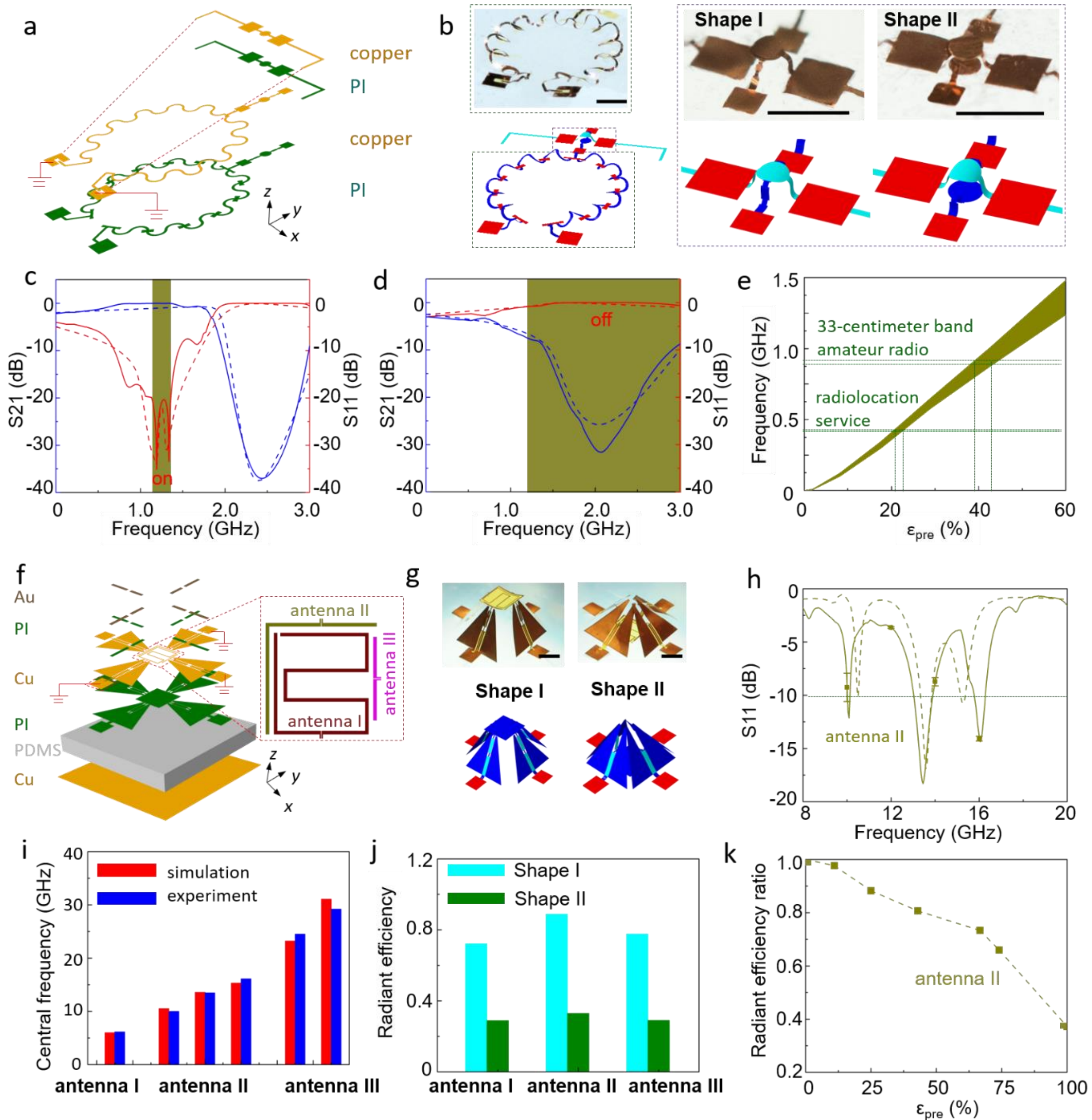

Figure 3.4 Applications of reconfigurable 3DFMs as switchable radio frequency (RF) electronic components. (a) Exploded view of the layer construction of the switchable RF device. [thickness of each layer from top to bottom: Cu (3 μm), PI (2 μm), Cu (3 μm), PI (2 μm)] (b) FEA predictions and optical images of the overall device, and magnified view of the capacitor structure that results from different release sequences. Scale bars, 1 mm. (c) S21 and S11 versus frequency for shape I when the device is released from a biaxial prestrain ($\varepsilon_{x\text{-}pre} = \varepsilon_{y\text{-}pre} = 60\%$). (d) S21 and

Figure 3.4 (cont.) S11 versus frequency for shape II when the device is released from a biaxial prestrain ($\varepsilon_{x\text{-}pre} = \varepsilon_{y\text{-}pre} = 60\%$). (e) Switchable frequency band as a function of the level of release strain when the device is subject to different biaxial prestrains. (f) Exploded view of the layer construction of the electromagnetic device with shielding capability [thickness of each layer from top to bottom: Au (100 nm), PI (1.5 μm), Cu (9 μm), PI (12 μm), silicone (5 mm), Cu (100 nm)]. (g) FEA prediction (lower frames) and optical images (upper frames) for the device. Scale bars, 5 mm. (h) Measured and computed dependence of the return loss (S11) on the frequency for antenna II. (i) FEA predictions and experimental measurements of the central frequency for antenna I, II and III. (j) Radiant efficiency for antenna I (at frequency f=6.0 GHz), II (f=13.58 GHz) and III (f=23.2 GHz) when the device is released from a biaxial prestrain ($\varepsilon_{x\text{-}pre} = \varepsilon_{y\text{-}pre} = 85\%$). (k) Radiant efficiency ratio for antenna I (f=6.0 GHz) as a function of the prestrain. In (c), (d) and (h), the solid and dash lines correspond to experimental and FEA results, respectively. Reproduced from reference 1.

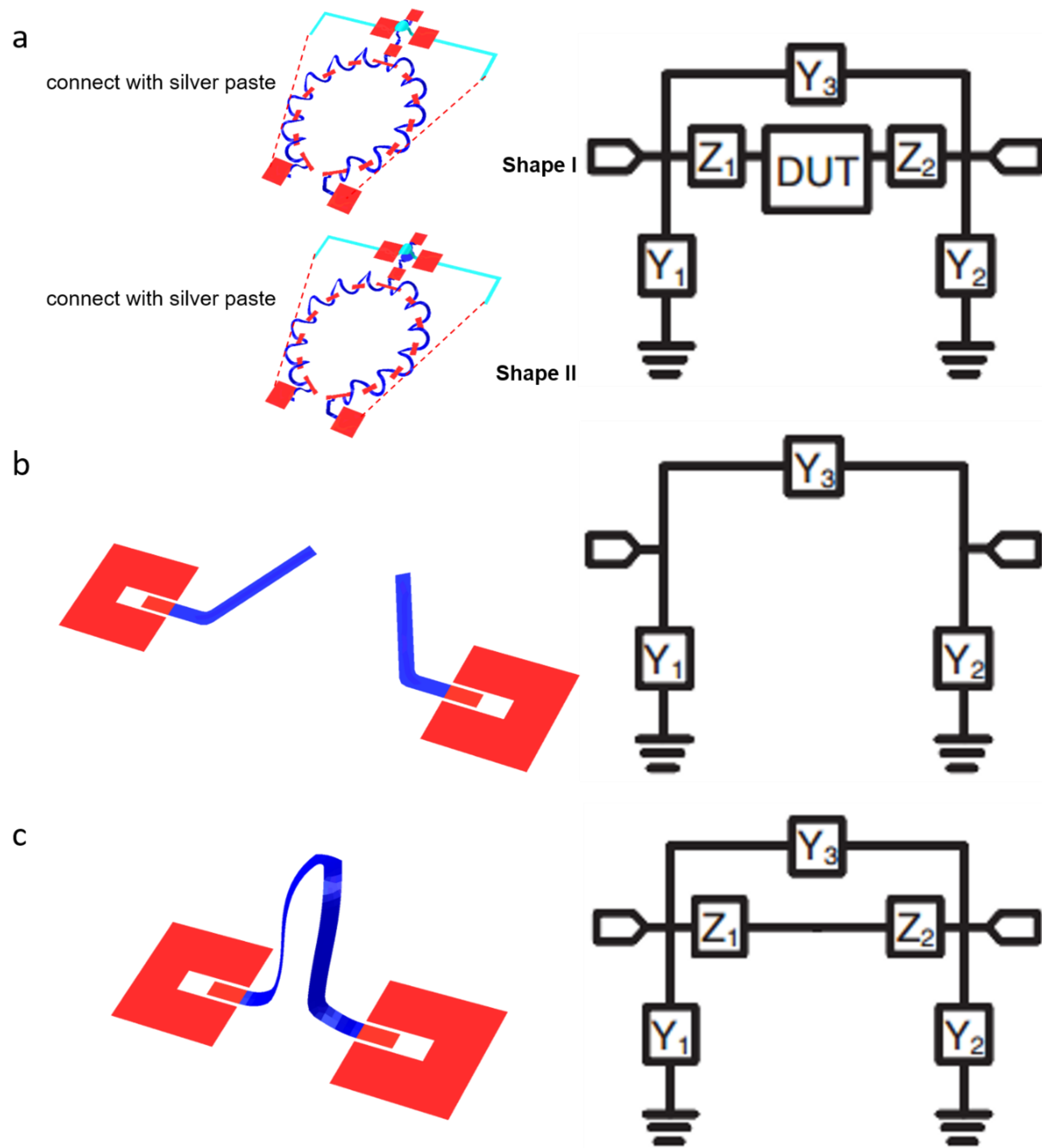

Figure 3.5 Open-through de-embedding patterns and their corresponding lumped equivalent circuits. (a) Test pattern with DUT. (b) Open pattern. (c) Thru pattern. Reproduced from reference 1.

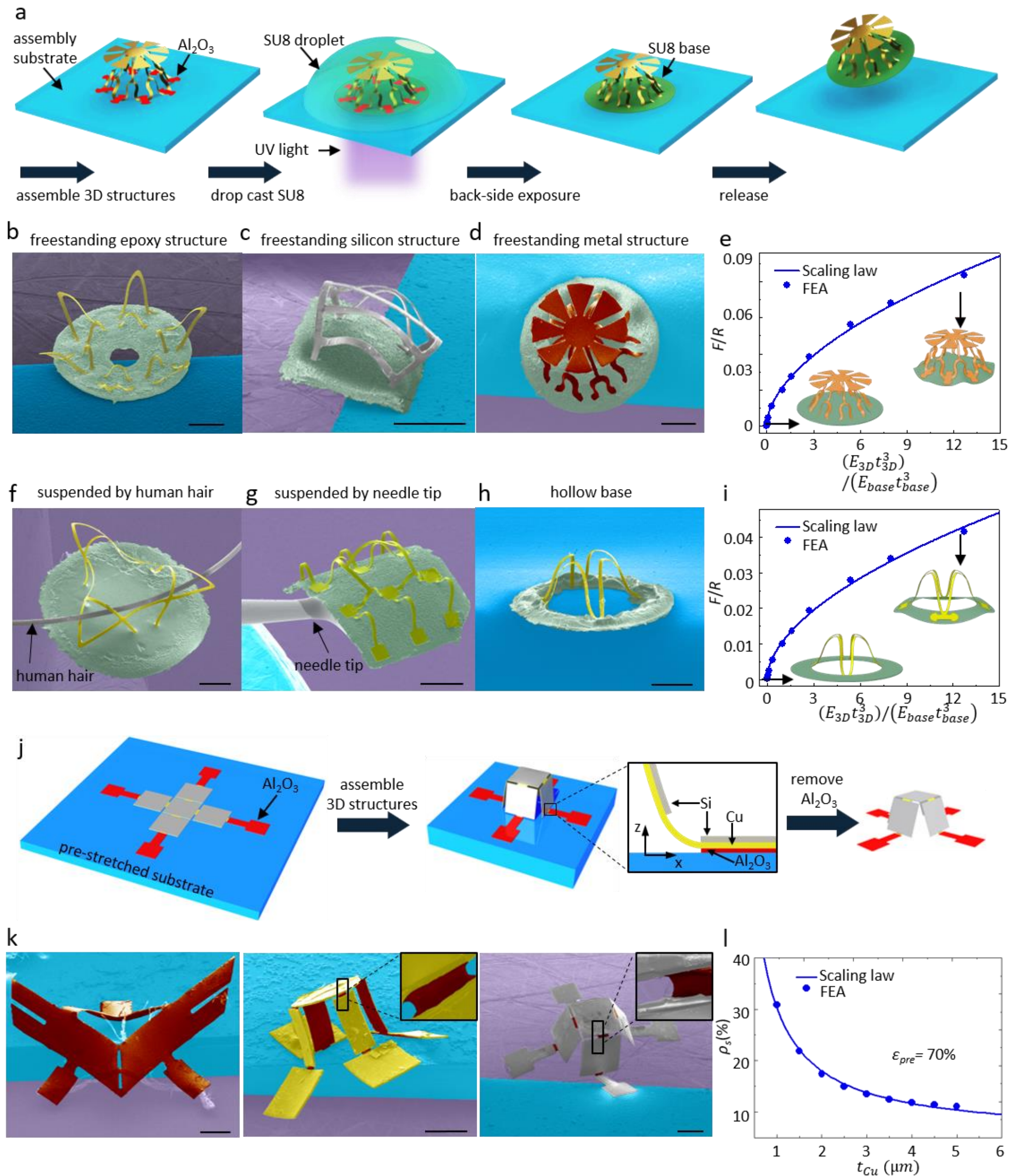

Figure 3.6 Freestanding 3DFMs. (a) Schematic illustration of a method for forming freestanding 3DFMs using photo-defined epoxy bases. (b)-(d) SEM images of freestanding 3DFMs made of SU8 (b), silicon/SU8 bilayers (c), and gold/SU8 bilayers (d). (e) Analytical modeling and FEA results of the flatness ratio (F) versus the ratio of bending stiffness for the jellyfish-like structure on a circular base. (f)-(g) SEM images of freestanding 3DFMs suspended by human hairs (f) and

Figure 3.6 (cont.) needle tips (g). (h) SEM image of a pillar-like structure confined with a narrow, ring-like hollow base. (i) Analytical and FEA results of flatness ratio (F) versus the ratio of bending stiffness for a ribbon structure on a hollow base. (j) Schematic illustration of another route to freestanding 3DFMs using plastic mechanics. (k) SEM images of freestanding 3DFMs made of copper (left), copper/PI bilayers (middle), and copper/silicon bilayers (right). (l) Analytical and FEA results of spring-back ratio (ρ_s) as a function of copper thickness for the box structure. Scale bars = 500 μm. Reproduced from reference 25.

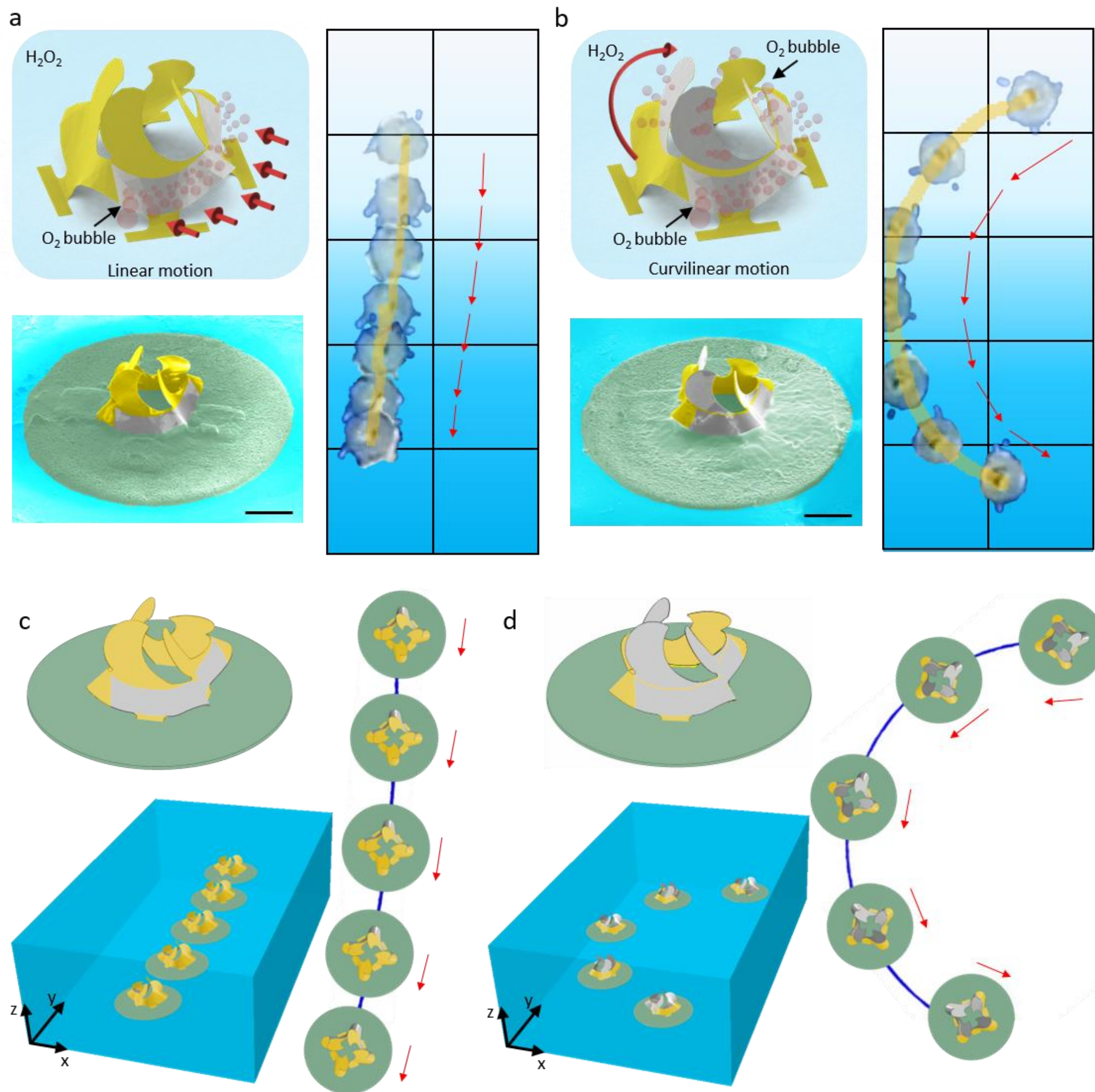

Figure 3.7 3D micro swimmers with controlled motion trajectories. (a)-(b) Schematic illustrations, SEM images, and superimposed images of micro swimmers designed for linear motion (a) and curvilinear motion (b). Scale bars = 500 µm. (c)-(d) 3D and top views of the trajectories and configurations of micro swimmers predicted by FEA modeling. Reproduced from reference 25.

3.8 References

1. Fu, Haoran, et al. "Morphable 3D mesostructures and microelectronic devices by multistable buckling mechanics." Nature materials 17.3 (2018): 268.

2. Yan, Zheng, et al. "Three-dimensional mesostructures as high-temperature growth templates, electronic cellular scaffolds, and self-propelled microrobots." Proceedings of the National Academy of Sciences 114.45 (2017): E9455-E9464.

3. Miura, Koryo. "Method of packaging and deployment of large membranes in space." title The Institute of Space and Astronautical Science report 618 (1985): 1.

4. Randall, Christina L., Evin Gultepe, and David H. Gracias. "Self-folding devices and materials for biomedical applications." Trends in biotechnology 30.3 (2012): 138-146.

5. Bishop, David, et al. "Silicon micro-machines for fun and profit." Journal of Low Temperature Physics 169.5-6 (2012): 386-399.

6. Kwok, Sen W., et al. "Magnetic assembly of soft robots with hard components." Advanced Functional Materials 24.15 (2014): 2180-2187.

7. Silverberg, Jesse L., et al. "Using origami design principles to fold reprogrammable mechanical metamaterials." science 345.6197 (2014): 647-650.

8. Silverberg, Jesse L., et al. "Origami structures with a critical transition to bistability arising from hidden degrees of freedom." Nature materials 14.4 (2015): 389.

9. Yang, Nan, and Jesse L. Silverberg. "Decoupling local mechanics from large-scale structure in modular metamaterials." Proceedings of the National Academy of Sciences 114.14 (2017): 3590-3595.

10. Overvelde, Johannes TB, et al. "A three-dimensional actuated origami-inspired transformable metamaterial with multiple degrees of freedom." Nature communications 7 (2016): 10929.

11. Overvelde, Johannes TB, et al. "Rational design of reconfigurable prismatic architected materials." Nature 541.7637 (2017): 347.

12. Rogers, John, et al. "Origami mems and nems." Mrs Bulletin 41.2 (2016): 123-129.

13. Leong, Timothy G., et al. "Tetherless thermobiochemically actuated microgrippers." Proceedings of the National Academy of Sciences 106.3 (2009): 703-708.

14. Ding, Zhen, et al. "Direct 4D printing via active composite materials." Science advances 3.4 (2017): e1602890.

15. Gladman, A. Sydney, et al. "Biomimetic 4D printing." Nature materials 15.4 (2016): 413.

16. Kim, Jungwook, et al. "Designing responsive buckled surfaces by halftone gel lithography." Science 335.6073 (2012): 1201-1205.

17. Xu, S., Yan, Z., Jang, K.I., et al. "Assembly of micro/nanomaterials into complex, three-dimensional architectures by compressive buckling." Science 347.6218 (2015): 154-159.

18. Zhang, Yihui, et al. "A mechanically driven form of Kirigami as a route to 3D mesostructures in micro/nanomembranes." Proceedings of the National Academy of Sciences 112.38 (2015): 11757-11764.

19. Yan, Zheng, et al. "Controlled mechanical buckling for origami-inspired construction of 3D microstructures in advanced materials." Advanced functional materials 26.16 (2016): 2629-2639.

20. Yan, Zheng, et al. "Mechanical assembly of complex, 3D mesostructures from releasable multilayers of advanced materials." Science advances 2.9 (2016): e1601014.

21. Nan, Kewang, et al. "Engineered elastomer substrates for guided assembly of complex 3D mesostructures by spatially nonuniform compressive buckling." Advanced functional materials 27.1 (2017).

22. Fu, Haoran, et al. "Mechanically-Guided Deterministic Assembly of 3D Mesostructures Assisted by Residual Stresses." small 13.24 (2017).

23. Kim, Jeonghyun, et al. "Battery-free, stretchable optoelectronic systems for wireless optical characterization of the skin." Science advances 2.8 (2016): e1600418.

24. Fenno, Lief, Ofer Yizhar, and Karl Deisseroth. "The development and application of optogenetics." Annual review of neuroscience 34 (2011).

25. Yan, Zheng, et al. "Three-dimensional mesostructures as high-temperature growth templates, electronic cellular scaffolds, and self-propelled microrobots." Proceedings of the National Academy of Sciences 114.45 (2017): E9455-E9464.

26. Otsuka, Kazuhiro, and Clarence Marvin Wayman, eds. Shape memory materials. Cambridge university press, 1999.

27. Huang, W. "On the selection of shape memory alloys for actuators." Materials & design 23.1 (2002): 11-19.

28. Cvetkovic, Caroline, et al. "Three-dimensionally printed biological machines powered by skeletal muscle." Proceedings of the National Academy of Sciences 111.28 (2014): 10125-10130.

29. Raman, Ritu, et al. "Optogenetic skeletal muscle-powered adaptive biological machines." Proceedings of the National Academy of Sciences 113.13 (2016): 3497-3502.

30. Yeom, Sung-Weon, and Il-Kwon Oh. "A biomimetic jellyfish robot based on ionic polymer metal composite actuators." Smart materials and structures 18.8 (2009): 085002.

31. Ma, Mingming, et al. "Bio-inspired polymer composite actuator and generator driven by water gradients." Science 339.6116 (2013): 186-189.

32. Kim, Tae-il, et al. "Injectable, cellular-scale optoelectronics with applications for wireless optogenetics." Science 340.6129 (2013): 211-216.

33. Kim, Jeonghyun, et al. "Miniaturized Battery - Free Wireless Systems for Wearable Pulse Oximetry." Advanced functional materials 27.1 (2017).

34. Han, Seungyong, et al. "Battery-free, wireless sensors for full-body pressure and temperature mapping." Science translational medicine 10.435 (2018): eaan4950.

CHAPTER 4

UNCONVENTIONAL APPLICATIONS

Significant portions of this chapter were published as: "Three-Dimensional Mesostructures as High-Temperature Growth Templates, Electronic Cellular Scaffolds, and Self-Propelled Microrobots." by Zheng Yan, Mengdi Han, *et al.*, *Proceedings of the National Academy of Sciences*, 114.45 (2017); "Compliant and Stretchable Thermoelectric Coils for Energy Harvesting in Miniature Flexible Devices." by Kewang Nan, Stephen Dongmin Kang, Kan Li *et al.*, *Science Advances*, 4.11 (2018); and "Soft 3D Microscale Vibratory Platforms for Characterization of Nano-Thin Polymer Films." by Kewang Nan, Heling Wang, Xin Ning *et al.*, *ACS Nano*, (2018). Reproduced with permission from the journals.

4.1 Introduction

The studies on the mechanics and fabrications of the mechanically-guided 3DFMs in previous chapters pave ways to unconventional device applications that are otherwise difficult to realize through conventional 3D assembly techniques. In this chapter, we present examples of these applications in bio-integrated electronics[1], energy harvesting[2], and nanomechanical sensing[3]. The results are expected to stimulate the inventions of high-performance, novel devices in many engineering fields.

4.2 3D Bio-integrated Electronic Scaffolds

Transferred 3D frameworks[1] can be used for guided growth of biological systems. Sophisticated cellular scaffolds can leverage high-performance components, including various electronic and optoelectronic devices, formed in 2D planar designs, to allow interaction and

communication with live cells and tissues in 3D. Potential consequences range from in vitro drug development to in vivo tissue repair[4-6].

4.2.1 High-resolution, in situ Imaging of Biological Tissues

As a demonstration, 3D bilayer nested cages of epoxy (Figure 4.1a) transferred onto optical-quality glass to enable high-resolution, in situ imaging, serve as growth platforms for neural networks of dorsal root ganglion (DRG) cells dissociated from explants from rats. The DRG, located on the dorsal root of the spinal nerve, contains the cell bodies of pseudounipolar sensory neurons, along with other types of cells, including satellite glial cells and Schwann cells. From the DRG, sensory neurons project axons that bifurcate, connecting to the central nervous system (CNS) on one end and the periphery of the organism on the other (Figure 4.1a, left). The DRG is an interesting research target due to its relevance in peripheral nerve repair and to its connection to the nonregenerative CNS[7-8]. Presented here, the 3D bilayer cage structure is pretreated to promote cell adhesion with a modified form of poly-D-lysine (PDL) which includes peptides containing the integrin-binding sequence of amino acids, arginine–glycine–aspartic acid (RGD) (Figure 4.1a, right)[9]. During the 35 d of cell culture development, the DRG cells organize into networks that exhibit two main modes of interaction with the scaffolds: following the 3D geometries of the scaffolds (left two frames in Figure 4.1b) and forming “shortcuts” between ribbons (right two frames in Figure 4.1b). The DRG cells are fixed and immunostained based on neuron-specific (MAP2, red) and glia-specific (GFAP, green) markers to show the organization of cells on the scaffolds by using confocal fluorescence microscopy. Corresponding phase-contrast images are also included in Figure 4.1b to delineate the scaffold geometries. These experiments

demonstrate that the scaffolds facilitate the reorganization of initially uniform dispersions of cells into hierarchical cellular constructs dictated in part by intrinsic cell properties.

Gradient light interference microscopy[10] (GLIM, Figure 4.1c) can capture the full 3D nature of both the scaffolds and the tissue constructs formed within them, along with intrinsic cell properties. This method offers label-free imaging by use of the gradient of the phase rather than the phase itself. In situ GLIM time-lapse characterization, summarized in Figure 4.1d, highlights the formation of the aforementioned shortcuts over the course of 27 h. Figure 4.1e provides a 3D image rendered from the GLIM data of a single DRG cell bridging cellular structures on two different ribbons, providing information regarding the thickness of the cellular structures.

4.2.2 Monitoring Electrophysiological Behaviors of Biological Tissues

Integration of microelectrodes into such 3D constructs allows study of the electrophysiological behaviors of the growing DRG neural networks (Figure 4.2). Here, exposed circular gold pads (50 μm in diameter, 300 nm in thickness) patterned on 3D cages act as microelectrodes for noninvasive extracellular stimulation and recording of action potentials (Figure 4.2a). A nanostructured, biocompatible layer of titanium nitride (TiN, 50 nm in thickness) deposited onto these gold pads increases the interfacial surface area and provides capacitive charge injection without generating/consuming chemical species during electric stimulation, thus promoting high-fidelity stimulation/recording. Electrochemical measurements in Figure 4.2b indicate a low impedance ($|Z|$) for the electrodes in cell culture medium at room temperature. The phase response in Figure 4.2b can be attributed to the complex impedance of the interface and the resistance (RS) of the electrolyte, which is in series connection with the interface. Cyclic voltammetry curves in Figure 4.2c demonstrate that the electrodes are electrochemically active,

seen here as oxidation waves for a ferrocenecarboxylic acid test analyte measured with and without the RGD-modified PDL pretreatment (i.e., the presence of the TiN and adsorbed cell attachment protein modifies but does not block their electrical activities). The top left frame in Figure 4.2d reveals no measurable signals after seeding and culturing DRG neurons for 7 d, consistent with silent behavior during this period[11]. After stimulating DRG neurons using one electrode with a biphasic periodic voltage (frequency: 100 Hz, amplitude: 10 V, duration: 1 s), capacitive charging appears in the electrode–electrolyte double layer. The same electrode subsequently detects 12 spikes (the bottom left frame in Figure 4.2d). Magnified views in Figure 4.2d (right frame) reveal that these spikes have triphasic waveforms with durations of ∼4 ms and amplitudes between 5 and 16 μV, consistent with shapes and durations reported from traditional studies using conventional 2D electrode structures[11-12].

These types of 3D electronic scaffolds, as well as extensions of them that integrate other types of chemical, thermal, electrical, and/or optical sensors and actuators, have potential in many areas, including as vehicles to facilitate the development of in vitro models for drug discovery and toxicology and as tools to accelerate basic research on mechanisms by which stimuli can influence the development of cells, of particular relevance in the exploration of strategies to promote wound healing, tissue repair, disease treatment, and others.

4.2.3 Methods

Fabrication of 3D electronic scaffolds. Fabrication of 3D electronic scaffolds began with spin coating a sacrificial layer of poly(methyl methacrylate) (PMMA, 60 nm in thickness) on a silicon wafer. Spin casting, photolithography, and RIE formed a pattern of PI (4 μm in thickness) on top of the PMMA. Next, spin casting, photolithography, electron beam evaporation, wet etching, and

lift-off patterned Cr/Au/TiN (10 nm/300 nm/50 nm in thickness) onto selected regions of the PI structure as the electrodes and conductive interconnections. Another layer of PI (3 μm in thickness) was patterned on top of the first, in a matching geometry but with circular openings to define the electrodes (50 μm in diameter). Dissolving the PMMA in acetone enabled transfer of the resulting 2D precursors to water-soluble tape. Electron beam evaporation of Ti/SiO_2 (5 nm/50 nm in thickness) through a shadow mask defined bonding sites. The remaining steps followed procedures described in previous chapters.

Transfer printing of 3D electronic scaffolds. Formation of 3D electronic scaffolds followed procedures described in previous chapters, but with Al_2O_3 sacrificial layers deposited between the bonding sites and the elastomer substrates. Transfer printing began with melting solid wax at elevated temperatures (125 °C for Crystalbond 509 or 90 °C for paraffin wax) and then casting this material onto the samples to cover the entire 3D electronic scaffold. Cooling to room temperature resolidified the wax to form a sacrificial carrier. Immersion in HCl (37% by weight) for 24 h removed the Al_2O_3 to release the structures embedded in wax. Transfer printing allowed delivery onto target substrates coated with one of three different types of adhesives: PDMS, silver conductive epoxy (CircuitWorks CW2400, ITW Chemtronics), or tissue adhesives (Vetbond, 3M). After curing the adhesive at room temperature, immersing the samples in an organic solvent (acetone for Crystalbond 509 and toluene for paraffin wax) at 70 °C dissolved the wax to complete the process**.**

Adult rat DRG isolation. All work with live animals was performed in full compliance with local and federal guidelines for the humane care and treatment of animals and in accordance with

approval by the University of Illinois at Urbana–Champaign IACUC animal use protocol. Sprague-Dawley male rats were quickly decapitated using a sharp guillotine. Spine vertebrae were surgically cut on both side between pedicle and lamina in the area of the facet of superior articular process. This cut exposed the spinal cord, which was removed. Additional cuts on sides and in the middle of the ventral portion of the vertebral column created two chains of vertebra pieces with easily visualized DRGs. DRGs were removed using fine forceps and placed into the Hibernate A (Life Technologies) solution located on ice.

Scaffold preparation for DRG cell seeding and culture. Transfer-printed 3D electronic scaffolds were rinsed with ethanol, then sterilized by exposure to UV light (300-W lamp) in a laminar flow hood for 30 min. Scaffolds were immersed in a 100 µg/mL RGD-modified PDL solution for 60 min before seeding.

Primary adult rat DRG dissociation and seeding. Approximately 20 lumbar and thoracic DRGs from an adult rat were collected and stored in Hibernate A up to 2 d before seeding. The Hibernate medium was then removed. The DRGs were treated with 0.25% collagenase in DRG physiological media for 1.5 h at 37 °C, and shaken a few times during incubation, strongly upon completion of the incubation period. The DRGs were centrifuged (200 × g) for 2–3 min to remove supernatant, and washed with HBSS. After another centrifugation to remove the HBSS, the DRG were incubated in 0.25% trypsin with EDTA for 15 min at 37 °C. The DRGs were centrifuged to remove supernatant, resuspended in DRG media + 1% FBS for 50 s to inactivate trypsin, and triturated. Once some of the pellet resettled, the supernatant was collected and centrifuged for 5 min at 200 × g. The resulting pellet was washed with HBSS and centrifuged to remove supernatant. Pelleted

cells were resuspended in the desired amount of DRG media containing the glial inhibitor AraC, usually 1 mL per 10 original DRGs. After cell seeding, the scaffolds were incubated overnight at 37 °C to allow for cell attachment before an additional 2 mL per Petri dish (3 mm in diameter) of DRG media was added. The medium was changed twice every 7 d. The concentration of AraC in the DRG media was kept at 0.3 μM from the moment of cell seeding until the end of the culture.

Immunocytochemistry–neuronal extensions (MAP2)/glia (GFAP)/nuclei staining. After 7 d in culture, neurons were rinsed 3× with PBS (37 °C), immersed in 4% paraformaldehyde (37 °C) at ambient temperature (23–25 °C) for 20 min, and then rinsed again with PBS, five times (last time for 5 min on a shaking board). A PBS solution containing 0.25% Triton X-100 was added to the samples for 10 min to permeabilize cellular membranes, before rinsing again with PBS five times. The samples were incubated in a 5% Normal Goat Serum for 30 min before rinsing again with PBS five times. The samples were then exposed to primary rabbit anti-MAP2 antibody at a 1:1000 dilution at 4 °C overnight and then rinsed five times with PBS. Next, the samples were exposed to primary chicken anti-GFAP (1:1000 dilution) antibody at room temperature for 1 h and then rinsed five times with PBS. Secondary Alexa 594 anti-rabbit and Alexa 488 anti-chicken IgG antibodies (1:200) were added to the samples, which were allowed to incubate for 1 h (23–25 °C). The samples were then rinsed with PBS five times. Finally, the samples were incubated with 0.002% DAPI in PBS for 1 min and rinsed with deionized water for 30 s–1 min. The samples were covered with two to three drops of antifade mounting media and a coverslip was set on top of the mounted sample.

Confocal fluorescence imaging. Tiled images of the entire scaffold were obtained using the 10× objective, were composed of either 2 × 2 tiles (927 μm × 927 μm) or 4 × 4 tiles (1270 μm × 1270 μm), depending on the scaffold architecture. These 10× magnification images required no immersion medium and were taken with an EC Plan-Neofluar N.A. = 0.3. In addition, single-frame and 2 × 2 tiled images (250 μm × 250 μm) were captured using a 40× objective for data analysis. The 40× magnification images were taken in Zeiss Immersol 518 immersion medium with refractive index n = 1.518 at 23 °C. Oversampling for all images was at least 2× as dictated by Nyquist sampling. Pinhole diameters for all images ranged from 1 to 2 airy unit (AU), with most measurements performed at ~1.6 AU. A 20% tile overlap and online stitching permitted high-resolution large-area imaging of scaffold structures of interest. Confocal z stacks were reconstructed using ImageJ software.

Electrophysiological recordings. All extracellular recordings used an ac-coupled differential amplifier (model 1700; A-M Systems). Signals were filtered with a 300-Hz high-pass filter and a 1-kHz low-pass filter. Amplified signal was digitized by Digidata 1322A (Molecular Devices) at 6.7 kHz.

4.3 Compliant and Stretchable Thermoelectric Coils for Energy Harvesting

With accelerating trends in miniaturization of semiconductor devices, techniques for energy harvesting become increasingly important, especially in wearable technologies and sensors for the Internet-of-things. Although thermoelectric systems have many attractive attributes in this context, maintaining large temperature differences across the device terminals and achieving low thermal impedance interfaces to the surrounding environment become increasingly difficult to

achieve as the characteristic dimensions decrease. Here, we propose and demonstrate an architectural solution to this problem, where thin film active materials integrate into compliant, open three-dimensional (3D) forms. This approach not only enables efficient thermal impedance matching, but it also multiplies the heat flow through the harvester, thereby increasing the efficiencies for power conversion. Interconnected arrays of 3D thermoelectric coils built using microscale ribbons of monocrystalline silicon as the active material demonstrate these concepts. Quantitative measurements and simulations establish the basic operating principles and the key design features. The results suggest a scalable strategy for deploying hard thermoelectric thin film materials in harvesters that can integrate effectively with soft materials systems, including those of the human body.

4.3.1 Fabrication and Design Approaches

Our demonstration of this thermoelectric helical coil architecture uses monocrystalline silicon as the active material, as shown in the schematic illustration of Figure 4.3a. Here, mechanically guided assembly generates 3D helical structures from 2D serpentines via compressive buckling induced by relaxing a previously stretched elastomer substrate to which the serpentines bond at selected locations; strong chemical bonds follow from condensation reactions between surface hydroxyl groups on the surface of the elastomer and patterns of silicon oxide formed on the serpentines (see detailed fabrication procedures in Section 4.3.5). The serpentines incorporate silicon ribbons with p- and n-type segments, termed p- and n- "legs," connected in a series arrangement by lithographically patterned traces of metal. Polymer coatings formed on the top and bottom sides encapsulate the system in a manner that also locates the silicon at the neutral mechanical plane to enhance fabrication yields during the bending and twisting deformations

associated with transformation from 2D to 3D, and during deployment and use. In the final configuration, the legs serve as the pathways for thermal transport between the substrate and the environment. Specifically, as the substrate equilibrates with the thermal source, heat passes into the coils at the bonding locations. The encapsulation layers have widths larger than those of the silicon ribbons to increase the surface area as the cold-side heat exchanger and to provide mechanical support and protection. As mentioned previously, the 3D coils also provide remarkable levels of mechanical compliance and robustness during handling and bending (Figure 4.3b), even though they incorporate heavily-doped silicon (fracture strain ~ 0.1%[13]). The assembly process can naturally scale to large arrays without deviating from the geometry predicted by the FEA (Figure 4.3c). Such characteristics render these systems well suited for forming intimate thermal interfaces to the human body, such as the wrist or ankle (Figure 4.3d), as well as other objects with curvilinear shapes. Although the examples presented here utilize a particular set of materials, fabrication schemes and device geometries, and the overall concepts have broad applicability.

The mechanical and thermal properties of 3D coils can be accurately predicted by the FEA, such that a full-scale, thermo-mechanically coupled model can provide critical guidance on selection of materials and geometrical configurations. An optimized layout based on using silicon (thickness = 0.2 μm) and polyimide (PI; total thickness = 8 μm) as active and encapsulating materials, respectively, incorporates a tapered serpentine geometry. The unit leg length is 1.57 mm with a constant curvature, and the PI widths at the top and bottom of the leg are 0.34 mm and 0.17 mm, respectively (i.e. ratio is 2). The following sections summarize the thermal and mechanical aspects of this computationally guided optimization process.

4.3.2 Thermal Design Principles: Heat Exchange and Impedance Matching

The advantages of the 3D architecture follow from a set of thermal aspects that are favorable for effective harvesting, which can be understood with some basic device principles[14-15]. For a total heat flow $\dot{Q}$[W] through a device, the harvested power can be written as $P = \eta\dot{Q}$ where η is the conversion efficiency. Here, only $\dot{Q}$ through the thermoelectric legs $\dot{Q}_{\mathrm{TE}}$, i.e. through silicon in our case, can be converted; any heat bypassing the legs does not contribute to $\dot{Q}_{\mathrm{TE}}$ and is referred to as "parasitic." The value of η is proportional to the difference in temperature across the thermoelectric leg ΔT_{TE}, as $\eta \approx \eta_0 \Delta T_{\mathrm{TE}}/T_{\mathrm{H}}$ in a harvesting environment that involves small thermal gradients and a given hot side temperature T_{H}. Here, η_0 depends on the thermoelectric figure-or-merit (zT) but not on the device design[14]. According to $P = \frac{\eta_0(zT)}{T_{\mathrm{H}}}\Delta T_{\mathrm{TE}}\dot{Q}_{\mathrm{TE}}$, the device design goal with a given thermoelectric material and hot side temperature is to maximize the product $\Delta T_{\mathrm{TE}}\dot{Q}_{\mathrm{TE}}$.

Because changes in many geometric parameters of the device (e.g. leg length) change $\dot{Q}_{\mathrm{TE}}$ and ΔT_{TE} in opposite directions, the most fundamental limiting factor – the heat exchange capability – should be optimized at the first step of design. The heat exchange capability describes how well the device can receive and dissipate heat from the hot and cold sources, represented by the inverse of the total thermal impedance for heat exchange $1/\Theta_{\mathrm{ex}}$; it determines the upper limit of $\dot{Q}_{\mathrm{TE}}$ because $\dot{Q}_{\mathrm{TE}} < \Delta T_{\mathrm{Envi}}/\Theta_{\mathrm{ex}}$, where ΔT_{Envi} is the temperature difference between the heat source and the surrounding environment. Once the design features that give a minimal Θ_{ex} are identified, the next step for optimization is to find specific geometric parameters that could produce the maximum $\Delta T_{\mathrm{TE}}\dot{Q}_{\mathrm{TE}}$. In traditional device geometries, the optimum point occurs when Θ_{ex} is similar to the impedance of the leg Θ_{TE} [15] because Θ_{TE} increases ΔT_{TE} but decreases $\dot{Q}_{\mathrm{TE}}$,

analogous to load impedance matching in electronics. This condition is the thermal impedance matching condition (see Appendix B for details).

Following this optimization strategy, we first find the design feature that maximizes the heat exchange capability (minimizes Θ_{ex}). We take advantage of the 3D design space that allows for a large surface area; in harvesters that rely on passive cooling from air convection, the surface area on the cold side determines the total heat flow. In the 3D helical coil system of Figure 4.3, all surfaces except those in contact with the substrate serve as cooling interfaces, with total areas that are much larger than the bonding area. We highlight the role of the leg encapsulation layer, which not only provides mechanical support, but also strongly enhances the heat exchange from an enlarged surface area. Analogous to conventional cooling fins, the optimal geometry for cooling is a diverging profile toward the cold side (i.e. top side). We thus employ a tapering geometry that increases in width towards the top (Figure 4.4). This top-side wide geometry, however, will inevitably increase the load applied to the leg, compromising mechanical stability. Therefore, the thermally favorable design should be limited to within the mechanical stability range.

To find the optimal tapered geometry, we simulated the dependence of the thermal and mechanical response on the encapsulation layer geometry using FEA. As indicated in Figure 4.4a, simply adding a non-tapered encapsulation layer to the bare silicon increases $\dot{Q}_{\mathrm{TE}}$ by three-fold (6.2 to 19.3 μW). Tapering the encapsulation to a higher cold-to-hot side area ratio further increases $\dot{Q}_{\mathrm{TE}}$, as expected. The increased heat flow also results in a lower cold side temperature (Figure 4.4b). The maximum strain in the silicon leg also increases with tapering, reaching the silicon fracture limit at a tapered ratio of three (Figure 4.4c). In addition, the fabrication yield associated with 3D assembly decreases with tapering because buckling in the downward direction (competing with the upward direction) becomes an increasingly favorable mode. To remain in the

mechanically stable regime, we selected a cold-to-hot side area ratio of two. We note that this design strategy – to increase the cold side heat exchange with an encapsulation layer – is unique for 3D thermoelectric harvesters. In an in-plane harvester where the surface area is fixed, substrates and encapsulation layers only increase parasitic heat flow, but not $\dot{Q}_{\mathrm{TE}}$.

The next focus is on conditions for thermal impedance matching. High heat flow is only beneficial if thermal impedance matching is possible. This condition can be easily achieved in the 3D coil structure because the leg length can be adjusted up to hundreds or thousands of microns; the thermal resistance of the leg is proportional to its length. Simulation results show that the impedance matching condition can be achieved with a leg length ≈ 1.5 mm (Figure 4.4d), at which a maximum in $\Delta T_{\mathrm{TE}}\dot{Q}_{\mathrm{TE}}$ (normalized by area and T_{H}) is found. We emphasize that the $\Delta T_{\mathrm{TE}}\dot{Q}_{\mathrm{TE}}$ calculated here includes only the heat input into the silicon, excluding any parasitic heat. The ability to adjust ΔT_{TE} across such a wide range (and thus obtain the impedance matching condition) in our design is a key differentiating feature relative to conventional film-based harvesters, where only an extremely small ΔT_{TE} is possible in the out-of-plane direction.

We note that our design scheme is optimized for harvesting in miniature devices. Because of the priority on minimal occupied space and weight, cooling is made to rely on natural convection. This cooling process dominates the thermal impedance of the harvester, making other design factors like substrate-to-leg conductance much less significant. Instead, increasing the total surface cooling capacity is of utmost priority, exemplified by the fact that the leg encapsulation layer actually enhances the heat flow through the leg (Figure 4.4a; 9.7 nW increase in silicon heat flow by adding a non-tapered encapsulation) despite it introducing parasitic heat flow (2.9 nW) . In other words, the benefit of increased cooling capability greatly outweighs any losses from parasitic heat flow, a regime which might be counterintuitive from the aspect of bulk generators.

4.3.3 Mechanical Compliance

One of the key advantages of our device is the mechanical compliance to endure substantial amount of bending, in-plane stretching and out-of-plane compression, as opposed to previously reported out-of-plane harvesters[16-21] with limited flexibility or stretchability. As shown in Figure 4.5, these 3D structures can be stretched in the in-plane direction by up to 60% for hundreds of cycles (Figure 4.5a-c) and can be vertically compressed up to 30% with only minimal degradation in the electric properties (Figure 4.5d-e). This exceptional level of mechanical compliance in a structure that incorporates silicon follows from a design principle that places silicon in the neutral mechanical plane with respect to deformation, as also predicted by FEA. This design also ensures that the strains in the encapsulation and metal layers are well below the threshold for plastic yielding. Stretching in the plane reduces the material strains, as it returns the structure to its original, undeformed 2D geometry. Uniaxial stretching over 200 cycles does not lead to signs of electrical or mechanical failure (Figure 4.5b-c). Comparable results were also found on the 8×8 array (Figure 4.3c), where 200 cycles of 60% biaxial stretching resulted in a 22% increase in resistance from 335.4 to 409.7 kΩ.

For vertical compression, measurements indicate the onset of changes in resistance at ~ 30% before fracture of the silicon causes an open circuit (Figure 4.5e), also consistent with FEA in Figure 4.5d. The overall resilience of the 3D coil suggests the potential to interface with various miniature device schemes. For example, suitable designs allow for system-level properties that are mechanically and geometrically compatible with those of the soft tissues of the human body.

As most inorganic thermoelectric materials, such as Bi_2Te_3-Sb_2Te_3 alloys[22], Zn_4Sb_3[23], and Cu_2Se[24], have fracture strains similar to silicon, the measurements and FEA results described above suggest that they could be deployed in similar 3D structures with comparable mechanical

properties. Use of thermoelectric materials based on organic polymers could further enhance the mechanics and also the heat flow properties.

4.3.4 Power Output and Projections

The output characteristics of the harvester (Figure 4.6a-b) that consists of an 8×8 array of coils (Figure 4.3c) are consistent with the design expectations outlined in previous sections. Using measurement procedures outlined in Section 4.3.5, the open circuit voltage is 51.3 mV at ΔT_{Envi} = 19 K, yielding an estimated temperature drop of 6.2 K across each individual leg based on an average thermopower of 65 μV/K measured from the pre-patterned silicon. This value is consistent with measurements from a 3×1 array (6.9 K), and somewhat smaller than the design estimation of 9.5 K (Figure 4.5d). The discrepancy follows, at least partly, from uncertainties in the thermal transport parameters used for simulation. In comparison to most literature reports[16-17] where even bulk material harvesters are operated significantly far from thermal impedance matching conditions, these results demonstrate the promise of our matching strategy. The open circuit voltage does not diminish over time in our measurements, indicating that the thermal profile in our device is at steady-state. The maximum power output, i.e. ~ 2 nW, is modest, mainly because of the low zT of silicon.

The good agreement between modeling and experiment allows use of simulation results to estimate power outputs for harvesters built with other materials, specifically those with better figure-of-merit $zT > 0.1$ than silicon ($zT > 0.001$ at 300 K). Recall that $P = \frac{\eta_0(zT)\Delta T_{\mathrm{TE}}\dot{Q}_{\mathrm{TE}}}{T_{\mathrm{H}}}$. For T_{H} = 313 K, we simulate $\Delta T_{\mathrm{TE}}\dot{Q}_{\mathrm{TE}}$ for designs relevant for two different groups of materials, inorganic and organic, while keeping the occupied area of the coil the same as that of the encapsulated silicon design. For organic-based materials (dashed line, Figure 4.6c), we find $\frac{\Delta T_{\mathrm{TE}}\dot{Q}_{\mathrm{TE}}}{T_{\mathrm{H}}}$ = 0.83 μW (similar

to the 0.73 μW of encapsulated silicon) based on a design that simply replaces the silicon and encapsulation entirely with the organic thermoelectric material. For inorganic materials (solid line, Figure 4.6c), the encapsulation again defines the surface area profile and maintains mechanical stability, but the reduced thermal conductivity compared with silicon results in $\frac{\Delta T_{\mathrm{TE}} \dot{Q}_{\mathrm{TE}}}{T_{\mathrm{H}}}$ = 0.41 μW based on Bi_2Te_3-Sb_2Te_3. Nevertheless, power output is generally higher by virtue of the higher zT yielding a higher conversion efficiency. Overall, by integrating known thermoelectric materials, power output at the level of a few μW appears to be possible. Such an improvement to 0.15 μW per coil would allow 100 μW of power from an area of a typical wrist watch (~10 cm^2) when a similar ΔT_{Envi} is given. Room for further improvement up to an order of magnitude in total exists from packing coils more efficiently, using designs better optimized for the low-thermal conductivity thermoelectric material, and stacking the coils in 3D with repeated transfer printing[25].

Our fabrication scheme is generally compatible with other materials, especially the organic variants in Figure 4.6c which allow minimal use of encapsulation layers. Additional opportunities for improvement in harvesters that use inorganic materials is in the development of thick (or wide) films to reduce the effects of parasitic heat flow through the encapsulation layers, while maintaining mechanically stable designs. For organic or composite materials, additional research on methods for deposition, doping and patterning could yield progress. For all classes of thermoelectric materials, the mechanical properties become more important to understand in the context of the sorts of 3D configurations reported here. A related challenge is to identify materials and compatible metals that do not suffer from electrical resistance increases during the 2D-to-3D mechanical transformation. In the current case of silicon, typically a three-fold increase in resistance is observed during the transformation, possibly due to electrode contact degradation and

plastic deformation in some parts of the leg. These various areas represent promising directions for future research.

4.3.5 Methods

Patterning and transfer printing of p- and n- doped single-crystalline silicon. Single-crystalline films of silicon with thickness of 200 nm (silicon-on-insulator, SOI, Soitec) served as the thermoelectric material. A layer of SiO_2 (500 nm) formed on the top silicon by plasma-enhanced chemical vapor deposition served as masks for doping. Patterning relied on photolithography and a combination of reactive ion etching (CF_4+O_2) and wet etching (buffered oxide etchant) to define openings in the SiO_2 for solid-state diffusion doping. The p- and n- type regions resulted from doping with boron (1000 °C, 14.5 min) and phosphorus (1000 °C, 5.5 min), respectively. Each dopant type required its own SiO_2 mask. A photolithographically patterned layer of photoresist (S1805, MicroChem) defined regions of via holes (3 μm diameter, 50 μm pitch), formed through silicon by reactive ion etching (SF_6). These holes also enabled etching of the buried oxide layer by immersing the wafer in 49% hydrofluoric acid for 30 min. Thoroughly rinsing the sample with deionized water prepared it for transfer printing. A flat slab of polydimethylsiloxane (Sylgard 184, 1:4) enabled retrieval of the photoresist/Si film and delivery onto a bilayer of polyamic acid (precursor to form polyimide 4 μm, PI 2545, HD MicroSystems) and poly(methylmethacrylate) (200 nm, PMMA, MicroChem) spin coated sequentially on a silicon handling wafer. Immersion in acetone dissolved the photoresist. Baking in a vacuum oven completed the curing of the polyimide (PI). Finally, photolithography and reactive ion etching (SF_6) patterned the silicon into isolated p- and n-type serpentine-like layouts.

Fabrication of the 2D thermoelectric precursor and the 3D spring structure. Bilayers of Ti (60 nm) / Au (60 nm) deposited by electron beam evaporation and patterned by photolithography and wet etching served as electrical interconnects between the p- and n- type silicon. This process also defined electrode pads for probing. Spin coating another layer of PI (4 μm) and patterning it by exposure to an oxygen plasma through a mask of photoresist (10 μm, AZ 4620, MicroChem) encapsulated the system and completed the fabrication of the 2D thermoelectric precursor. Dissolving the residual photoresist and the underlying PMMA in acetone allowed the precursor to be retrieved onto a piece of water-soluble tape (Aquasol). A pattern of SiO_2 (50 nm) formed by electron beam evaporation through a shadow mask defined bonding sides on the back side of the precursor. An elastomer substrate (Dragon Skin 10, 1:1, Smooth-On Inc.) stretched to the desired level using a stage served as a substrate for 3D assembly. Exposing the elastomer and the 2D precursor (still on water-soluble tape) to ultraviolet induced ozone (Jelight UVO-Cleaner, 144AX) and then laminating to the two together and baking them in a convection oven at 70 °C formed strong adhesion via condensation reactions at the bonding site interface. Dissolving in warm water removed the tape. Slowly releasing the strain in the elastomer substrate while immersed in water completed the 3D assembly.

Thermoelectric characterization. Transport properties of the doped silicon films were characterized at room temperature. Electrical conductivity and Hall measurements used the van der Pauw method with Mo probes. A 2 T electromagnet generated the magnetic field. Measurements of electrical conductivity used an in-line four-point Os probe setup, to yield results consistent with those from the van der Pauw method. The in-plane Seebeck coefficient of the doped silicon film was measured using a scanning probe setup[26] with a maximum temperature difference

of ~ 8 K. The thermoelectric response of the coil harvester was measured by placing the device on a Cu block that was heated using a film heater attached on the bottom side of the block. A type K thermocouple was attached to the bottom of the harvester substrate, and the film heater was PID controlled to maintain the harvester bottom temperature at 40 °C. Room temperature was measured using another type K thermocouple placed in air near the harvester. The entire setup was built inside a probe station enclosed in a dark box. Electrodes were probed using W needles. The output voltage and current were measured at varied load resistances. To achieve the equivalent effect of switching the load resistance, a source measurement unit (Keithley 2400) was used under current-scanning mode.

Mechanical characterization. The cyclic stretching tests involved loading the harvester device onto a stretching stage, then uniaxially stretching and releasing between 0 and 60% at a strain rate of 0.013 s^{-1}. The vertical compression tests involved compression up to 40% applied by carefully sandwiching the device between two stiff plates and displacing the top plate using a piezoelectric stage (PI-USA, Waltham MA). The total compression was estimated based on the initial nominal coil diameter of 660 μm. Applying force through a steel spherical probe to the cover glass base ensured that the sandwiching plates remained in a parallel configuration. In addition, force measurements and side-view monitoring confirmed the uniform loading on multiple coils. Force was measured through the displacement of a 4-bar flexure monitored by capacitive sensors (Lion Precision, Oakdale MN). The transducer stiffness was ~ 1020 N/m, much stiffer than the out-of-plane stiffness of the devices themselves; the flexure displacement was added on to the prescribed displacement for vertical compression to reach targeted values.

4.4 Soft 3D Vibratory Platforms for Nanomechanical Sensing

Vibrational resonances of microelectromechanical systems (MEMS) can serve as means for assessing physical properties of ultrathin coatings in sensors and analytical platforms. Most such technologies exist in largely two-dimensional (2D) configurations with a limited total number of accessible vibration modes and modal displacements, thereby placing constraints on design options and operational capabilities. This study presents a set of concepts in three-dimensional (3D) microscale platforms with vibrational resonances excited by Lorentz-force actuation for purposes of measuring properties of thin film coatings. Nanoscale films including photodefinable epoxy, cresol novolak resin, and polymer brush with thicknesses as small as 270 nm serve as the test vehicles for demonstrating the advantages of these 3D MEMS for detection of multiple physical properties, such as modulus and density, within a single polymer sample. The stability and reusability of the structure are demonstrated through multiple measurements of polymer samples using a single platform, and via integration with thermal actuators, the temperature-dependent physical properties of polymer films are assessed. Numerical modeling also suggests the potential for characterization of anisotropic mechanical properties in single or multilayer films. The findings establish unusual opportunities for interrogation of the physical properties of polymers through advanced MEMS design.

4.4.1 3D Multimodal Vibratory Systems Actuated by Lorentz-Force

Figure 4.7a is a schematic illustration of a representative 3D system assembled on an elastomeric substrate. The overall size, as measured by the distance between the two sites at which the structure bonds to the substrate, is 800 μm. The critical dimension, as defined by the width of the narrowest ribbon, is 100 μm. As shown by the exploded view in Figure 4.7b, this platform

consists of a layer of patterned conductive traces (Au, thickness = 300 nm) sandwiched between two layers of polyimide (PI, thickness ~2.5 μm for each). The PI layers not only form the structural components of the system, but they also encapsulate and protect the traces. The 3D architecture results from mechanical buckling of a 2D precursor via controlled release of a prestretched elastomeric substrate, as described in previous chapters. The detailed fabrication process for the precursors appears in Section 4.4.6. Briefly, layers of PI and gold are consecutively deposited on a silicon wafer and patterned using photolithography. Dissolution of a sacrificial layer of poly(methyl methacrylate) (PMMA) releases the precursor formed in this manner from the underlying wafer. The planar nature of the process then allows integration of nanoscale polymer films as test vehicles with a wide range of thicknesses and geometries. In this work, we demonstrate the use of a photodefinable epoxy (SU8), a cresol novolak resin (S1805), and a polymer brush (PNIPAm) as test films, patterned onto the 2D precursors via photopolymerization, photolithography and selective growth respectively (see Section 4.4.6 for details).

Figure 4.7c highlights the systems for Lorentz-force actuation and optical measurement. The Lorentz force follows from use of a sinusoidal voltage source (1.5V, Keithley 3390) to create an alternating current (AC) through the traces, with a permanent magnet (neodymium disc) placed underneath the 3D structure to induce a static magnetic field in the z-direction. The result is an AC oscillatory force at the frequency of the current, imparted onto the traces at a direction perpendicular to the current and the magnetic field. The amplitude of the Lorentz force can be estimated by $F = B \times I_{rms} \times L_{Au} \approx 12.5$ μN (magnetic field [B] ≈ 0.5T; rms value of electric current [I_{rms}] = 25 mA; gold wire length [L_{Au}] = 1 mm). The optical measurement system uses apparatus based on lock-in detection of laser light scattered from the 3D structure. The amplitude of such a measurement is approximately proportional to the amplitude of the vibration. Additional details

are in Section 4.4.6. Changing the position of the magnet alters the direction of the magnetic field to allow actuation of targeted vibration modes. Figure 4.7d illustrates the lowest in-plane and out-of-plane vibration modes, obtained by FEA. Experimentally, these modes are excited by placing the magnet below (denoted as mode 1) and to the left of the 3D structure (denoted as mode 2), respectively.

4.4.2 Characterization of Modulus and Density Using Multimodal Resonances

The effects of the patterned polymer films under test on the vibrational frequencies of these two modes allows determination of both the modulus and density of the same sample. Dimensional analysis (see Appendix B for details) and FEA suggest a linear relationship between the resonant frequency and the polymer modulus and density

$$\frac{f}{f_0} = C_{\mathrm{E}} \frac{E_{\mathrm{P}} h_{\mathrm{P}}}{\hat{E}_{\mathrm{Base}} h_{\mathrm{Base}}} - C_{\rho} \frac{\rho_{\mathrm{P}} h_{\mathrm{P}}}{\hat{\rho}_{\mathrm{Base}} h_{\mathrm{Base}}}, \tag{1}$$

where f and f_0 are the resonant frequencies with and without the polymer, E_{P}, ρ_{P} and h_{P} are the polymer modulus, density and thickness, $\hat{E}_{\mathrm{Base}}$, $\hat{\rho}_{\mathrm{Base}}$ and h_{Base} are the effective modulus, average density and thickness of the PI/Au/PI tri-layer, respectively (see Appendix C. 1 for details); and the dimensionless parameters C_{E} and C_{ρ} depend on the topology of the 3D vibratory platform, the vibration mode and the polymer patterns and the gold circuit patterns. For the 3D structure, vibration modes and polymer/gold patterns in Figure 4.8a&b, FEA gives $C_{\mathrm{E}(1)} = 0.44$, $C_{\rho(1)} = 0.30$ for mode 1 and $C_{\mathrm{E}(2)} = 0.20$, $C_{\rho(2)} = 0.30$ for mode 2. The results indicate that the specific designs of the polymer patterns and the vibration modes enable partial decoupling of the sensitivities of resonant frequencies to the polymer modulus and density. In particular, the resonant frequency of mode 1 is 2.2 ($C_{\mathrm{E}(1)}/C_{\mathrm{E}(2)}$) times more sensitive to the polymer modulus than that of mode 2, as

measured by the slope of the curves in Figure 4.8a. Meanwhile the resonant frequencies of both modes are sufficiently sensitive to the polymer density. The design of the polymer patterns follows from use of a FEA-based algorithm that optimizes the contribution of the polymer to the strain energy and the kinetic energy of the vibrations (see Appendix C. 2 for details). The developed scaling law serves as the basis of an inverse problem to determine the polymer tensile stiffness ($E_P h_P$) and mass ($\rho_P h_P$) from the measured resonant frequencies (see Appendix C. 3 for details).

In principle, the method is applicable to evaluation of any type of material (polymers, metals, ceramics), but the tensile stiffness ($E_P h_P$) and mass ($\rho_P h_P$) of the films must be at least one order of magnitude smaller than those of the base layer ($\hat{E}_{Base} h_{Base} = 1.36 \times 10^4$ N/m and $\hat{\rho}_{Base} h_{Base} = 0.013$ kg/m^2 for the design shown in Figure 4.8a), such that the linear relationship in Eq. (1) applies. In such cases, to deduce the elastic modulus (E_P) and density (ρ_P) of the polymer from multimodal frequency measurements, the thickness (h_P) of the polymer film must be known. Measurements of thickness are most easily performed prior to 3D assembly, in the precursor 2D geometry with techniques such as surface profilometry or spectroscopic ellipsometry (see Section 4.4.6 for details), with uncertainty of ~5%.

As an example, Figure 4.8c and 4.8d show experimental measurements of the response curves of mode 1 and 2 respectively, for the case of a patterned layer of a photodefinable epoxy (SU8; thickness = 610 nm). The resonant frequencies are $f_{(1)}$=30.6 kHz, $f_{0(1)}$ =28.8 kHz for mode 1, and $f_{(2)}$ =28.4 kHz, $f_{0(2)}$ =27.9 kHz for mode 2. The repeatability of the measurement is ~0.1%, as defined by the standard deviation of four measurements performed in sequence. The effective modulus, average density and thickness of the base layer are $\hat{E}_{Base} = 2.51$ GPa , $\hat{\rho}_{Base} = 2.41$ g/cm^3 and $h_{Base} = 5.4$ μm , respectively. Inserting these values into Eq. (1) yields the modulus

$E_P = 3.8 \pm 0.4$ GPa and density $\rho_P = 1.3 \pm 0.3$ g/cm^3 of the epoxy, as presented in Figure 4.8e. The combined uncertainties in thickness and frequency lead to ~10 % and ~20% uncertainties in the extracted film modulus and density, respectively (see Appendix C. 4 for details). The ~5% discrepancies between the modulus and density values reported here and those in the literature (SU8 modulus 4.02 GPa; SU8 density 1.22 g/cm^3) are within the uncertainties.

4.4.3 Robustness and Reusability of 3D Vibrators

The elastic, reversible nature of the 3D assembly process allows repetitive use of these measurement platforms. Specifically, after measuring one polymer sample, applying tensile strain on the underlying elastomeric substrate fully returns the 3D structure to its unbuckled, 2D form, thus allowing the removal of the film under test and application of another material (Figure 4.9a&b). Release of the tensile strain re-assembles the 3D structure for frequency measurements. Cycling tests that involve 500 cycles of stretching/release reveal a resonance frequency shift of less than 0.3% (from 34.90±0.03 kHz to 35.00±0.03 kHz), despite an increase in circuit resistance of ~20% perhaps due to some level of plastic yielding in the gold layer. Because the gold (300 nm) is much thinner than the PI (~5-6 μm) and because it is positioned at the neutral mechanical plane, its plastic yielding has a minor effect on the overall resonant frequency. As a demonstrating example, Figure 4.9c shows a set of experimental results on two cresol novolak resin (S1805) films with different thicknesses (450±30 nm and 650±40 nm), actuated with mode 1. Note that after washing away S1805 with acetone, the response curve of the 3D vibrator matches the initial polymer-free state exceptionally well, indicating good robustness and repeatability of the system, as well as effectively complete removal of S1805.

4.4.4 Integration with Thermal Actuators for Temperature-Dependent Measurements

The compatibility with planar fabrication technologies allows integration of additional actuating and sensing elements, via a few additional fabrication steps. As a specific example, thermal actuators allow studies of modulus as a function of temperature. Figure 4.10a shows schematic illustrations of a modified 3D platform that includes this functionality. A bilayer of photodefinable epoxy (SU8, thickness = 40±2 nm) and a poly(N-isopropylacrylamide) (PNIPAm) brush (thickness = 270±20 nm) patterned directly on top of the thermal actuators serve as the test sample (see Section 4.4.6 for experimental details). Figure 4.10b shows the FEA calibration of the temperature change versus direct current input for the thermal actuator. The temperature change at the polymer region is uniform, as illustrated by the inset of Figure 4.10b. The experimental results in Figure 4.10c show as expected that the resonant frequency decreases as the temperature increases. Measurements for three cycles of heating are in Figure 4.10c, where the peak temperature is 80 ℃ in the polymer in cycle 1 (denoted by the blue solid triangles) and 300 ℃ in cycles 2 (red solid circles) and 3 (black solid squares). The sharp, ~0.5±0.05 kHz decrease in resonant frequency at 40 ℃~50 ℃ corresponds to the glass transition of PNIPAm, while the ~0.2±0.05 kHz decrease at 100 ℃~150 ℃ corresponds to that of SU8. The measured glass transition temperature matches well with the literature values for SU8[27], whereas it is lower than the reported values for bulk PNIPAm[28], as expected for this material which contains short polymer chain lengths and has a small thicknesses[29]. During the glass transition, the change in polymer mass ($\rho_P h_P$) is negligible because of mass conservation; the change in polymer thickness is also small (<1%) due to the small coefficient of thermal expansion[30-31] and the small change in temperature across the glass transition. The changes in the moduli of PNIPAm and SU8 films are thus determined from the corresponding resonant frequency shifts to be $\Delta E_{\text{PNIPAm}} = 1.1 \pm 0.2$ GPa

and $\Delta E_{SU8} = 4 \pm 1$ GPa , respectively (Figure 4.10d). The difference between the measured change in modulus of SU8 across the glass transition is consistent with the literature value[27] (3.7 GPa), to within experimental uncertainties. Finally, the further reduction in resonant frequency above 200 ℃ is likely attributable to the onset of softening of PI itself[32].

4.4.5 Potential for Characterization of Anisotropic Elastic Moduli Using Multimodal Resonances

The multimodal resonances of the 3D structures, and the ability to pattern polymers in a precise manner provide routes to determine the elastic moduli of anisotropic materials. Figure 4.11a presents schematic illustrations of the 3D vibratory structure with patterned test films that have transversely isotropic elastic moduli (for instance, oriented polystyrene-block-polydimethylsiloxane films[33]). The optimized polymer patterns (Figure 4.11b) are found using an optimization algorithm for the distributions of strain components. To enhance the sensitivity of the resonant frequencies to the longitudinal component of the modulus, the test polymer should be patterned in locations with the largest strain along the longitudinal direction. The same consideration holds true for the transverse modulus component. Optimized patterns of typical polymers balance these two considerations (see Appendix C. 5 for details). For the current design, the resonant frequency of mode 2 is roughly 2.5 times more sensitive to the transverse modulus ($E_{P(t)}$) than the mode 1 (Figure 4.11c), while the latter is roughly 1.5 times more sensitive to the longitudinal modulus ($E_{P(l)}$, see Figure 4.11d) than the former, as measured by the slopes of the curves in Figure 4.11b&c. This decoupling allows determination of both the longitudinal and transverse moduli by measuring the frequency of mode 1 and 2 with and without the polymer patterns, assuming that the polymer density and thickness are known.

4.4.6 Methods

Fabrication of 3D Vibratory Platform. Fabrication began with spin coating a bilayer of poly(methyl methacrylate) (950 PMMA A4, MicroChem, thickness ~200 nm) and polyimide (PI 2545, HD MicroSystems, thickness ~2.5 μm) on a silicon wafer. Depositing Cr (thickness ~5 nm) and Au (thickness ~300 nm) by electron beam evaporation followed by photolithography and wet etching defined the circuits. Spin coating another layer of PI (thickness ~2.5 um) followed by deposition and patterning of Cr (thickness ~5 nm) and Au (thickness ~50 nm) defined a hard mask in the shape of 2D devices, where the external electrodes were exposed for connections with the function generator. Oxygen plasma etching (March Jupiter III RIE) removes the unmasked PI. After removing the etching mask by wet etching, a layer of polymer was patterned on top to serve as the measurand (see below for details). The underlying PMMA layer was dissolved by immersion in acetone overnight to allow retrieval of the device onto a piece of water-soluble tape. A thin layer of silicon oxide (thickness ~50 nm) deposited on the back side of the sample by electron beam evaporation created the necessary surface chemistry for strong adhesion to the elastomer platform at the bonding sites. The non-bonding sites were protected from SiO_2 deposition by a Kapton shadow mask created by laser cutting. A silicone elastomeric substrate (Dragon Skin 10) was stretched to a desired prestrain (30-40%) using a customized, biaxial stage. After exposing the elastomer and the 2D precursors (still on water-soluble tape) to ultraviolet (UV) induced ozone (Jelight UVO-Cleaner, Model 144AX), the two were laminated together and then baked in a convection oven at 70 °C to yield strong adhesion at the bonding sites where SiO_2 was deposited. Finally, dissolving the tape in warm water and slowly releasing the prestrain completed the assembly process.

Patterning and Characterizing the Thicknesses of the Polymer Films. Patterning the SU8 film used in Figure 2 began with spin coating the SU8 precursor (SU8 2000.5, MicroChem) onto the 2D devices at 2000 rpm for 40 s. After prebaking at 95 °C for 1 min, the film was exposed under an iron oxide photomask with 365 nm UV light at an intensity of 60 mJ/cm^2. Post exposure baking at 95 °C for 1 min and developing in SU8 developer (MicroChem) yielded the desired patterns on the 2D precursors. The sample was then hard bake at 200 °C for 10 min. The thickness was characterized using a profilometer (Dektak 3030) while the 2D precursors were still on silicon wafer.

Patterning of the S1805 films used in Figure 3 began by forming the 3D vibratory platforms as described in the previous section and stretching the elastomeric substrate to fully recover its 2D form. After rinsing the sample with acetone, isopropanol alcohol, and DI water, the S1805 precursor (MicroChem) was spin coated at 4000 rpm (cycle 2, Figure 3b) or 2000 rpm (cycle 3, Figure 3c), followed by baking at 110 °C for 3 min. The elastomeric substrate was then relaxed to return the sample to its 3D form. After each cycle, the sample was thoroughly rinsed with acetone to completely remove the S1805 film.

Patterning of the bilayer of SU8 and poly(N-isopropylacrylamide) (PNIPAm) brush used in Figure 4 began by spin coating SU8 precursor (SU8 2002, MicroChem), diluted using cyclopentanone with a 1:5 volume ratio, onto the 2D devices at 4000 rpm for 40 s. After prebaking at 95 °C for 1 min, the film was exposed under an iron oxide photomask with 365 nm UV light at an intensity of 50 mJ/cm^2. Post exposure baking at 95 °C for 1 min and developing in SU8 developer (MicroChem) defined the desired patterns on the 2D precursors. The sample was then hard baked at 200 °C for 10 min. The PNIPAm brush was selectively grown on the SU8 patterns using surface-initiated atom transfer radical polymerization (SI-ATRP) using previously reported

procedures[34]. Briefly, SU8 surfaces were activated using oxygen plasma for 3 minutes (150 W, March Plasmod GCM-200) and then functionalized with the ATRP initiator (11-(2-Bromo-2-methyl)propionyloxy) undecyltrichlorosilane (BMPOUTS). Devices were placed in a 1 mM solution of BMPOUTS in anhydrous hexanes at room temperature. After 24 hours, substrates were removed, sonicated in hexanes, dried using a nitrogen stream, and placed in a reaction vessel under argon. NIPAM (4.85 g, 42.9 mmol) was diluted with MeOH (15 mL) and H_2O (7 mL) and degassed in a separate Schlenk flask. Then, 1,1,4,7,10,10-hexamethyltriethylenetetramine (HMTETA, 242 μl, 0.89 mmol) and CuBr (53.8 mg, 0.38 mmol) were added to the monomer solution under positive argon flow. Once dissolved, the flask was then sealed and the mixture was transferred to the reaction vessel containing the substrates. Substrates were removed after 10 minutes, sonicated in methanol, ethanol, and water to remove the film residuals in the non-SU8 regions, and then dried in a nitrogen stream.

The thickness of the PNIPAm brush was determined using spectroscopic ellipsometry (VASE, J.A. Wollam Co) on a control sample. Ellipsometric parameters (Ψ, Δ) were measured at three angles of incidence (65°, 70°, 75°) and from 400 nm to 800 nm. Data was analyzed by WVASE software using a three-layer model. Software-supplied refractive indices were used for silicon (substrate) and silicon dioxide (2 nm). Data was fit to a Cauchy layer model, with fixed (An, Bn) values of (1.45, 00.1) and no optical absorption. Control samples were prepared by growing the PNIPAm brush off a silicon wafer that had been patterned with SU8 using the identical conditions as the actual samples. The SU8 layer was determined to be 39.6 nm. After polymerization, the total thickness of the polymer layers (SU-8 and PNIPAM) was determined to be 312.9 nm. Thus, the NIPAM brush thickness is approximately 273.3 nm.

Lorentz-force Actuation System and Optical Measurement System. A function generator (Keithley 3390) applied 1.5 V sinusoidal voltage to the 3D vibratory structure while placed in a static magnetic field induced by a permanent neodymium disc magnet. The Lorentz-force, perpendicular to both the electric current and the magnetic field, oscillated at the frequency of the applied voltage to drive vibrations of the structure.

An optical measurement system was custom-built to measure the dynamics of the 3D vibratory platforms (Figure S3). A focusing lens and mirror delivered a focused laser beam onto the center of the 3D structure. A microscope facilitated alignment. The 3D structure was firmly mounted onto a mechanical stage capable of translation in X-, Y-, and Z- directions and tilt with respect to X- and Y- axes. Light scattered from the 3D structure was reflected by a second mirror, collected by a second lens and directed to a photodetector (Thorlabs, DET110) for intensity measurements. The fluctuations in the scattering intensity due to the 3D vibrations generated photocurrent in the photodetector with the same overall time dependence. The system was tuned such that the amplitude of the photocurrent responded linearly to the amplitude of the input voltage. Within the operational range of frequency, the amplitude of the fluctuating photocurrent is directly proportional to the vibration amplitude, which peaked at the resonant frequency. A lock-in amplifier (SRS 830, Stanford Research Systems) was used to record the amplitude of the photocurrent.

A Labview program was used to sweep the desired range of frequency and convert data from the lock-in amplifier. At each frequency, the measurement was repeated 64 times to ensure minimum fluctuations, and the increment of frequency was 50 Hz. The error of the system was determined to be ~ 50 Hz.

4.5 Conclusions

This chapter presents various theoretical and experimental results on application of the mechanically-guided 3DFMs, such as the 3D electronic scaffolds for *in vitro* biological studies, the 3D thermoelectric energy harvesters for wearable applications, and the 3D vibratory platforms for nanomechanical sensing. While they are still preliminary prototypes subject to further developments (i.e. scalability and multiple sensor integrations for the 3D electronic scaffolds, replacement with better thermoelectric materials for the 3D thermoelectric energy harvesters, and resolution enhancement and uncertainty minimization for the 3D vibratory platforms), these results represent critical components (structural supports, power solutions and sensors) towards integrated, miniature, multi-functional, highly customizable, and mechanically compliant electronic platforms for the next-generation biomedical research and soft robotics.

4.6 Figures

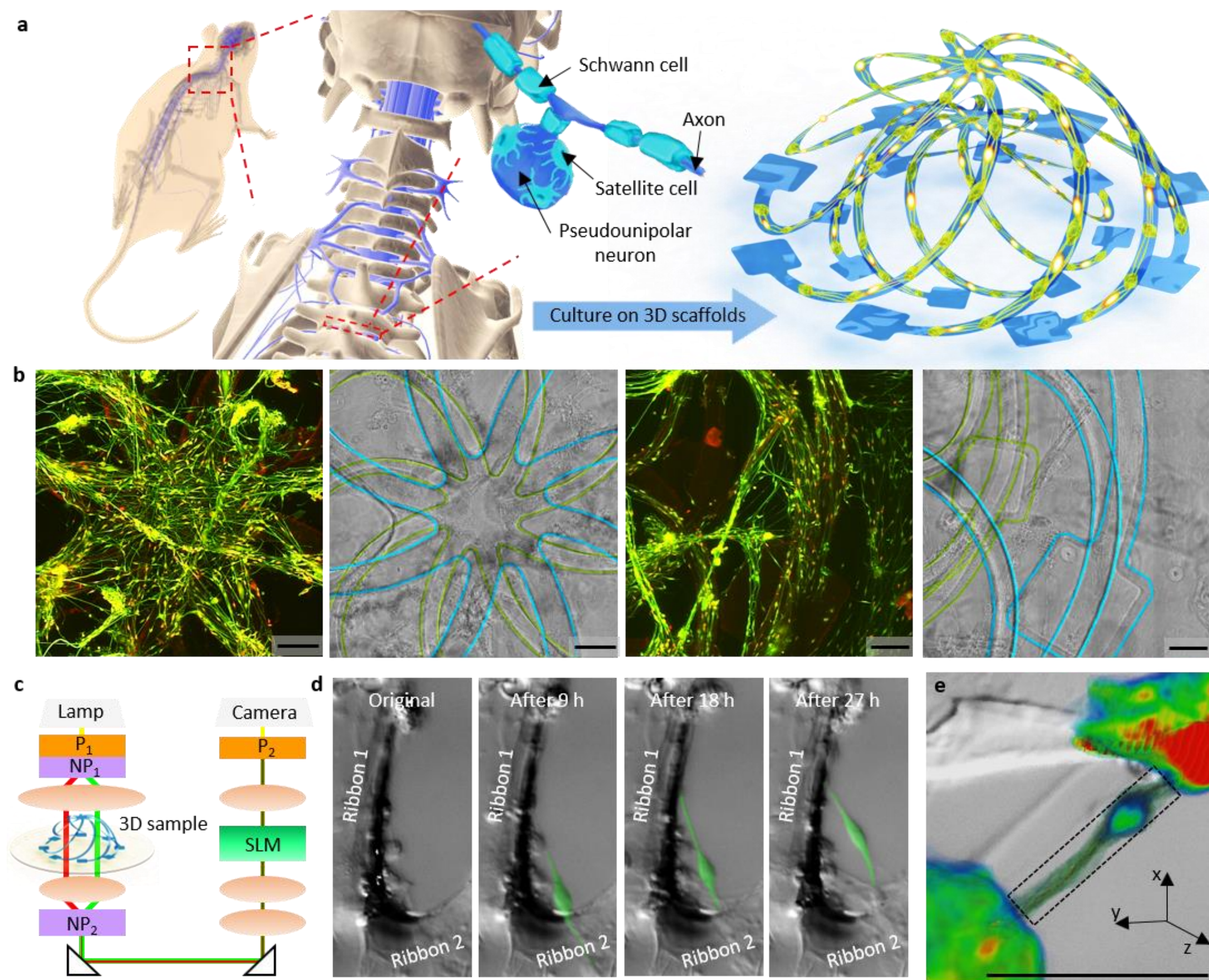

Figure 4.1 3D electronic scaffolds for imaging. (a) Schematic illustration of rat DRG and the cell populations within them (left), as cultured on 3DFMs (right). (b) Confocal fluorescence micrographs immunostained with antiMAP2 (neurons, red), and antiGFAP (glia, green), and corresponding phase-contrast micrographs of DRG cells cultured on a 3D bilayer cage on a glass slide. (c) Schematic illustrate of the setup for GLIM imaging. "P" stands for polarizer and "NP" stands for Nomarski prism. (d) In situ observation of the migration of a DRG cell on a 3D ribbon. (e) Amira 3D rendering of interribbon DRG cell formations observed via GLIM. Scale bars = 100 μm. Reproduced from reference 1.

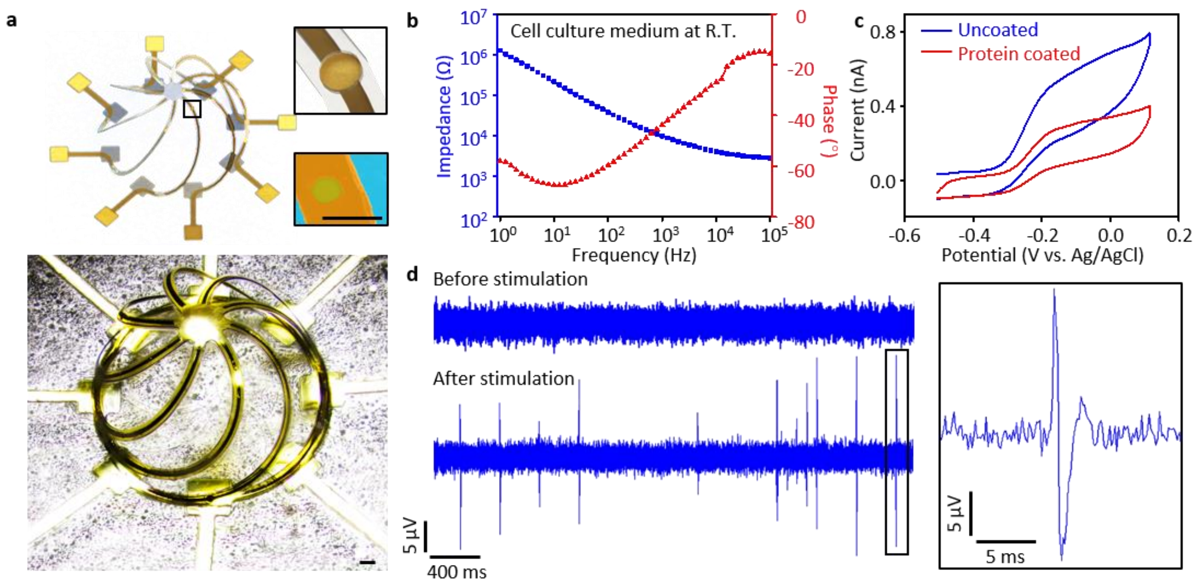

Figure 4.2 3D electronic scaffolds for electrophysiological monitoring. (a) Schematic illustration and optical image of a 3D cage with eight integrated and separately addressable electrodes for stimulation and recording. The insets show schematic illustration and SEM image of a representative electrode. (b) Impedance and phase measurements of these electrodes evaluated in cell culture medium. (c) Ferrocenecarboxylic acid oxidation test of the electrodes before and after protein treatment. (d) Extracellular action potential stimulation and recording of DRG neurons on 3D electrodes: data collected from one 3D electrode before (top left) and after electrical stimulation (bottom left), and magnified view of one spike (right). Scale bars = 100 μm. Reproduced from reference 1.

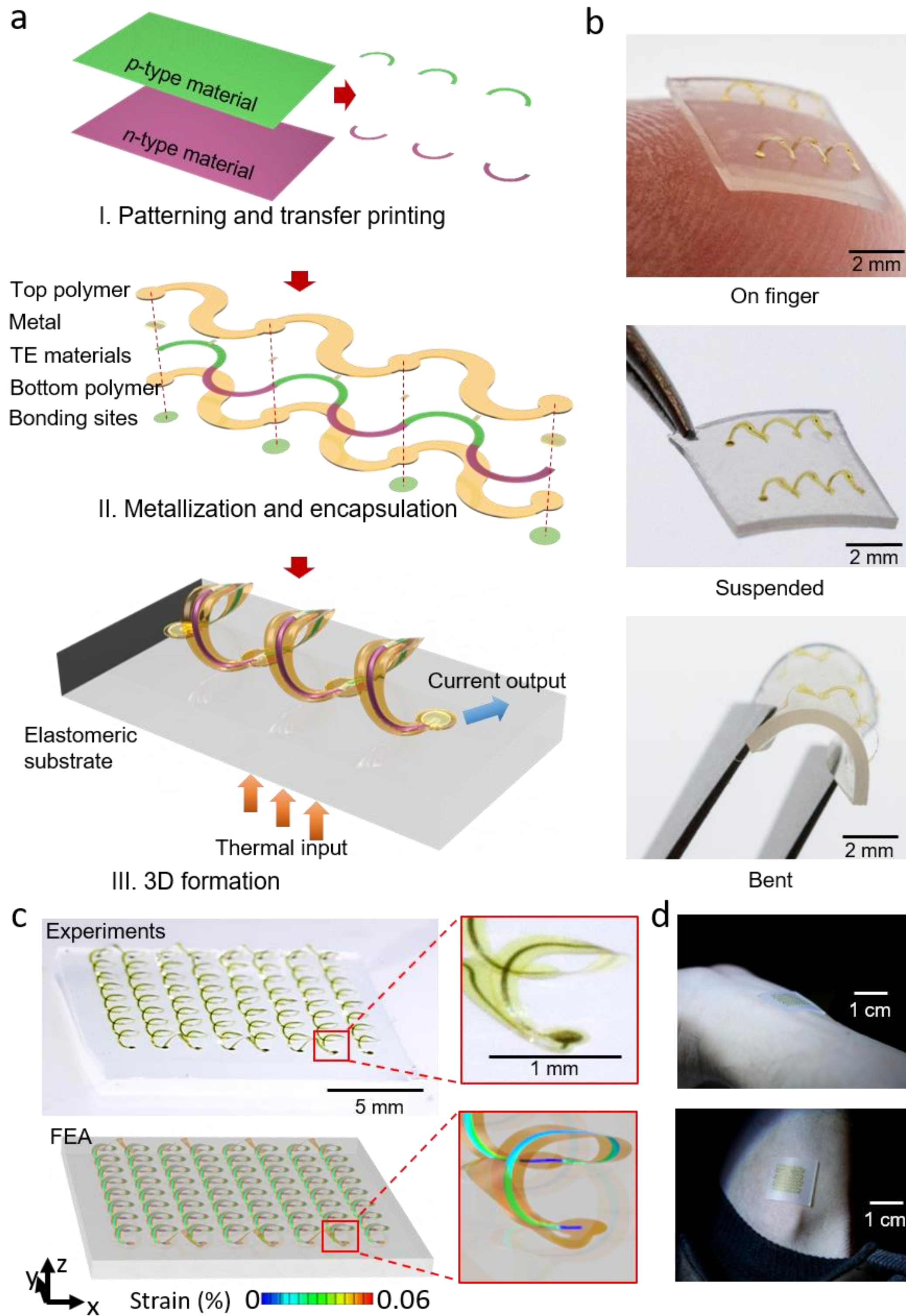

Figure 4.3 3D thermoelectric coils as active components of flexible and deformable systems for harvesting electrical power. (a) Schematic illustration of the process for fabrication and 3D

Figure 4.3 (cont.) assembly. (b) Optical images of the resulting 3D thermoelectric coils. The geometry of the structure and the elastomer substrate combine to provide mechanical robustness against handling and mechanical deformation. (c) Image of an array with 8×8 coils. The magnified view shows that the 3D structure has a geometry consistent with that predicted by finite element analysis. The colored profile represents strain in the silicon leg. (d) The 8×8 array attached to the skin. Reproduced from reference 2.

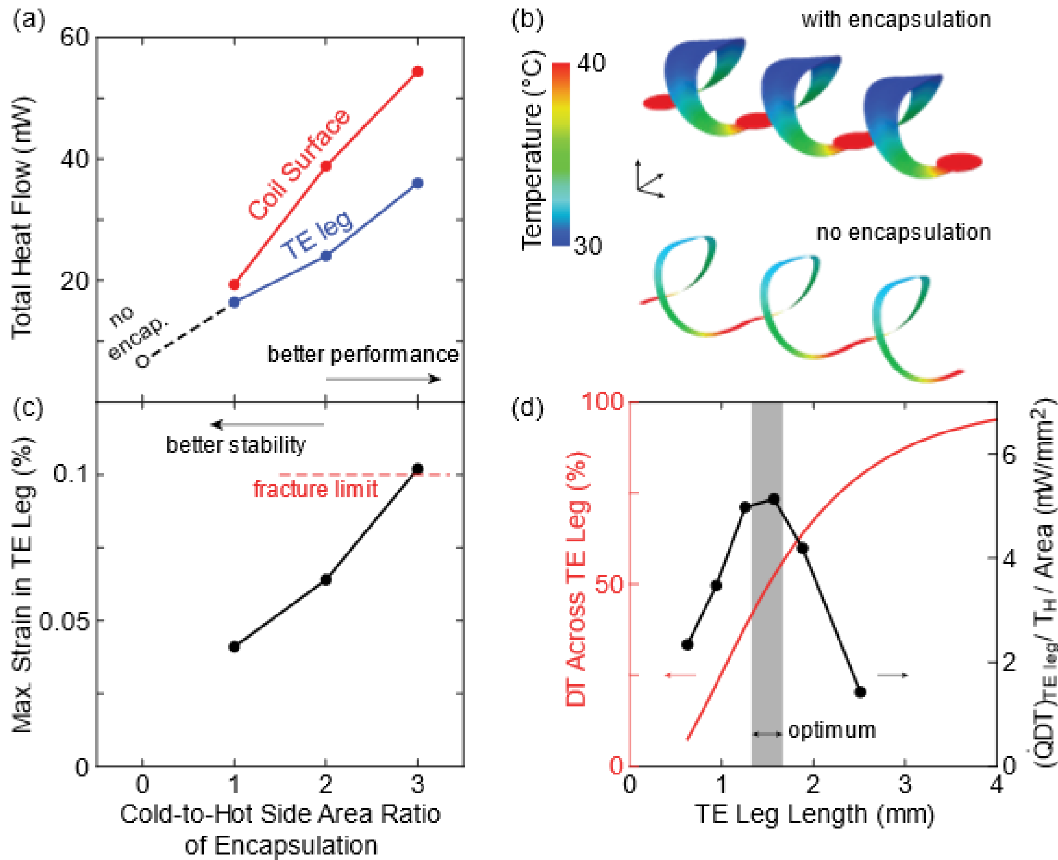

Figure 4.4 Considerations in thermal engineering to optimize choices of design parameters. (a) The total heat flow across the silicon thermoelectric leg (blue) increases as the width of the cold side of the encapsulated polymer layer is increased. (b) Simulated temperature profiles by FEA that compare the encapsulated case (the ratio of the area of the cold to the hot side is two) to the non-encapsulated case with identical geometry. (c) The maximum strain in the thermoelectric leg as a function of the ratio of the area of the cold to the hot side. (d) With an area ratio of two, the leg length is selected to maximize $\Delta T_{\mathrm{TE}}\dot{Q}_{\mathrm{TE}}$ (right axis, normalized to T_{H} and area) which is the impedance matching condition. The corresponding fractional temperature drop across the leg is shown on the left axis. All findings presented here are results of modeling of 3×1 coil structures (three leg-pairs) with a hot-side thermal bath of 40 °C and the entire surface subject to convective heat dissipation due to ambient air at 21 °C. Reproduced from reference 2.

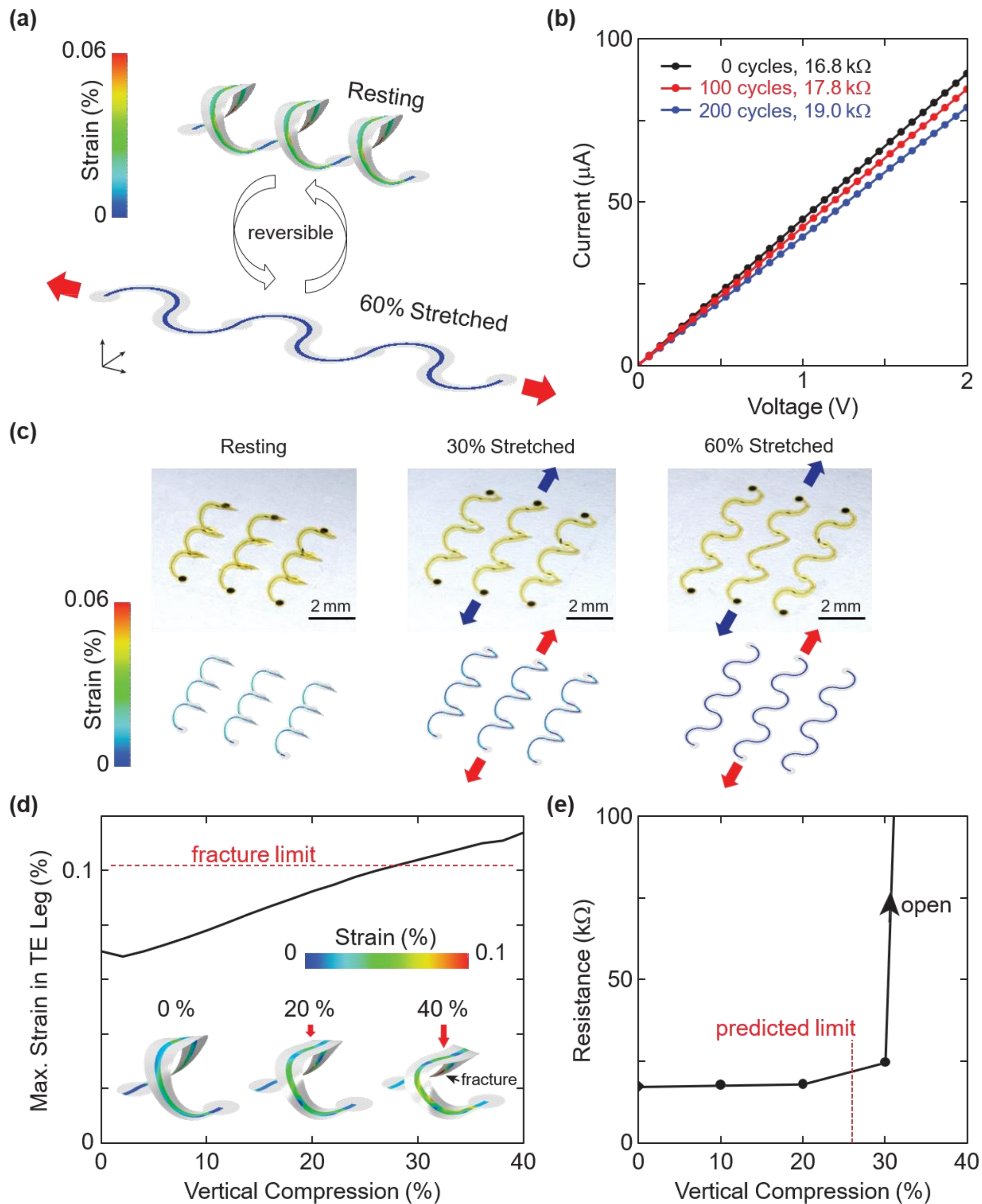

Figure 4.5 Mechanical deformability and durability of 3D thermoelectric coils. (a) Simulated distributions of strain in the silicon thermoelectric leg before and after uniaxial stretching in the plane by 60%. (b) Results of experimental durability tests that involve multiple cycles of 60% uniaxial stretch and release on a 3 × 1 coil structure (strain rate ~ 0.01 s^{-1}). (c) Optical images (top

Figure 4.5 (cont.) row) and simulated structures (bottom row) upon in-plane stretching. (d) Simulated values of the maximum local strain in the thermoelectric leg induced by vertical compression. The inset shows the deformed structure upon compression, including a strain distribution map of the silicon leg. (e) Experimental measurements of the device resistance upon vertical compression. At a compression of 40%, the device shows open-circuit behavior, due to fracture of the silicon. Reproduced from reference 2.

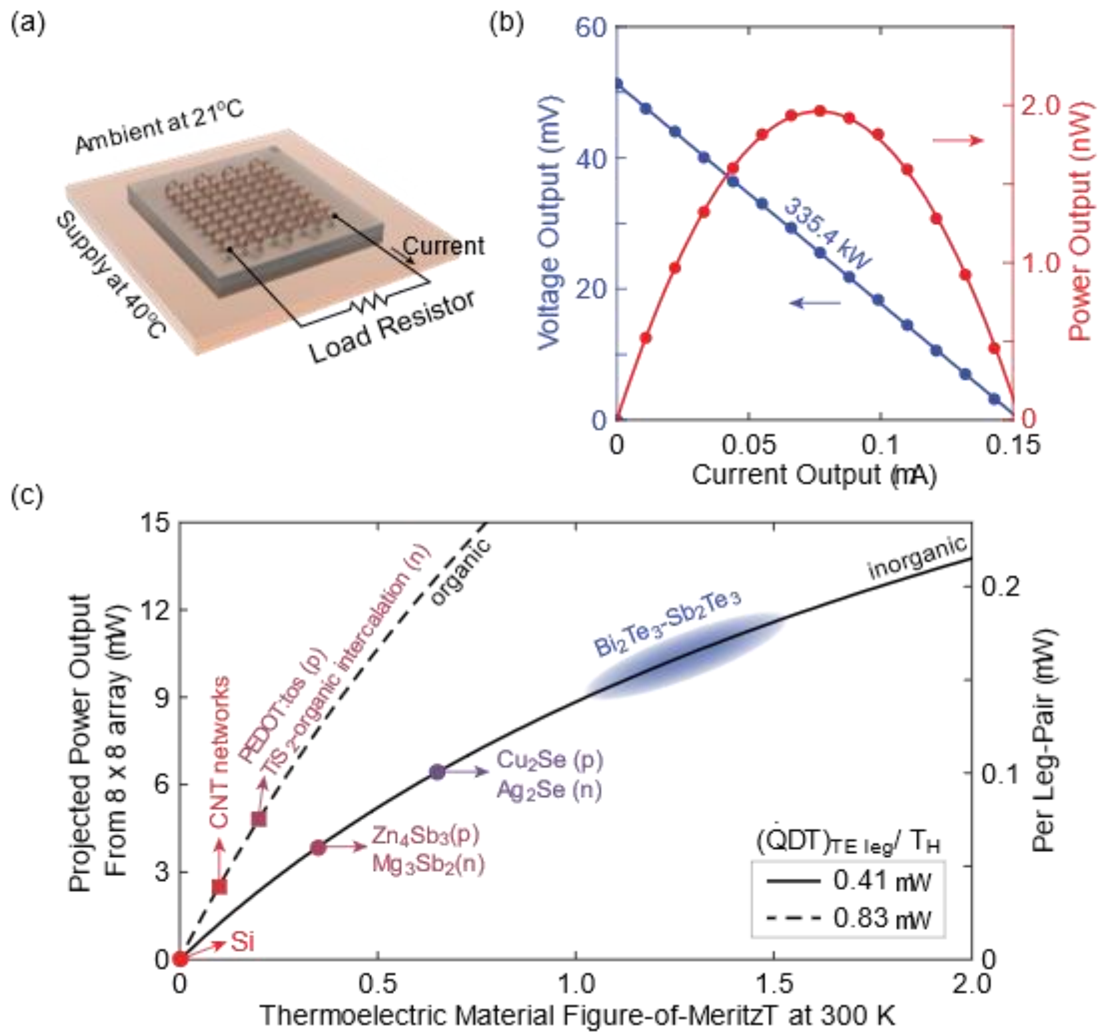

Figure 4.6 Energy harvesting with thermoelectric coils and road map for power enhancement. (a) Schematic illustration of the measurement conditions for evaluating the performance of the harvesting devices. (b) Measured power output characteristics of the 8 × 8 coil array, showing a maximum power of ~2 nW. (c) Projected power output achievable by using known thermoelectric materials with thermoelectric figure-of-merit *zT* higher than that of Si (left axis is for a 8 × 8 array; right axis shows values on a per coil basis). The dashed and solid lines represent the values from structures obtainable with organic and inorganic materials, respectively. Reproduced from reference 2.

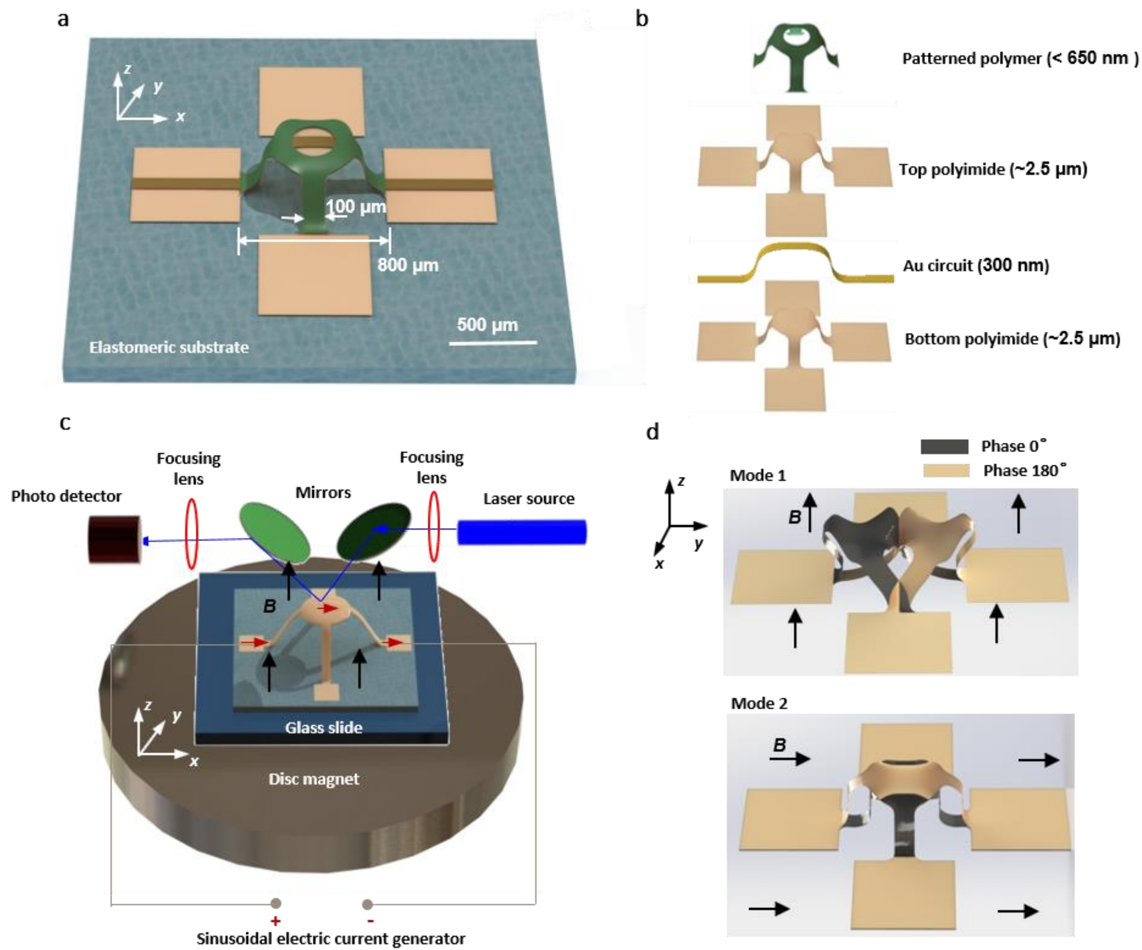

Figure 4.7 3D vibratory platform actuated by Lorentz force. (a) Schematic illustrations of the 3D structure, assembled on an elastomer substrate. (b) Exploded view of the layered composition with integrated conductive traces. (c) Schematic illustration of the measurement system, consisting of a magnet and current source for Lorentz-force actuation and a laser apparatus for detection of vibrational motions. (d) FEA views of the two distinct vibration modes of the vibrator, achieved by placing the permanent magnet at the bottom (top frame) and at the side (bottom frame). The amplitudes of the vibrations are exaggerated for viewing purposes. Reproduced from reference 3.

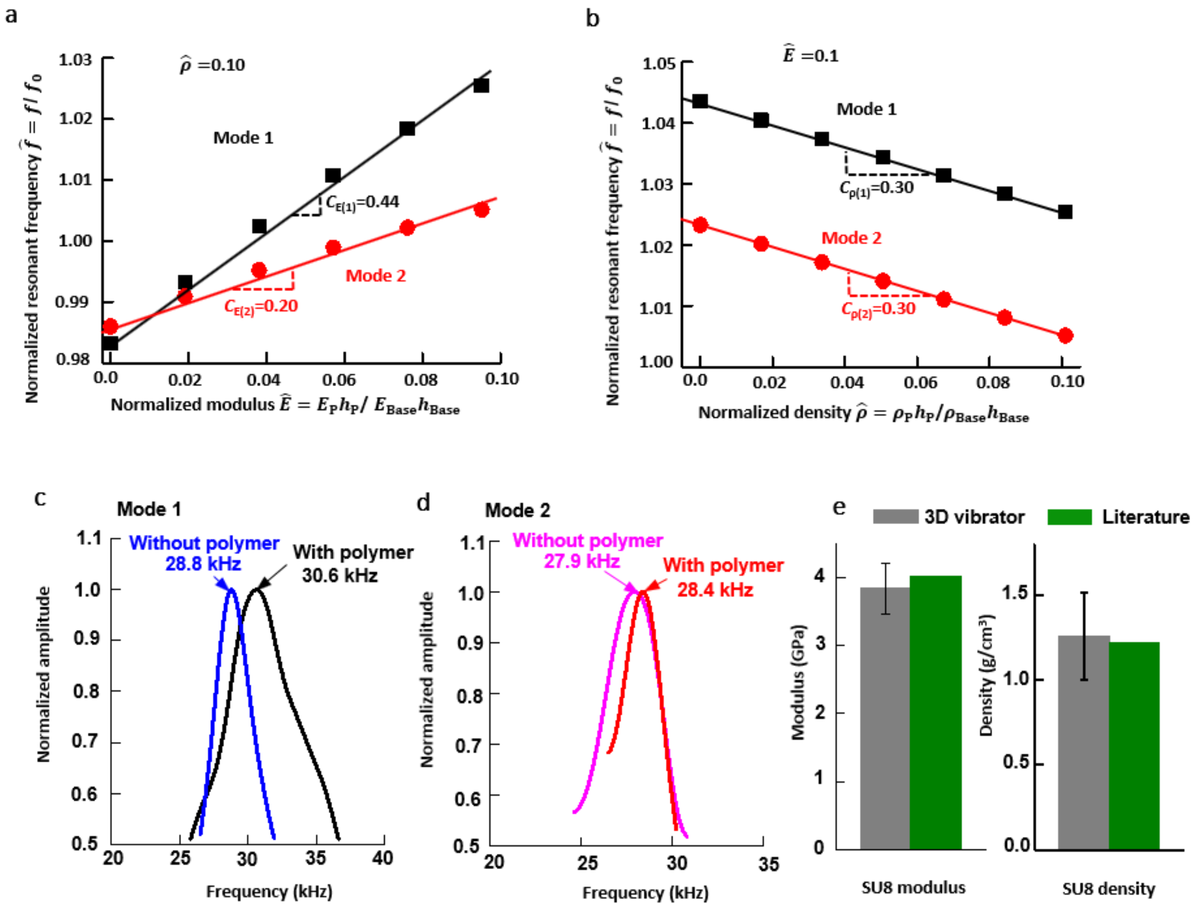

Figure 4.8 Measurement of modulus and density using a single 3D microstructure. (a)-(b) FEA result for variation of the normalized resonant frequency with the normalized modulus (a) and the normalized density (b), for both vibration mode 1 and 2. (c)-(d) Measurement results of the normalized amplitude vs. frequency for mode 1 (c) and mode 2 (d). (e) Modulus (left frame) and density (right frame) determined by the 3D vibratory structure, compared with the literature values. Reproduced from reference 3.

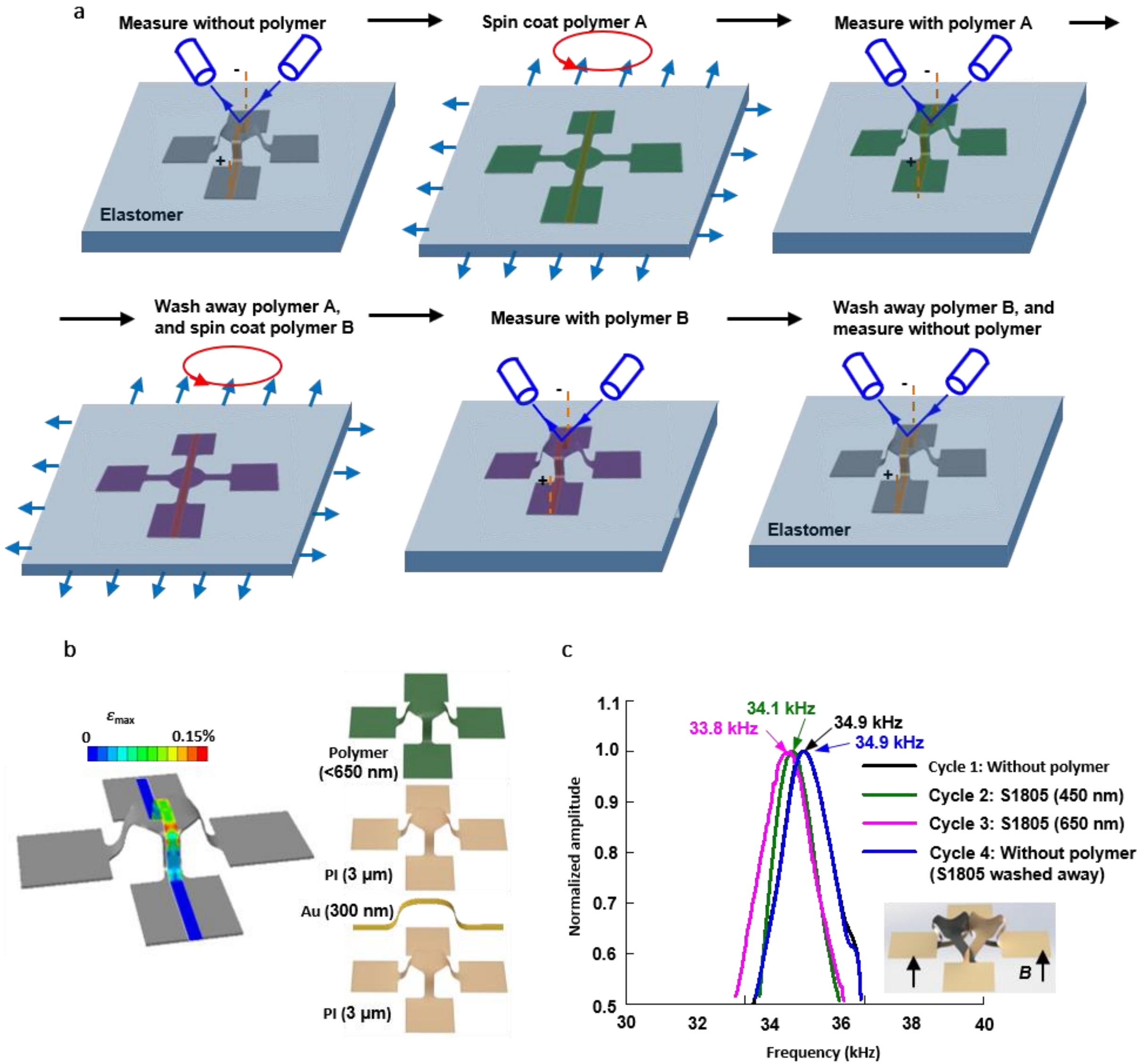

Figure 4.9 Reusability of 3D vibrator. (a) Schematic illustration of repetitive use of the 3D vibrator. (b) Maximum strain in the gold layer obtained by FEA, which is below its yield strain (left frame); Exploded view of the layered composition of the vibratory platform (right frame). (c) FEA views of the vibration mode in this measurement (inset), and a series of measurement results on the same platform using different testing subjects. The amplitudes of the vibrations are exaggerated for viewing purposes. Reproduced from reference 3.

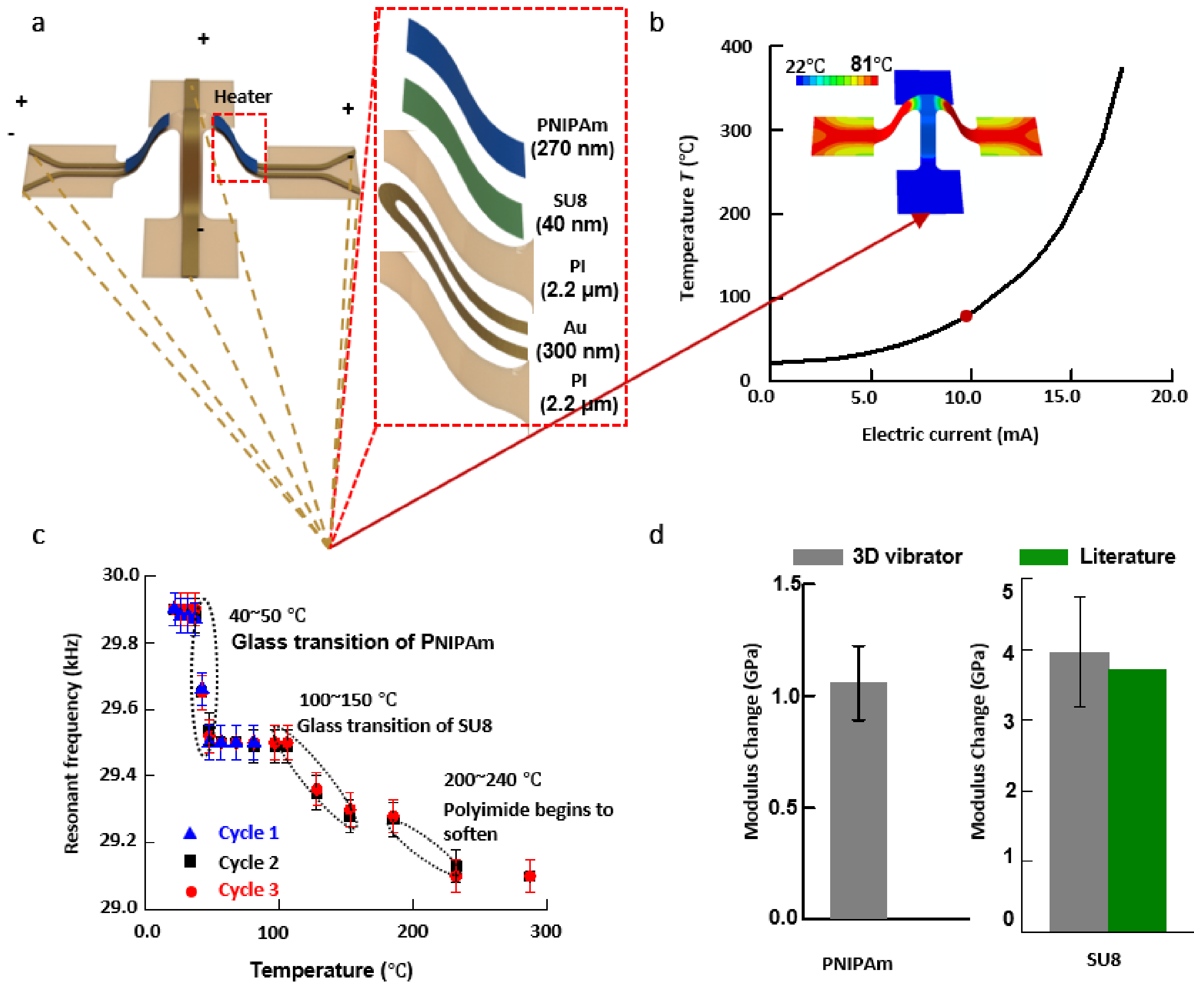

Figure 4.10 3D vibratory platform integrated with thermal actuators. (a) Schematic illustration of the 3D architecture integrated with thermal actuators, circuits for Lorentz force actuation and patterned polymer film (left frame), and magnified, exploded view of the section containing the thermal actuators (right frame). (b) Calibration of temperature vs. supplied electric current. (c) Experimental results for the variation of the resonant frequency with temperature. (d) Change in modulus of PNIPAm (left frame) and SU8 (right frame) determined from the results in (c). Reproduced from reference 3.

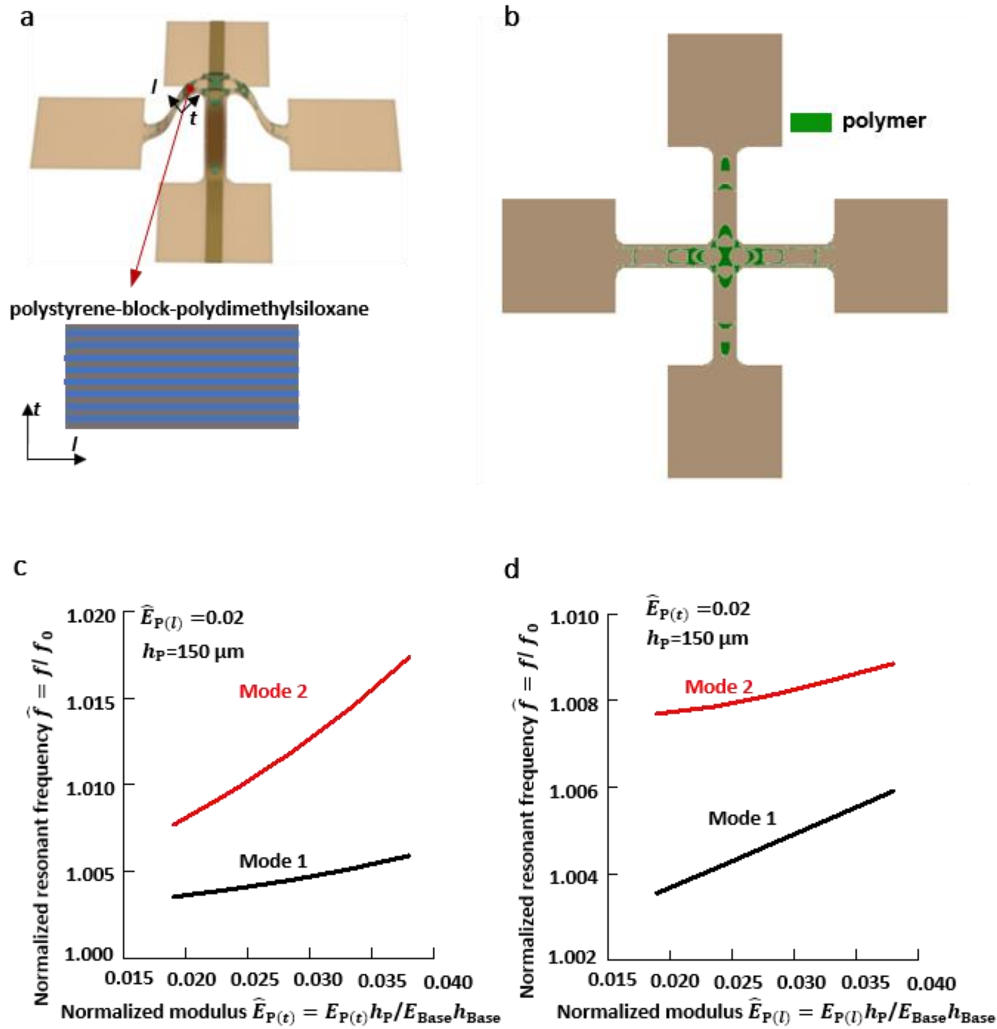

Figure 4.11 Theoretical investigation of measurement of anisotropic elastic moduli using a 3D vibratory platform. (a) Schematic illustration of the 3D vibratory platform with a thin film that has anisotropic elastic moduli. In this case, the thin film has different elastic moduli along the transverse (*t*) and longitudinal (*l*) directions. (b) Optimized polymer patterns according to the optimization algorithm. (c)-(d) FEA results of normalized resonant frequency for mode 1 and mode 2 with normalized modulus in transverse (*t*) (c) and longitudinal (*l*) (d) directions, respectively. Reproduced from reference 3.

4.7 References

1. Yan, Zheng, et al. "Three-dimensional mesostructures as high-temperature growth templates, electronic cellular scaffolds, and self-propelled microrobots." Proceedings of the National Academy of Sciences 114.45 (2017): E9455-E9464.

2. Nan, Kewang, et al. “Compliant and stretchable thermoelectric coils for energy harvesting in miniature flexible devices” Science Advances 4.11 (2018): eaau5849.

3. Nan, Kewang, et al. “Soft 3D microscale vibratory platforms for characterization of nano-thin polymer films.” ACS Nano (2018): 10.1021/acsnano.8b06736.

4. Tian, Bozhi, et al. "Macroporous nanowire nanoelectronic scaffolds for synthetic tissues." Nature materials 11.11 (2012): 986.

5. Xie, Chong, et al. "Intracellular recording of action potentials by nanopillar electroporation." Nature nanotechnology 7.3 (2012): 185.

6. Lind, Johan U., et al. "Instrumented cardiac microphysiological devices via multimaterial three-dimensional printing." Nature materials 16.3 (2017): 303.

7. Feirabend, H. K. P., and E. Marani. "Dorsal root ganglion." (2003): 28-33.

8. White, Norman M., and Robert J. McDonald. "Multiple parallel memory systems in the brain of the rat." Neurobiology of learning and memory 77.2 (2002): 125-184.

9. Badea, Adina, et al. "3D-printed pHEMA materials for topographical and biochemical modulation of dorsal root ganglion cell response." ACS applied materials & interfaces 9.36 (2017): 30318-30328.

10. Nguyen, Tan H., et al. "Gradient light interference microscopy for 3D imaging of unlabeled specimens." Nature communications 8.1 (2017): 210.

11. Ravula, Surendra K., et al. "A multielectrode microcompartment culture platform for studying signal transduction in the nervous system." Lab on a Chip 6.12 (2006): 1530-1536.

12. Tsai, Hsing-Chen, et al. "Phasic firing in dopaminergic neurons is sufficient for behavioral conditioning." Science 324.5930 (2009): 1080-1084.

13. Vedde, Jan, and Peter Gravesen. "The fracture strength of nitrogen doped silicon wafers." Materials Science Science and Engineering B-Solid State Materials for Advanced Technology: l996 36.1-3 (1996): 246-250.

14. Snyder, G. Jeffrey. "Thermoelectric energy harvesting." Energy Harvesting Technologies. Springer, Boston, MA, 2009. 325-336.

15. Baranowski, Lauryn L., G. Jeffrey Snyder, and Eric S. Toberer. "Effective thermal conductivity in thermoelectric materials." Journal of Applied Physics 113.20 (2013): 204904.

16. Kim, Sun Jin, Ju Hyung We, and Byung Jin Cho. "A wearable thermoelectric generator fabricated on a glass fabric." Energy & Environmental Science 7.6 (2014): 1959-1965.

17. Snyder, G. Jeffrey, et al. "Thermoelectric microdevice fabricated by a MEMS-like electrochemical process." Nature materials 2.8 (2003): 528.

18. Pelz, U., et al. "Fabrication Process for Micro Thermoelectric Generators (μTEGs)." Journal of Electronic Materials 45.3 (2016): 1502-1507.

19. Weber, J., et al. "Coin-size coiled-up polymer foil thermoelectric power generator for wearable electronics." Sensors and Actuators A: Physical 132.1 (2006): 325-330.

20. Suarez, Francisco, et al. "Flexible thermoelectric generator using bulk legs and liquid metal interconnects for wearable electronics." Applied energy 202 (2017): 736-745.

21. Wang, Ziyang, et al. "Realization of a wearable miniaturized thermoelectric generator for human body applications." Sensors and Actuators A: Physical 156.1 (2009): 95-102.

22. Kim, S. S., S. Yamamoto, and T. Aizawa. "Thermoelectric properties of anisotropy-controlled p-type Bi–Te–Sb system via bulk mechanical alloying and shear extrusion." Journal of alloys and compounds 375.1-2 (2004): 107-113.

23. Ueno, K., et al. "Optimization of hot-press conditions of Zn4Sb3 for high thermoelectric performance. II. Mechanical properties." Journal of alloys and compounds 388.1 (2005): 118-121.

24. Tyagi, Kriti, et al. "Crystal structure and mechanical properties of spark plasma sintered Cu2Se: An efficient photovoltaic and thermoelectric material." Solid State Communications 207 (2015): 21-25.

25. Yan, Zheng, et al. "Mechanical assembly of complex, 3D mesostructures from releasable multilayers of advanced materials." Science advances 2.9 (2016): e1601014.

26. Iwanaga, Shiho, and G. Jeffrey Snyder. "Scanning Seebeck coefficient measurement system for homogeneity characterization of bulk and thin-film thermoelectric materials." Journal of electronic materials 41.6 (2012): 1667-1674.

27. Chung, Soonwan, and Seungbae Park. "Effects of temperature on mechanical properties of SU-8 photoresist material." Journal of Mechanical Science and Technology 27.9 (2013): 2701-2707.

28. Biswas, Chandra Sekhar, et al. "Effects of tacticity and molecular weight of poly (N-isopropylacrylamide) on its glass transition temperature." Macromolecules 44.14 (2011): 5822-5824.

29. Keddie, Joseph L., Richard AL Jones, and Rachel A. Cory. "Size-dependent depression of the glass transition temperature in polymer films." EPL (Europhysics Letters) 27.1 (1994): 59.

30. Feng, R., and R. J. Farris. "The characterization of thermal and elastic constants for an epoxy photoresist SU8 coating." Journal of materials science 37.22 (2002): 4793-4799.

31. Kujawa, Piotr, and Françoise M. Winnik. "Volumetric studies of aqueous polymer solutions using pressure perturbation calorimetry: A new look at the temperature-induced phase transition of poly (N-isopropylacrylamide) in water and D2O." Macromolecules 34.12 (2001): 4130-4135.

32. Antipov, Yuri V., and Yakov S. Vygodskii. "Polymers on the Basis of Epoxy Oligomers and Polyimideis." MICC 90. Springer, Dordrecht, 1991. 679-684.

33. Ye, Changhuai, et al. "Anisotropic mechanical properties of aligned polystyrene-block-polydimethylsiloxane thin films." Macromolecules 46.21 (2013): 8608-8615.

34. Xue, Changying, et al. "Protein adsorption on poly (N-isopropylacrylamide) brushes: dependence on grafting density and chain collapse." Langmuir 27.14 (2011): 8810-8818.

CHAPTER 5

CONCLUSIONS AND OUTLOOK

This thesis presents a novel approach to 3D functional mesostructures (3DFMs) via deterministic mechanical buckling of 2D thin-film precursors, using compressive forces supplied by relaxation of pre-stretched elastomeric substrates. Fabrications of the 2D precursors are fully compatible with state-of-the-art planar technologies such as photolithography and laser cutting, resulting in large degrees of freedom in terms of geometries, materials, and architectures. Specifically, 3DFMs made of materials ranging from electronic-grade semiconductors (mono-crystalline silicon), to high-performance metals (gold, copper), and to photo-patternable epoxies (SU8, polyimide), with overall dimensions ranging from tens of microns to several millimeters, with geometries and architectures ranging from kirigami/origami (Chapter 2.2), to multilayers (Chapter 2.3), to locally-tunable structures (Chapter 2.4), to shape-shifting structures (Chapter 3.2), and to freestanding structures (Chapter 3.3), have been demonstrated. Throughout the thesis, we have shown the importance of finite element analysis (FEA) in geometric designs and mechanical predictions to greatly facilitate the experiments.

This new technology enables exciting device opportunities in many engineering fields that are otherwise difficult to realize through conventional 3D techniques. In this thesis, we have successfully demonstrated the applications of 3DFMs as soft, stretchable and tunable 3D functional devices in passive electronics (radiofrequency [RF] devices and antennas, Chapters 2.3.2, 2.4.2 and 3.2.4), active electronics (3D light-emitting diodes [LEDs] and transistor arrays, Chapter 3.2.1), robotics (shape-shifting electronics and micro swimmers, Chapters 3.2 and 3.4), biology (3D cellular scaffolds, Chapter 4.2), energy harvesting (3D thermoelectric harvesters, Chapter 4.3), and nanomechanical sensing (3D vibratory platforms, Chapter 4.4). These examples

represent but a glimpse of many other engineering implications by the mechanically-guided 3D assembly.

Moving forward, an important next step is to integrate smart and functional materials to realize additional degrees of control over the 3D geometries and architectures beyond the mechanical forces supplied by the elastomeric substrates. Promising candidates include shape-memory polymers and alloys actuated by thermal variations, ionic polymers actuated by electric fields, ferromagnetic materials actuated by magnetic fields, and cellular composite materials actuated by solvent swelling/deswelling. Several interesting applications can be envisioned with such advances in materials and designs, including microscale sensing, robotics, and energy conversions.

With the advances in fabrication techniques and materials selections, we might one day see the realization of 3D microelectronics capable of seamless integrations with cells and tissues, as depicted in Figure 1.1. Some preliminary work has been demonstrated in Chapter 4.2. Future research directions include further device shrinkage and upgrades to include the wireless powering and data transmissions, the multifunctional sensing and the ability to stimulation (thermal, electrical, mechanical etc.) and therapy (drug delivery).

APPENDIX A: DESIGN AND MECHANICS OF MORPHABLE 3D MESOSTRUCTURES

A. 1 Scaling Law for the Strain Energy Barrier

The ribbon structure shown in Figure 3.2a is characterized by five geometrical parameters, i.e., w_{narrow}, w_{wide}, l_{narrow}, l_{wide}, and t. Here, l, w and t are the length, width and thickness of the two constituent ribbons, respectively. The subscripts 'narrow' and 'wide' denote the creases and other regions, respectively. During its compressive buckling process, the strain energy barrier discussed in Figure 3.2b plays an important role in the shape shifting. This strain energy barrier can be normalized as $\bar{E}_{barrier} = E_{barrier} * \frac{S}{l}$, where S denotes the out-of-plane bending stiffness of the wide regions, $l = 4(l_{\text{narrow}} + l_{\text{wide}})$ is the lateral dimension of 2D precursor. In general, the normalized strain energy barrier depends on the prestrain (ε_{pre}), and can be expressed as:

$$\bar{E}_{barrier} = F\left({}^{w_{\text{narrow}}}/_{w_{\text{wide}}}, {}^{l_{\text{narrow}}}/_{l_{\text{wide}}}, {}^{t}/_{w_{\text{wide}}}, {}^{w_{\text{wide}}}/_{l_{\text{wide}}}, \varepsilon_{\text{pre}}\right) \tag{2}$$

Where F is a dimensionless function of the width ratio, length ratio, thickness to width ratio, width to length ratio and prestrain.

Due to a large curvature in narrow segments, shape II typically corresponds to a larger strain energy than shape I after release (Figure 3.2c, $E_{diff} > 0$), such that it would switch into shape I for a vanishing energy barrier. Thereby, we focus on the energy barrier for shape II herein ($E_{barrier} = E_{peak} - E_{initial}$, $E_{initial} = E_{II}$), i.e., the energy barrier during sequential release. According to FEA results (Figure A1a-b) of ribbon structures with a wide range of geometric parameters, the normalized strain energy barrier is almost independent on the thickness to width ratio (t/w_{wide}) and width to length ratio (w_{wide}/l_{wide}) after sequential release, because of the deformations that are localized at the narrow segments. Since the bending curvature scales with the square root of the compressive strain ($\varepsilon_{compr} = \varepsilon_{pre} / (1 + \varepsilon_{pre})$, with $\varepsilon_{pre} = \varepsilon_{x\text{-}pre} = \varepsilon_{y\text{-}pre}$) applied to the ribbon, it can be

deduced that the function F is linearly proportional to the compressive strain, such that Equation (S1) can be simplified as:

$$\bar{E}_{barrier} = H\left({}^{w_{\text{narrow}}}/_{w_{\text{wide}}}, {}^{l_{\text{narrow}}}/_{l_{\text{wide}}}\right)\left(\frac{\varepsilon_{pre}}{1+\varepsilon_{pre}}\right) \quad (3)$$

Such proportional dependence agrees well with FEA results for all of the cases studied herein, as shown in Figure A1c. The function H in Equation (S2) denotes the coefficient of proportionality between F and ε_{compr}, which depends on the width ratio (w_{narrow}/w_{wide}) and length ratio (l_{narrow}/l_{wide}) (Figure A1d-e). By increasing the width ratio for a fixed length ratio (0.15), H decreases and becomes zero when $w_{narrow}/w_{wide} > 0.79$. This suggests that the designs with $w_{narrow}/w_{wide} > 0.79$ and $l_{narrow}/l_{wide} = 0.15$ give the same configuration for simultaneous and sequential release, due to the vanishing energy barrier. It also can be observed from Figure A1e that the 2D precursor can achieve a unique shape when $w_{narrow}/w_{wide} = 0.25$ and $l_{narrow}/l_{wide} < 0.04$.

A. 2 Design Process for 2D Precursors with Multiple Buckling Modes

For an initial design shown in Figure A2, simulations of the processes of simultaneous and sequential release allow assessments of reconfigurability. If the design fails to exhibit multiple modes, then creases are added to different groups of ribbon components until reconfigurability is achieved. For any ribbon group (e.g., group *n* with ribbons ①②③), creases are added to the end and the middle of each ribbon, the process of simultaneous release is simulated, and then displacement loads are applied to all the intersections of group-*n* ribbons in the as-formed 3D geometry. If another stable configuration is obtained after unloading the displacement, the process of sequential release is simulated to determine whether the updated 2D precursor with creases indeed reconfigures into the new mode. Otherwise, these procedures are repeated for the next

possible ribbon groups until the new buckling modes are identified. The overall procedure is summarized in a flow chart in Figure A3.

A. 3 Appendix Figures

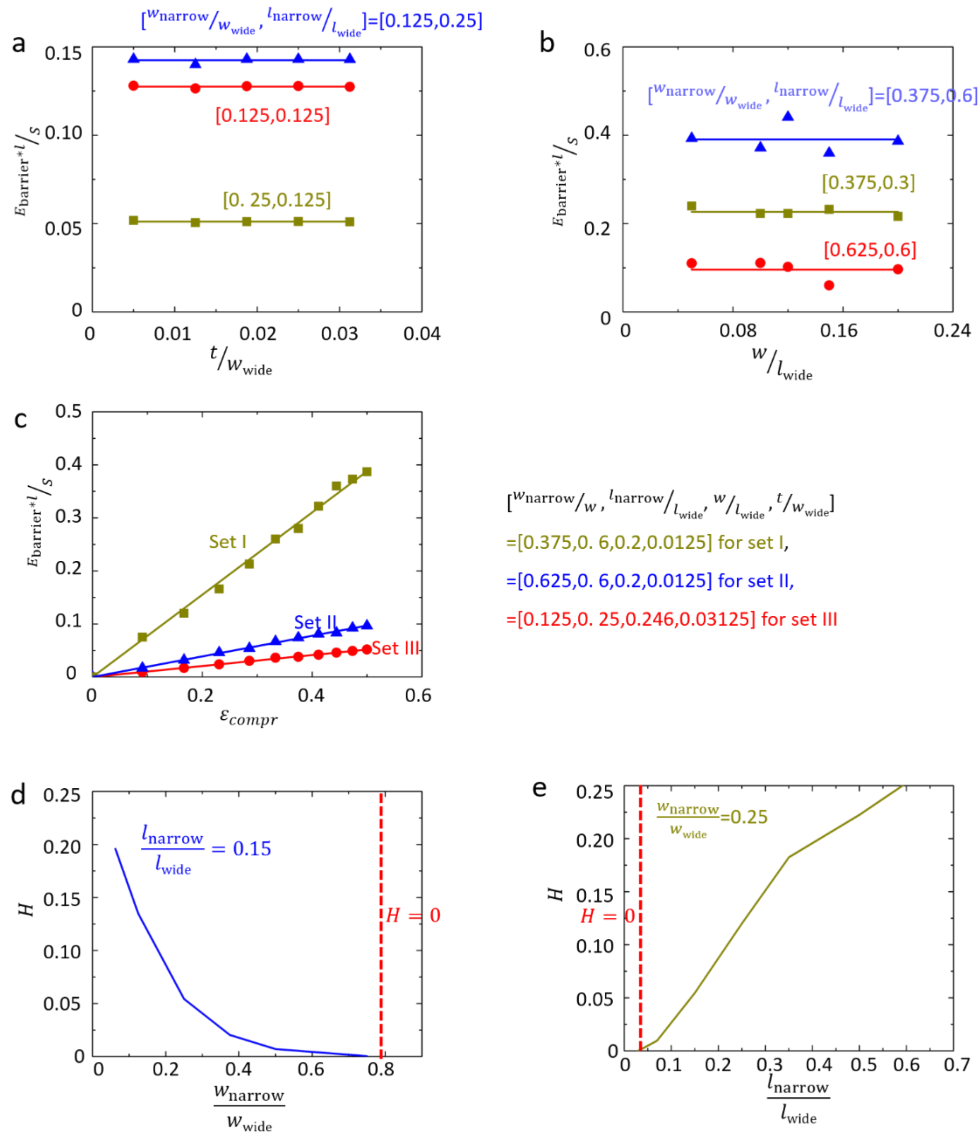

Figure A1 Parametric study of the energy barrier for the pure straight ribbon structure after sequential release. (a), (b) Normalized strain energy barrier as a function of thickness to width ratio (a) and width to length ratio (b), for different crease width ratio and crease length ratio. (c) The normalized strain energy barrier versus thickness to compressive strain, for different crease width ratio, crease length, thickness to width ratio and width to length ratio. (d), (e) Function *H* as a function of crease width ratio (d) and crease length ratio (e).

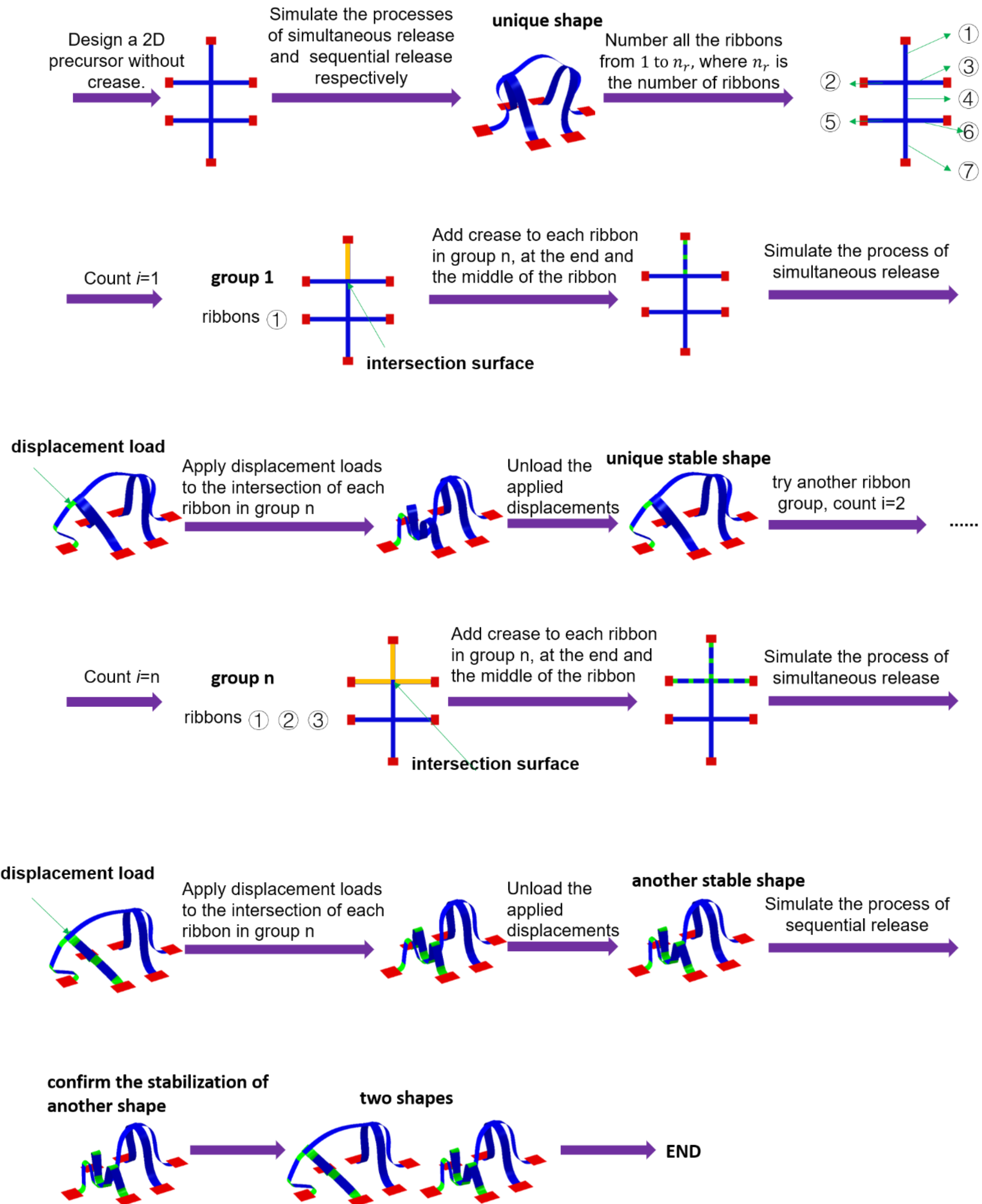

Figure A2 Example of the design process for a 2D precursor capable of shape transformations.

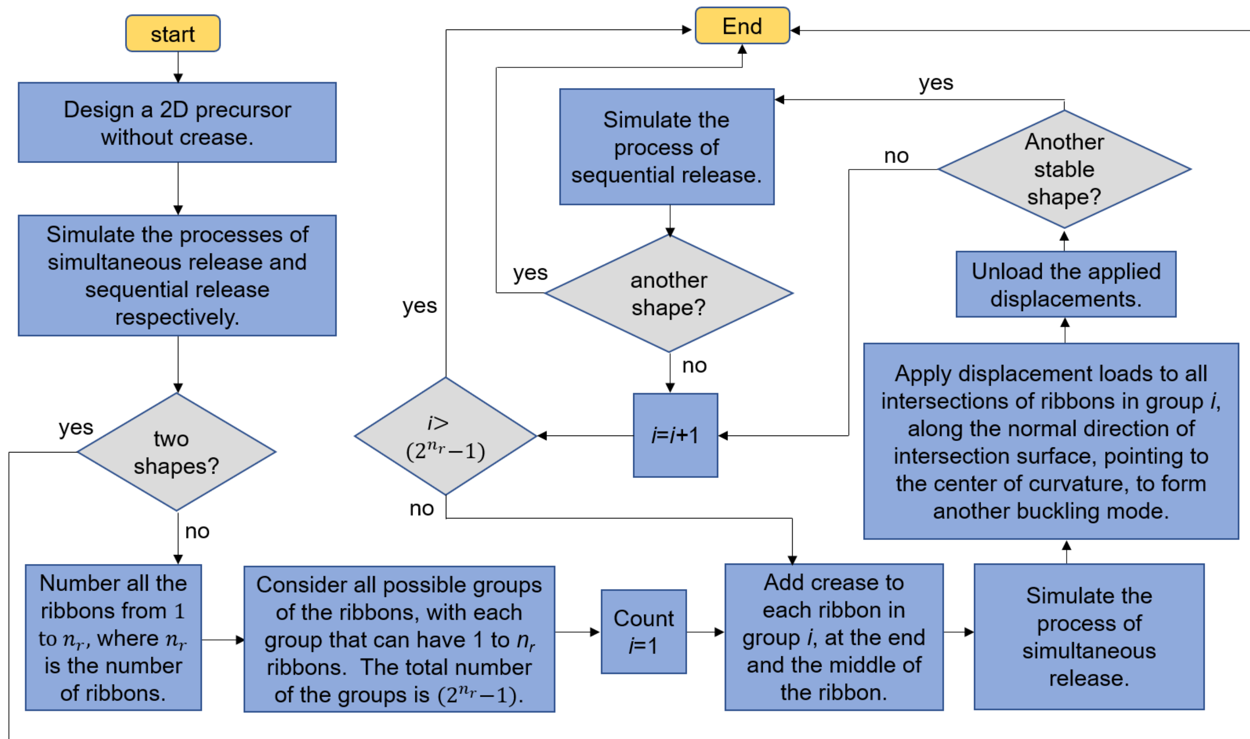

Figure A3 Flow diagram of the design process outlined in Figure A2.

APPENDIX B: POWER OPTIMIZATION IN THERMOELECTRIC HARVESTERS

B. 1 Power Output from a Thermoelectric Harvester

Thermoelectric devices convert heat into electrical power with an efficiency η. The generated power *P* from a heat flow through a thermoelectric material $\dot{Q}_{\mathrm{TE}}$ is:

$$P = \eta \dot{Q}_{\mathrm{TE}} \tag{4}$$

The conversion efficiency is:

$$\eta = \frac{\Delta T_{\mathrm{TE}}}{T_{\mathrm{H}}} \frac{\sqrt{1+ZT}-1}{\sqrt{1+ZT}+1+\frac{\Delta T_{\mathrm{TE}}}{T_{\mathrm{H}}}} \tag{5}$$

Here, T_{H} is the temperature at the hot side of the thermoelectric material and ΔT_{TE} is the temperature drop across the thermoelectric material that drives $\dot{Q}_{\mathrm{TE}}$. Notice the Carnot efficiency $\eta_{\mathrm{C}} = \frac{\Delta T_{\mathrm{TE}}}{T_{\mathrm{H}}}$ appearing in the equation. *ZT* is the device figure-of-merit employed in device modeling, which is different than the material figure-of-merit *zT*. In the harvester, this distinction can be avoided by simplifying Eq.S2. The "harvesting limit" is characterized by $\Delta T_{\mathrm{TE}} \to 0$, in which we can replace *ZT* with *zT*. In addition, $\eta_{\mathrm{c}} \ll (\sqrt{1+ZT}+1)$ allows for further simplification. The conversion efficiency reduces to a much simpler form:

$$\eta = \frac{\Delta T_{\mathrm{TE}}}{T_{\mathrm{H}}} \frac{\sqrt{1+ZT}-1}{\sqrt{1+ZT}+1} = \frac{\Delta T_{\mathrm{TE}}}{T_{\mathrm{H}}} \eta_0(zT) \tag{6}$$

η_0 is an irresistibility factor that determines the conversion efficiency relative to η_{c}, and is a function of only *zT* in the harvesting limit. The harvested power can now be expressed as:

$$P = \frac{\eta_0(zT)}{T_{\mathrm{H}}} \Delta T_{\mathrm{TE}} \dot{Q}_{\mathrm{TE}} \tag{7}$$

It is seen that, for a given thermoelectric material, the harvested power is proportional to $\Delta T_{\mathrm{TE}} \dot{Q}_{\mathrm{TE}} / T_{\mathrm{H}}$, a factor that is determined by the heat exchange characteristics of the harvester. It could also be thought of as the maximum energy available for conversion.

B. 2 Thermal Impedance Matching Condition

The thermal impedance matching concept originates from the design situation where $\Delta T_{\mathrm{TE}}\dot{Q}_{\mathrm{TE}}$ (which determines power; Eq.S4) becomes maximum when the thermal impedance of the thermoelectric leg Θ_{TE} is at an optimum value; increasing Θ_{TE} increases ΔT_{TE} but decreases $\dot{Q}_{\mathrm{TE}}$, creating an optimum point.

In a conventional generator geometry, thermal impedance of the thermoelectric leg can be controlled independently from that of the heat exchangers (Θ_{ex} combining both hot and cold sides). For a given temperature difference between the heat source and environment ΔT_{Envi},

$$\dot{Q}_{\mathrm{TE}} = \frac{\Delta T_{\mathrm{Envi}}}{\Theta_{\mathrm{ex}}+\Theta_{\mathrm{TE}}} \tag{8}$$

and

$$\Delta T_{\mathrm{TE}} = \Delta T_{\mathrm{Envi}} \frac{\Theta_{\mathrm{TE}}}{\Theta_{\mathrm{ex}}+\Theta_{\mathrm{TE}}} \tag{9}$$

where zero parasitic heat was assumed. It is seen that $\Delta T_{\mathrm{TE}}\dot{Q}_{\mathrm{TE}}$ is maximized when $\Theta_{\mathrm{ex}} = \Theta_{\mathrm{TE}}$ (or, equivalently $\Delta T_{\mathrm{TE}} = \frac{1}{2}\Delta T_{\mathrm{Envi}}$). This condition is referred to as the *thermal impedance matching condition* for thermoelectrics. In practice, $\Theta_{\mathrm{ex}} \approx \Theta_{\mathrm{TE}}$ rather than an equality mostly because of the additional heat transport by Peltier currents.

B. 3 Thermal Impedance Matching in Coil Harvesters

In the coil harvester, the impedance matching condition is more complex because Θ_{ex} and Θ_{TE} are not controllable independently. Scaling the leg length, which is the primary means of controlling Θ_{TE}, also changes Θ_{TE} because the occupied area of the coil changes (which enlarges the coil surface area). Therefore, one must maximize the areal power density.

APPENDIX C: 3D VIBRATORS FOR MECHANICAL CHARACTERIZATION OF NANO-THIN FILMS

C. 1 Scaling Law in Eq. (1), Section 4.4.2

As a first step, a scaling law was derived via dimensional analysis for the resonant frequency when a thin layer of polymer is deposited homogeneously on a PI base layer (modulus-- E_{PI}, density-- ρ_{PI} and thickness h_{PI}). For a vibration mode dominated by bending deformation, the resonant frequency is

$$f = \alpha\sqrt{\frac{K}{M}} \tag{10}$$

where the bending stiffness

$$K = \frac{E_{\mathrm{PI}}^2 h_{\mathrm{PI}}^4 + 4E_{\mathrm{PI}}E_{\mathrm{P}}h_{\mathrm{PI}}^3 h_{\mathrm{P}} + 6E_{\mathrm{PI}}E_{\mathrm{P}}h_{\mathrm{PI}}^2 h_{\mathrm{P}}^2 + 4E_{\mathrm{PI}}E_{\mathrm{P}}h_{\mathrm{PI}}h_{\mathrm{P}}^3 + E_{\mathrm{P}}^2 h_{\mathrm{P}}^4}{12\left(E_{\mathrm{PI}}h_{\mathrm{PI}} + E_{\mathrm{P}}h_{\mathrm{P}}\right)L^2} \tag{11}$$

the mass

$$M = \left(\rho_{\mathrm{P}}h_{\mathrm{P}} + \rho_{\mathrm{PI}}h_{\mathrm{PI}}\right)L^2 \tag{12}$$

and L is the in-plane size of the structure. Considering that the polymer thickness (h_{P}) is much smaller than the PI thickness, the ratio of the resonant frequency with/without the polymer is

$$\frac{f}{f_0} = \frac{3}{2}\frac{E_{\mathrm{P}}h_{\mathrm{P}}}{E_{\mathrm{PI}}h_{\mathrm{PI}}} - \frac{1}{2}\frac{\rho_{\mathrm{P}}h_{\mathrm{P}}}{\rho_{\mathrm{PI}}h_{\mathrm{PI}}} \tag{13}$$

For the 3D vibrators presented in the main text, an Au layer is sandwiched between two PI layers. Therefore, the PI modulus E_{PI} and density ρ_{PI} should be revised to the effective modulus $\hat{E}_{\mathrm{Base}}$ and average density $\hat{\rho}_{\mathrm{Base}}$ of the PI/Au/PI tri-layer. Equation (S12) is for the structure with the polymer depositing on the entire surface of the base layer. When the polymer is patterned on a selected

region such as the one shown in Figure S5a, the parameters C_{E} and C_{ρ} replace $\frac{3}{2}$ and $\frac{1}{2}$, respectively. These considerations lead to the scaling law Eq. (1) in Section 4.4.2.

C. 2 Effective Modulus and Average Density of an *n*-Layer Composite

The effective modulus of an *n*-layer composite is

$$\hat{E} = \frac{12}{h^3}\left(\frac{D_3}{3} - D_2 y_{\mathrm{m}} + D_1 y_{\mathrm{m}}^2\right) \tag{14}$$

with

$$D_1 = \sum_{i=1}^{n} E_i h_i,\ D_2 = \sum_{i=1}^{n} E_i\left(y_i^2 - y_{i-1}^2\right),\ D_3 = \sum_{i=1}^{n} E_i\left(y_i^3 - y_{i-1}^3\right),\ y_{\mathrm{m}} = \frac{D_2}{2D_1},\ h = \sum_{i=1}^{n} h_i \tag{15}$$

where E_i and h_i is the modulus and thickness of the *i*-th layer respectively; $y_0 = 0$ and $y_i = y_{i-1} + h_i$ for *i*=1, 2,..., *n*. The average density is

$$\hat{\rho} = \frac{1}{h}\sum_{i=1}^{n} \rho_i h_i \tag{16}$$

where ρ_i is the density of the *i*-th layer.

C. 3 Polymer Patterns for Determining Polymer Modulus and Density of Isotropic Materials

An algorithm was developed to select the polymer patterns such that the resonant frequencies of the two vibration modes have decoupled sensitivities to the polymer modulus and density. FEA first predicts the distribution of the ratio $\frac{W_{\mathrm{Strain}}}{W_{\mathrm{Kinetic}}}$ without polymer for vibration mode 1 and mode 2, respectively; W_{Strain} and W_{Kinetic} are the strain energy density and the kinetic energy density of vibration, respectively. For vibration mode 1, the entire region (Ω, area *A*) of the base

layer is divided into $\Omega_{\text{Polymer(1)}}$ (area $A_{\text{Polymer(1)}}$) and $\Omega_{\text{NoPolymer(1)}}$, with $\Omega_{\text{Polymer(1)}} \bigcup \Omega_{\text{NoPolymer(1)}} = \Omega$, $\Omega_{\text{Polymer(1)}} \bigcap \Omega_{\text{NoPolymer(1)}} = \varnothing$ and $A_{\text{Polymer(1)}} = \beta_{(1)} A$. $\beta_{(1)}$ is an optimization variable. The region $\Omega_{\text{Polymer(1)}}$ is selected such that for an arbitrary point in $\Omega_{\text{Polymer(1)}}$, the ratio $\frac{W_{\text{Strain}}}{W_{\text{Kinetic}}}$ is larger than that of an arbitrary point in $\Omega_{\text{NoPolymer(1)}}$. Similarly for vibration mode 2, a region $\Omega_{\text{Polymer(2)}}$ with area $A_{\text{Polymer(2)}} = \beta_{(2)} A$ is selected such that for an arbitrary point in $\Omega_{\text{Polymer(2)}}$, the ratio $\frac{W_{\text{Strain}}}{W_{\text{Kinetic}}}$ is smaller than that of an arbitrary point in $\Omega_{\text{NoPolymer(2)}}$ ($\Omega_{\text{Polymer(2)}} \bigcup \Omega_{\text{NoPolymer(2)}} = \Omega$, $\Omega_{\text{Polymer(2)}} \bigcap \Omega_{\text{NoPolymer(2)}} = \varnothing$). $\beta_{(2)}$ is also an optimization variable. The polymer patterns are the intersection of $\Omega_{\text{Polymer(1)}}$ and $\Omega_{\text{Polymer(2)}}$. With the polymer patterns obtained in this manner, FEA predicts the relationship of the resonant frequency versus the polymer modulus and density for the two vibration modes. A parameter study on the variables $\beta_{(1)}$ and $\beta_{(2)}$ suggests that with $\beta_{(1)} = \beta_{(2)} = 0.68$, the sensitivities of the two vibration modes to the polymer modulus and density are reasonably well decoupled (Figure 4.8a&b).

C. 4 Determination of Polymer Modulus and Density from Multimodal Resonance

Equation (1) in Section 4.4.2 leads to the following formula to determine the polymer modulus and density

$$E_{\text{P}} = \frac{\hat{E}_{\text{Base}} h_{\text{Base}}}{h_{\text{P}}} \frac{C_{\rho(1)}\left(\hat{f}_{(2)} - 1\right) - C_{\rho(2)}\left(\hat{f}_{(1)} - 1\right)}{C_{\text{E}(2)} C_{\rho(1)} - C_{\text{E}(1)} C_{\rho(2)}} \tag{17}$$

$$\rho_{\text{P}} = \frac{\hat{\rho}_{\text{Base}} h_{\text{Base}}}{h_{\text{P}}} \frac{C_{\text{E}(1)}\left(\hat{f}_{(2)} - 1\right) - C_{\text{E}(2)}\left(\hat{f}_{(1)} - 1\right)}{C_{\text{E}(2)} C_{\rho(1)} - C_{\text{E}(1)} C_{\rho(2)}} \tag{18}$$

where $\hat{f}_{(1)}=\frac{f_{(1)}}{f_{0(1)}}$ and $\hat{f}_{(2)}=\frac{f_{(2)}}{f_{0(2)}}$ are the ratio of the resonant frequency with/without the polymer for vibration mode 1 and 2, respectively. The uncertainties in the determined polymer modulus and density caused by the uncertainties in the experiment results of the resonant frequencies are

$$\delta E_{\mathrm{P}}=\frac{\hat{E}_{\mathrm{Base}}h_{\mathrm{Base}}}{h_{\mathrm{P}}}\frac{C_{\rho(1)}\delta\hat{f}_{(2)}-C_{\rho(2)}\delta\hat{f}_{(1)}}{C_{\mathrm{E}(2)}C_{\rho(1)}-C_{\mathrm{E}(1)}C_{\rho(2)}}-\frac{\delta h_{\mathrm{P}}}{h_{\mathrm{P}}}E_{\mathrm{P}} \tag{19}$$

$$\delta\rho_{\mathrm{P}}=\frac{\hat{\rho}_{\mathrm{Base}}h_{\mathrm{Base}}}{h_{\mathrm{P}}}\frac{C_{\mathrm{E}(1)}\delta\hat{f}_{(2)}-C_{\mathrm{E}(2)}\delta\hat{f}_{(1)}}{C_{\mathrm{E}(2)}C_{\rho(1)}-C_{\mathrm{E}(1)}C_{\rho(2)}}-\frac{\delta h_{\mathrm{P}}}{h_{\mathrm{P}}}\rho_{\mathrm{P}} \tag{20}$$

respectively, where

$$\delta\hat{f}_{(1)}=\frac{\delta f_{(1)}}{f_{(1)}}-\frac{f_{(1)}}{f_{0(1)}}\frac{\delta f_{0(1)}}{f_{0(1)}},\quad \delta\hat{f}_{(2)}=\frac{\delta f_{(2)}}{f_{(2)}}-\frac{f_{(2)}}{f_{0(2)}}\frac{\delta f_{0(2)}}{f_{0(2)}} \tag{21}$$

$\delta f_{(1)}$, $\delta f_{0(1)}$, $\delta f_{(2)}$ and $\delta f_{0(2)}$ are the uncertainties in the resonant frequency with/without polymer of vibration mode 1 and 2, respectively; δh_{P} is the uncertainty in the polymer thickness.

C. 5 Polymer Patterns for Determining Longitudinal Modulus and Transverse Modulus of Transversely Isotropic Materials

A similar algorithm selects the polymer patterns presented in Figure 4.11b such that the resonant frequencies of the two vibration modes have decoupled sensitivities to the longitudinal modulus and the transverse modulus. FEA first predicts the distribution of the ratio $\left|\frac{\varepsilon_l}{\varepsilon_t}\right|$ without polymer for vibration mode 1 and mode 2, respectively; ε_l and ε_t are the normal strain of vibration along the longitudinal direction and the transverse direction, respectively. Region $\Omega_{\mathrm{Polymer(1)}}$ is selected such that for an arbitrary point in $\Omega_{\mathrm{Polymer(1)}}$, the ratio $\left|\frac{\varepsilon_l}{\varepsilon_t}\right|$ is larger than that

of an arbitrary point in region $\Omega_{\text{NoPolymer}(1)}$. Region $\Omega_{\text{Polymer}(2)}$ is selected such that for an arbitrary point in $\Omega_{\text{Polymer}(2)}$, the ratio $\left|\frac{\varepsilon_l}{\varepsilon_t}\right|$ is smaller than that of an arbitrary point in region $\Omega_{\text{NoPolymer}(2)}$. The polymer patterns are the intersection of $\Omega_{\text{Polymer}(1)}$ and $\Omega_{\text{Polymer}(2)}$. $\beta_{(1)}$ and $\beta_{(2)}$ are optimization variables. A parameter study on $\beta_{(1)}$ and $\beta_{(2)}$ suggests that with $\beta_{(1)} = \beta_{(2)} = 0.62$, the sensitivities of the two vibration modes to the longitudinal modulus and the transverse modulus are reasonably well decoupled (Figure 4.11c&d).